uOttawa

L'Université canadienne
Canada's university

FACULTÉ DES ÉTUDES SUPÉRIEURES ET POSTOCTORALES

uOttawa

L'Université canadienne
Canada's university

FACULTY OF GRADUATE AND POSDOCTORAL STUDIES

Jinsong Xie
AUTEUR DE LA THÈSE / AUTHOR OF THESIS

M.A.Sc. (Civil Engineering)
GRADE / DEGREE

Department of Civil Engineering
FACULTÉ, ÉCOLE, DÉPARTEMENT / FACULTY, SCHOOL, DEPARTMENT

Numerical Modeling of Tsunami Waves

TITRE DE LA THÈSE / TITLE OF THESIS

Dr. Ioan Nistor
DIRECTEUR (DIRECTRICE) DE LA THÈSE / THESIS SUPERVISOR

Dr. T. Murty
CO-DIRECTEUR (CO-DIRECTRICE) DE LA THÈSE / THESIS CO-SUPERVISOR

EXAMINATEURS (EXAMINATRICES) DE LA THÈSE / THESIS EXAMINERS

Dr. Paul Simms

Dr. C. Rennie

Dr. N. Nirupama

Gary W. Slater
Le Doyen de la Faculté des études supérieures et postdoctorales / Dean of the Faculty of Graduate and Postdoctoral Studies

NUMERICAL MODELING OF TSUNAMI WAVES

by

Jinsong Xie

A thesis
submitted under the supervision of
Dr. Ioan Nistor
and
Dr. Tad Murty

in partial fulfillment of the
requirements for the degree of
Master of Applied Science
in
Civil Engineering

Department of Civil Engineering
University of Ottawa
Ottawa, Canada
K1N 6N5

May, 2007

Library and
Archives Canada

Published Heritage
Branch

395 Wellington Street
Ottawa ON K1A 0N4
Canada

Bibliothèque et
Archives Canada

Direction du
Patrimoine de l'édition

395, rue Wellington
Ottawa ON K1A 0N4
Canada

Your file Votre référence
ISBN: 978-0-494-49296-3
Our file Notre référence
ISBN: 978-0-494-49296-3

NOTICE:
The author has granted a non-exclusive license allowing Library and Archives Canada to reproduce, publish, archive, preserve, conserve, communicate to the public by telecommunication or on the Internet, loan, distribute and sell theses worldwide, for commercial or non-commercial purposes, in microform, paper, electronic and/or any other formats.

The author retains copyright ownership and moral rights in this thesis. Neither the thesis nor substantial extracts from it may be printed or otherwise reproduced without the author's permission.

AVIS:
L'auteur a accordé une licence non exclusive permettant à la Bibliothèque et Archives Canada de reproduire, publier, archiver, sauvegarder, conserver, transmettre au public par télécommunication ou par l'Internet, prêter, distribuer et vendre des thèses partout dans le monde, à des fins commerciales ou autres, sur support microforme, papier, électronique et/ou autres formats.

L'auteur conserve la propriété du droit d'auteur et des droits moraux qui protège cette thèse. Ni la thèse ni des extraits substantiels de celle-ci ne doivent être imprimés ou autrement reproduits sans son autorisation.

In compliance with the Canadian Privacy Act some supporting forms may have been removed from this thesis.

While these forms may be included in the document page count, their removal does not represent any loss of content from the thesis.

Conformément à la loi canadienne sur la protection de la vie privée, quelques formulaires secondaires ont été enlevés de cette thèse.

Bien que ces formulaires aient inclus dans la pagination, il n'y aura aucun contenu manquant.

Canada

The University of Ottawa
Faculty of Engineering

This Certifies that

Jinsong Xie

Has been awarded a Research Poster Prize (1st Place)
In the Civil Engineering Category

For the poster entitled:
Tsunami Risk for Western Canada - Numerical Modelling of the
Cascadia Fault Tsunami

uOttawa

2007

Murat Saatcioglu
Vice Dean (Research)

ABSTRACT

This thesis provides a synthetic understanding and an extensive analysis on megathrust earthquake generated tsunamis, with emphasis on the application of numerical modeling. In the present thesis, the tsunami characteristics are first depicted as a special hydrodynamic phenomenon. Further, a detailed literature review on the recent developments in tsunami numerical modeling techniques and on their applications is presented. A common approach in modeling the generation, propagation and inundation of tsunamis is discussed and used in the thesis. Based on the assumption of a vertical displacement of ocean water that is analogous to the ocean bottom displacement during a submarine earthquake, and the use of a non-dispersive long-wave model to simulate its physical transformation as it radiates outward from the source region. A general analysis of the Indian Ocean Tsunami of December 26th, 2004 is provided; and tsunami generation and propagation is conducted for this tsunami, as well as for tsunamis occurring in the Arabian Sea and Northwest Pacific Ocean, near the coast of the Vancouver Island. The analyses are based on geological and seismological parameters collected by the author. In this paper the author uses the collected bathymetry and earthquake information, plus tide gauge records and field survey results, and focuses on the theoretical assumptions, validation and limitation of the existing numerical models. Numerical simulations are performed using MIRONE, a tsunami modelling software developed based on the nonlinear shallow water theory. Through numerical modeling of three tsunami scenarios, e.g. December 26, 2004 Indian Ocean Tsunami, November 28, 1945 Arabian Sea Tsunami and the potential Cascadia Tsunami, a vivid overview of the tsunami features is provided as discussed. Generally, the results fairly agree with the observed data. The GEOWARE software is used to compute the tsunami travel time necessary to calibrate the results from MIRONE, using different numerical techniques. Several sensitivity analyses are conducted so that one can understand how oceanic topography affects tsunami wave propagation, determine how smoothing the topography affects the simulated tsunami travel time, and interpret the tsunami wave-height patterns as seen in the model simulations. The model can predict reasonably the tsunami behaviour, and are thus useful for tsunami warning system (tsunami mitigation and preparedness); and coastal population and industry can prepare for such possible catastrophic events.

ACKNOWLEDGEMENTS

First of all, deepest gratitude and great appreciation is extended to his academic advisors, Dr. Ioan Nistor and Dr. Tad Murty, for their continuous and supportive guidance, suggestions and mentorship; acknowledge the simulating discussion and inspiration. The constant patience and invaluable help, backed by high level of generosity and intelligence, made their contributions to the present thesis unaccountable. They guided the author's steps into the world of scientific research.

In particular, the author is also grateful to Professor Charles L. Mader for his kindness, interesting informative comments. His wisdom provided the author with both invaluable scientific and spiritual knowledge. Sincere thanks are directed to Professor Joaquim Luis for his professional advising, generosity and almost peer mentorship. Acknowledgements are also addressed to Professor Paul Wessel and Niru Nirupama for their guidance to GEOWARE model.

The author would like to acknowledge the support of the Ontario Student Assistance Program (OSAP) and of the University of Ottawa. The deepest appreciation is conveyed to all the members of the colleagues and academic staff of Water Resource, Department of Civil Engineering. To all the other people of University of Ottawa, both staff and students, the author would like to deeply thank for the constant help in managing the problems involved by his presence among them.

The great memories and excellent two years together with Dr. Ioan Nistor and Dr. Tad Murty in University of Ottawa will always remain unforgettable.

Finally, this work would not have been possible without the continuous spiritual and economic support from his family who trustfully and patiently encouraged him to pursue his dreams with enthusiasm, optimism and confidence. This thesis is dedicated to them.

TABLE OF CONTENTS

LIST OF SYMBOLS

Symbol	Description
ρ	Water density
D	Water depth
C_s	Phase speed
C_g	Group speed
k	Wave number
C	Wave speed
ζ	The sea level
L	Wave length
H	Wave height
T	Wave period
g	Earth's gravity acceleration (g=9.81 m/s^2)
d	The total depth $d = D + \zeta - \eta$
d_0	The focal depth
φ	Strike
λ_0	Rake
δ	Slip angle
Δ	Maximum slip distance
W	Fault width
l_0	Fault length
μ	Shear modulus
M_0	Total seismic moment release
λ_0	A characteristic wave length of the tsunami
η_0	A typical amplitude of the tsunami
R	Radius of the Earth which is assumed to be equal to 6370km
Δs	Distance in the slope term (width of disturbed area)
N_z	Brunt-Vaisalla frequency (or buoyancy frequency of the ocean column)

υ	Kinematic viscosity of seawater
κ	A non-dimensional tuning parameter
P_e	Seabed pressure
a_x	Horizontal acceleration
$\frac{\Delta h}{\Delta s}$	Bathymetric slope of the disturbed seabed
α	A variable that include factors related to both the seismic disturbance and the ocean column
ω	Local current frequency given by $\omega = \frac{2\pi}{T_c}$
T_c	Period of current oscillation which is given by $\frac{1}{2}\sqrt{\frac{h}{g}}$
u	Velocity in the λ (E-W) direction
v	Velocity in the ϕ (N-S) direction
η	Bottom displacement
t	Time
f	Coriolis force
r	Bottom friction coefficient, equal to 3.3×10^{-3}
m	Time step
Mw	Earthquake magnitude
E_x	Energy flux in x direction
E_y	Energy flux in y direction
Ω	The Earth's angular velocity
$\tau_\lambda^b, \tau_\varphi^b$	Bottom friction force
$u(x,y,t)$	Magnitude of the induced horizontal current (m/s)

LIST OF FIGURES

LIST OF TABLES

CHAPTER 1

LITERATURE REVIEW

1. INTRODUCTION

1.1. Significance of the study

The Earth's crust actually consists of several major plates and many micro plates. Each of the plates moves at different rates and in different directions. All of the contacts and movements between two or more plates, as the results of those movements, produce the tectonic activities on the Earth. Those tectonic activities include earthquakes, volcano eruptions and landslides. All of these could trigger tsunamis. Unfortunately, earthquakes, which are the major cause of tsunami generation, are not yet predictable. Earthquake distribution maps show places where the earthquakes will likely happen, but no one has been able to predict exactly when or where an earthquake will occur. It is noticeable that probabilities of earthquake and tsunami recurrence in the near future can be evaluated to some degree based on recently developed paleo-seismology, paleo-tsunami studies, GPS geodesy, tectonic motion and fault slip. As long as the tectonic activities continue, earthquake and tsunamis will occur.

Along the history of humankind, tsunamis have been responsible for considerable damage to property and loss of life nearing the vicinity of coastal regions. As far back as 1480 B.C., history records destruction caused by huge tsunami waves which lead to loss of life and damage to local communities along the coastline. The violent explosion of the volcanic island of Krakatoa in August 1883 generated a thirty meter high tsunami wave that killed 36,500 people in Java and Sumatra; this is the first trans-ocean-wide tsunami recorded in historical time that was reasonably well-documented. The most destructive Pacific-wide tsunami in recent times was that of May 1960, which originated in Chile, killing over 1,000 people in Chile, Hawaii, the Philippines, Okinawa and Japan, and causing tremendous destruction to property. The tsunami of December 2004 in the Indian Ocean is by far the most destructive tsunami in historical time. This tsunami which killed more than 350,000 people caused loss of life more than all historical Pacific Ocean tsunamis combined for the 19th and 20th centuries. The 2004 Indian Ocean tsunami is the first global tsunami which occurred after modern instrumentation (wave gauges) became available and was installed.

During the last twenty years, the world witnessed the rapid growth and development of coastal areas in most of the developing, as well as the developed countries. It is the result of population explosion and of technological and economic developments that made the use of the coastal zone more necessary than before. As a consequence, aquaculture infrastructure has replaced much of the mangroves and beach forests along coastal shores. Many of the coastal sand dunes that acted as natural barriers against incoming waves were removed to make way for the construction of beach resorts, ports, walkways and roads. Significant changes have occurred to coastlines due to human activities and thus future tsunamis will have a much more severe social and economic impact.

In the current stage of human development, it can be concluded that tsunamis will have far more significant and long-term social and economic impacts. Although infrequent, tsunamis are among the most terrifying and complex physical phenomena and have been responsible for great loss of life and extensive destruction to property. Because of their destructive potential, tsunamis have important impact on the human, social and economic sectors of our societies. Historical records show that enormous destructions of coastal communities throughout the world have taken place and that the socio-economic impacts of tsunamis in the past have been enormous. Future tsunamis will have a much more severe social and economic impact. It is therefore important to study and simulate tsunamis in order to predict, mitigate and prepare for such future potential events.

Accordingly, it is essential to increase the preparedness of societies in order to deal with possible future disasters. The mitigation programs, ranging from improved building codes to public education to development of tsunami early warning systems, have the purpose to reduce losses due to catastrophic earthquakes and tsunamis. Furthermore, tsunami research can provide recommendations for the strengthening of disaster management strategies.

1.2. Scope of the study

Tsunami research is a multi-disciplinary field, involving at least eight major scientific disciplines: Geology, Seismology, Tsunami Science, Engineering, Disaster Management, Meteorology and Communications (*Tsunami Information Sources, Wiegel 2006*). This is not an all inclusive list. These disciplines can be subdivided into many topical subjects such as Paleo-tsunami, which belongs to Tsunami Science. Paleo-tsunami studies focus on tsunami events which occurred in the past, based on the sedimentation stratification found along the coastline. The objectives of Paleo-tsunami studies are to gain information on the possibility of a tsunami recurrence pattern and characteristics such as wave height, run-up and flooded area.

This thesis concentrates on numerical modeling of tsunami waves. A better understanding of tsunamis must take into account the tsunami generation mechanism; hence, the author briefly offers an introduction on tsunami wave phenomena, its generation mechanisms and its impacts on the coastline. The motivation for this study was to analyze the propagation of the December 2004 tsunami waves in the Indian Ocean, despite the fact that the recent Indian Ocean tsunami has been studied and simulated by various researchers, because the most complete information and data needed for research was available from this particular tsunami. There is a particular wealth of information and a unique data record, not only based on instrumental measurements, but also from the numerous scientific surveys conducted in several areas following the event. These extensive data records allowed numerical modelers to simulate all phases of this tsunami, and compare the results of their models with collected field data in order to calibrate these models. Therefore several studies were conducted for the region of the Indian Ocean, such as collecting tide gauge records data, field survey data, and associated impacts on bordering countries. Moreover, since an earthquake–induced tsunami is of interest for seismologists, a detailed study was made on the Indian Ocean plate tectonics, fault plane mechanisms, geology, geographical features and earthquake sources. In addition, consideration was also given to the possibility of a major tsunami along Vancouver Island in the region of the Cascadia subduction zone.

Tsunami is a long gravity wave and can be modeled in three stages: generation, propagation and coastal inundation or run-up. Prototype models and laboratory experiments are difficult due to scale considerations. Thus, numerical modeling becomes the best approach to simulate tsunamis in their three stages. Owing to lack of high-resolution bathymetry near the coastlines, emphasis was given to tsunami generation and propagation and less to the run-up phenomenon.

Two different numerical tsunami models were used, namely MIRONE and GEOWARE; sensitivity tests in terms of the two key output parameters, wave height and tsunami travel time, were also performed by varying the spatial grid size and the time steps. The Arabian Sea tsunami of November, 1945 was also simulated using the MIRONE model. Results were found to agree well with the recorded data.

1.3. Objectives of the study

Disaster preparedness requires several components, such as rapid identification of an imminent tsunami, effective national and regional warning systems to alert coastal population, and civil defense and community preparedness to respond to tsunami warnings. In spite of our technological improvement over the past two decades, we are still unable to provide timely warnings to many areas of the world. Improvements are necessary in communications in order to ensure that warnings are prompt and accurate. An increased degree of automation is necessary in handling and interpreting basic data. Research is also needed in the development of instrumentation such as deep-ocean sensors, which are useful in early tsunami detection. Instrumentation can help capture movements of the Earth's crust and measure the initial wave height of the tsunami. Research is also needed on the real-time interpretation of seismic source parameters, which in turn may help tsunami evaluation; apparently more research is needed to improve our understanding of tsunamis interacting with the coast. Research can also lead to improvements of early warning systems, for better land-use management of tsunami-prone coastal areas and to the development of important engineering guidelines of critical coastal structures.

The present numerical models include four different subroutines: tsunami generation model, tsunami propagation model, tsunami inundation model and tsunami travel time model. One result of the numerical computation is the tsunami travel times to various locations around the area of interest, while other output of the numerical model is represented by estimates of the maximum tsunami amplitude near the coast. A good tsunami generation model can provide appropriate initial conditions for the subsequent propagation model and the inundation model.

1.4. Organization of the dissertation

The first chapter provides background information about tsunamis and an extensive literature review on the numerical modeling of tsunamis. Part one of the chapter describes the significance, scope, objectives and organization of the dissertation. Part two provides an overview of tsunami phenomena: definition, generation, propagation and inundation mechanisms and outlines its characteristics and its destructive effects, and specifies tsunami features in different oceans. Part three of Chapter one describes the current tsunami numerical modeling techniques and procedures.

The second chapter focuses on the numerical modeling of tsunamis and introduces the MIRONE and GEOWARE numerical models. It also provides specifications on the characteristics and accuracy of the bathymetry and coastal topography used in the context of this thesis. The next part of Chapter two deals with the 2004 Indian Ocean tsunami using two different fault plane mechanisms and details on the calibration of the numerical model using the tide gauge records and satellite altimetry data. The calibrated model was further used to simulate two other tsunamis: the past Makran subduction zone tsunami in the Arabian Sea and a potential Cascadia subduction zone tsunami along Vancouver Island. Recommendations for future work are also provided in this chapter.

The third chapter introduces aspects on tsunami mitigation and preparedness. It has become clear that disaster management strategies need to be strengthened through the implementation of mitigation and preparedness options in order to enhance communities' resilience to natural hazards, such as tsunamis.

2. GENERAL OVERVIEW

2.1. Tsunami definition

A tsunami is a wave train, or a series of ocean waves, generated in a body of water by an impulsive disturbance that vertically displaces the water column. Earthquakes, landslides, volcanic eruptions, explosions, and even the impact of cosmic bodies, such as meteorites, can generate tsunamis. Tsunamis can savagely attack coastlines, causing devastating damage and loss of life. In deep-ocean, their wave length may be of the order of hundred of kilometers or more, but with a wave height of only a few tens of centimeters or less. Therefore, it is hard to detect and recognize the tsunami by visual observations before it reaches shallow waters. Although tsunami waves are often not taller than normal wind waves in open ocean, they are far more dangerous when they propagate on to the shoreline.

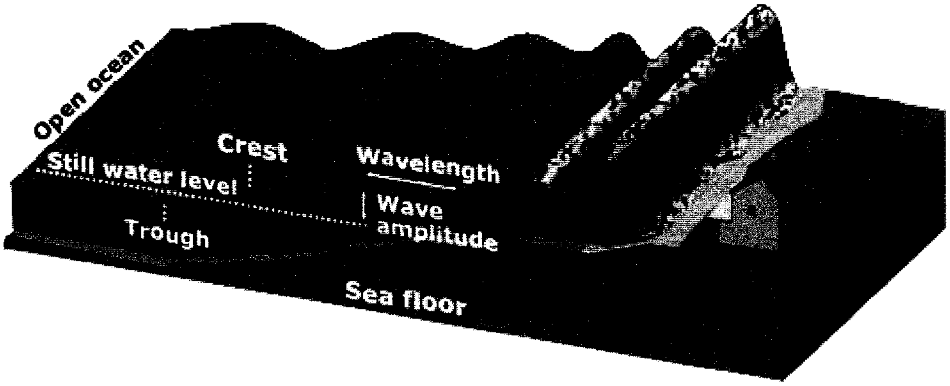

Figure 2-1: Change in tsunami wave shape as it approaches land (Ng *et al.,* 1990)

2.2. Tsunami generation

For the most part, tsunamis are generated by submarine earthquakes, less commonly by submarine landslides, and, occasionally, by volcanic eruptions and very rarely by meteorite impacts. Submarine landslides, which often accompany large earthquakes, as well as collapses of volcanic cones, can also disturb the overlying water column as sediment and rock slump down-slope and are redistributed across the seafloor. Similarly, a violent submarine volcanic eruption can create an impulsive force that uplifts the water column. When such volcanoes lie near bodies of water, resulting explosion debris can move the water body and rapidly displace some of that water, generating a tsunami. Conversely, submarine landslides and cosmic-body impacts disturb the water from above, as momentum from falling debris is transferred to the water. Tsunamis can be generated when the sea floor abruptly deforms and vertically displaces the overlying water. Tectonic earthquakes are a particular type of earthquake that are associated with the Earth's crust deformation. When these earthquakes occur beneath the sea floor, the water above the deformed area is displaced from its equilibrium position. Waves are hence formed as the displaced water mass, which is under the influence of gravity, attempts to regain its initial equilibrium surface. When large areas of the sea floor elevate or subside, a tsunami can be created.

2.3. Tsunami generation mechanism

Generally speaking, the amount of vertical motion of the sea floor, the area over which it occurs, the simultaneous occurrence of slumping of under water sediment due to the shaking, and the efficiency with which energy is transferred from the Earth's crust to the ocean water are all part of the tsunami generation mechanism. A tsunami can be generated by any disturbance that displaces a large water mass from its equilibrium position. In the case of earthquake-generated tsunamis, the water column is disturbed by the uplift or subsidence of the sea floor. Not all earthquakes generate tsunamis. The most important mechanism for tsunami generation is the vertical displacement of the seafloor. If the earthquake is in such a way that it only generates lateral movements (called strike-slip), there is no significant tsunami. To generate a tsunami, the fault where the earthquake occurs must be underneath or near the ocean. Shallow focus earthquakes along the subduction zone create a vertical movement (up to several meters) of the sea floor over a large area (up to hundred thousand square kilometers) which is called thrust-slip or dip-slip, and very large earthquakes of the order of magnitude 7.5 or greater. In other words, earthquake-induced tsunamis are characterized by a very shallow focus, with fault dislocations greater than several meters. They are also slow earthquakes, with slippage along the fault beneath the sea floor which occurs more slowly than it would happen in a normal earthquake. The only known method to quickly recognize a tsunami earthquake is to estimate a parameter called the seismic moment which uses very long period seismic waves (more than 50 seconds/cycle). Figure 2-2 shows the different possible tectonic rupture configurations during an earthquake.

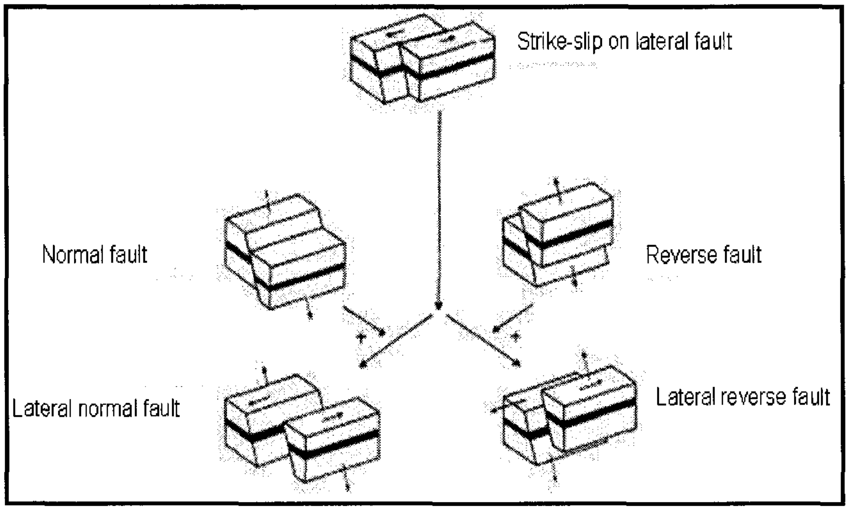

Figure 2-2: Earthquake rupture configurations (Murty *et al.*, 2005)

2.4. Tsunami propagation

Tsunami waves travel outward in all directions from the generating area with strong directionality of the main energy propagation and are modified as they pass over the varying ocean bathymetry. In the linear wave theory, the generalized equations of the phase velocity, C_s, and group velocity, C_g, for tsunami wave can be expressed as:

$$C_s = \sqrt{\frac{g}{k}\tanh(kd)} \qquad (1)$$

$$C_g = \frac{c_s}{2}[1+\frac{2kd}{\sinh 2kd}] \qquad (2)$$

Here d is water depth; k is the wave number. Within limited water depth and larger wave length, the ratio of kd usually is very small, thus the above formula can be simplified with $kD << 1$ to

$$C = \sqrt{gd} \qquad (3)$$

In this assumption, the wave speed is non-dispersive (does not depend on the wave length) and a single frequency applies. Therefore a tsunami travels at a speed that is only related to the water depth; hence, as the water depth decreases, the tsunami slows down; at a certain critical point when the water becomes very shallow, this assumption breaks down and no longer holds. While the tsunami's energy flux, which is dependent on both its wave speed and wave height, remains nearly constant, in the deep ocean, its speed is of the order of the speed of a jet plane and its height is reduced to only a few centimeters to perhaps one meter. When a tsunami approaches the shore, its speed decreases as its height increases. Just as other water waves, tsunamis begin to lose energy as they rush onshore; part of the wave energy is reflected offshore, while the shoreward-propagating wave energy is dissipated through bottom friction and turbulence. Despite these losses, tsunamis still reach the coast with significant amounts of energy.

2.5. Tsunami inundation and its destruction

Once the tsunami reaches land, it continues to push forward causing severe damage to any obstacles in its path. Tsunami waves usually do not break at the coast, but continue to move inland until the energy is finally dissipated through bottom friction or through impact with obstacles as well as due to the increasing slope of the land. The sheer height of the generated hydraulic bore is enough to pulverize objects in its path, often reducing buildings to their foundations and scouring exposed ground to the bedrock (Appendix A-1). Large objects such as ships and boulders can be carried several hundreds of meters or kilometers inland (Nistor, 2006) before the tsunami subsides. In certain cases, the sea can withdraw and empty harbors, this sometimes draws the curious people to the shoreline and to their death, since the recession of the sea is inevitably followed by the arrival of the crest of a tsunami wave.

Together, the strength of the disturbance, the distance the tsunami wave travels, and the shape of the coastline, determine the tsunami wave height, and ultimately, its destructive potential. Offshore and coastal features can determine the size and impact of tsunami waves. Reefs, bays, entrances to rivers, undersea features and the slope of the beach all help modify the tsunami shape and energy as it attacks the coastline. Tsunamis can reach a maximum vertical height onshore above sea level, often called a run-up height, of 10, 20, and even 50 meters. Two main factors affect the manner in which tsunami waves spread: they diverge away from the source, and are transformed by the topography of the sea floor. Close to the epicenter, the waves are controlled mostly by the shape of the earthquake fault.

Tsunamis have great erosional potential, stripping beaches of sand that may have taken thousands of years to accumulate and undermining trees and other coastal vegetation. The fast-moving water bodies associated with the inundating tsunami can crush homes and other coastal structures. Death and damage from tsunamis result mainly from inundation forces exerted by flooding and receding waves and the impact of floating debris. Tsunamis can cause heavy damage to houses, tourist resorts, fishing boats and gear, culture ponds and crops, and consequently affect the livelihood of large numbers of coastal communities. The destructive waves impact not only soil and water resources, but also damage healthy coral reefs, sea grass beds and beach forests. The surviving victims face psychosocial stress resulting from the loss of their loved ones, being rendered homeless and fears of another tsunami. The tsunami effects on human settlements, livelihood, coastal resources, and natural environment, together with the psychosocial well being of the members of the coastal communities all contributed to the degradation of the coastal ecosystems and communities.

2.6. Tsunami characteristics

Tsunamis act very differently from typical surf swells: they contain immense energy, propagate at high speeds and can travel great trans-oceanic distances with little overall energy loss. A tsunami can cause damage thousands of kilometers away from its origin, so there may be several hours between its creation and its impact on a coast. As the wave approaches land, the wave-front becomes steeper and taller, and there is less distance between crests. The wave can increase to a height of six stories or more as it approaches the coastline and gets compressed. The steepening process is analogous to the cracking of a tapered whip. As a wave goes down the whip from handle to tip, the same energy is carried by less and less material, and, as a consequence, the wave then moves more violently.

Some special hydrodynamic features can increase and/or prolong the tsunami wave height under the right conditions. The energy of an incident tsunami can be redistributed in time and space with the characteristics which differ from the original (incident) wave. These changes are induced by the nonlinear shallow water dynamics and by the trapped and partially leaky oscillations controlled by the continental slope/shelf topography. An amphidromic point is a position within a tidal system where the tidal range is almost zero. They are the 3-D equivalent of nodes in a standing wave problem. At the amphidromic point, there is almost no vertical movement, but further away the tidal range may be amplified. These amphidromic points can generate strong gradients of currents and hence amplify the tsunami wave. Helmholtz resonance is another phenomenon which can occur in harbours and bays, when a long gravity wave enters and is effectively trapped inside. This forces the wave to reflect back and forth inside the harbour over long time periods. Amplification of tsunami waves can occur through the drawing of energy from currents through Reynold's eddy stresses. Reflected waves from boundaries can also interact with direct tsunami waves, as well as the interaction with internal waves. Local geographic peculiarities can lead to seiche or standing waves forming, which can amplify the onshore damage. For instance, the tsunami that hit Hawaii on April 1, 1946 had a fifteen-minute interval between wave fronts. The natural resonant period of Hilo Bay is about thirty minutes. That means that, at each time step, the tsunami wave was in phase with the surface motion of Hilo Bay, creating a seiche in the bay. As a result, Hilo suffered the worst damage compared to any other place in Hawaii, with the tsunami/seiche reaching a height of 14 m and killing 159 inhabitants.

Tsunamis propagate outward from their source, so the coasts in the "shadow" of the impacted land masses are usually fairly safe. However, tsunami waves can diffract around land masses (as shown in this Indian Ocean tsunami where the waves reached the western shorelines of Sri Lanka and India). They are not necessarily symmetrical; tsunami waves may be much stronger in one direction than in others, depending on the nature of the source and the surrounding geography. Also, distance alone is no guarantee of safety. For instance, the 2004 Indian Ocean tsunami hit Somalia harder than Bangladesh despite being much farther away. Also tsunami behavior differs from region to region. As shown in Fig.2-3, the second wave of the 2004 Indian Ocean tsunami, which was the highest, approached Sri Lanka from both sides of the island due to diffraction and refraction, and the wrap-around effect produced very high waves on the shadowed area of Sri Lanka.

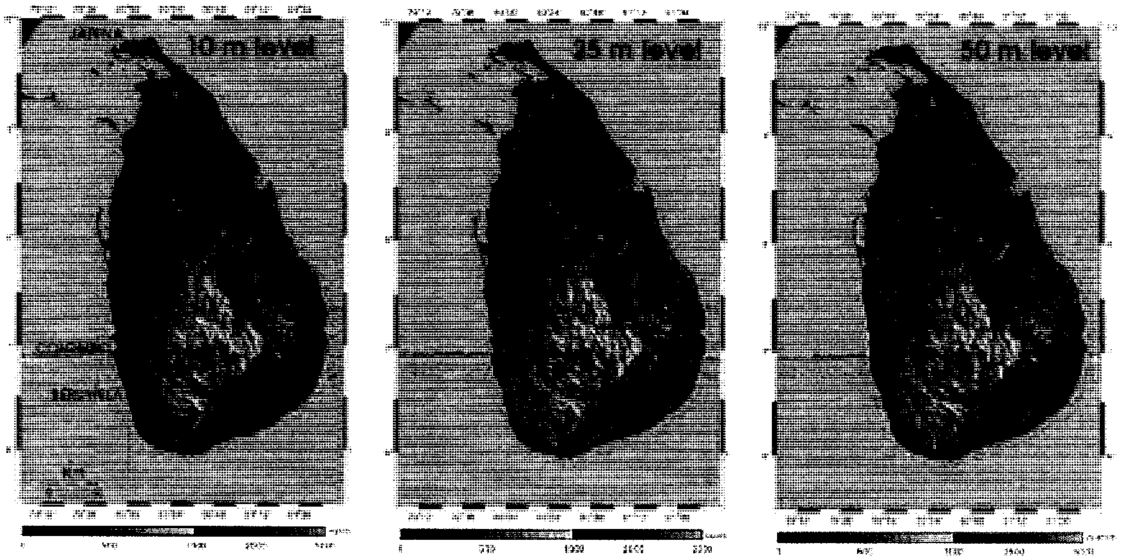

Figure 2-3: Inundation areas for rising sea level of 10, 25, and 50 meters respectively, (Fernando *et al.*, 2006)

2.7. Tsunami characteristics for the four planetary oceans

The Pacific Ocean and the Indian Ocean both lay on converging tectonic plate boundaries, which can create tsunamigenic earthquakes, in the form of trans-oceanic as well as local tsunamis. Due to the vastness of the Pacific, a tsunami on one side could take up to almost twenty-four hours to travel to the other far side. By contrast to the Pacific and Indian Oceans, the Atlantic Ocean contains a major diverging plate and therefore is not able to create large tsunamigenic earthquakes At the plate boundaries in the middle of the ocean. This makes tsunami events in the Atlantic Ocean extremely rare. Most often, tsunamis on one side of the Atlantic Ocean do not propagate to the opposite side since they dissipate quickly in time and space. The major difference between Pacific and Indian Oceans is that in the Indian Ocean, events are very rare and boundary conditions are not easy to numerically model. Ideally, one would need to obtain more frequency dispersion and less amplitude dispersion (nonlinear effects) so that the tsunami impact on the coast will be less. This is somewhat true for the Pacific and Atlantic Oceans and not true for Indian Ocean, at least not to the same degree. Because of large frequency dispersion in the Pacific, tsunamis are usually in the form of up to seven to ten waves and the highest wave varies between the third and fifth. In the Indian Ocean, because of the small phase dispersion, usually there are no more than three waves and the second wave is usually the highest. For this reason, even at the best of times (a perfect tsunami warning system), there is less warning time for the Indian Ocean tsunamis (Murty *et al.*, 2005). The Arctic Ocean is somewhat different from the other three oceans. Tsunamis are infrequent and usually localized. The ice cover over much of the ocean has an enormous influence over tsunamis. Notably, sparse population lives along the shores of the Arctic Ocean and there appears to be no urgent requirement for a tsunami warning system for the region.

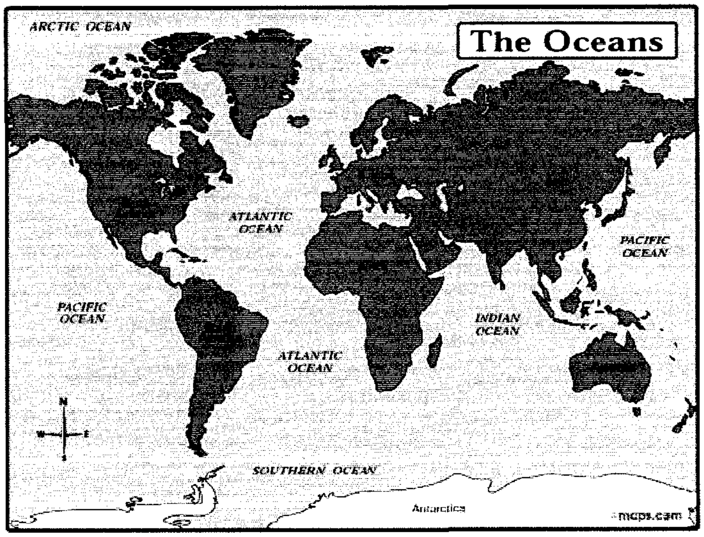

Figure 2-4: The Oceans of the World (EarthGuide, 2002).

Within the recorded history, approximately 225 tsunamis occurred around the world, mostly along the coastal areas of Japan, south-east Asia, the Caribbean Sea, Mexico, South America and Alaska (Volume Library, 1998). The coastlines around the Pacific Ocean are the most active seismic and volcanic regions on the surface of the Earth. Due to this fact, the entire circumference of the Pacific Rim is known as the "Ring of Fire". There are major faults that surround the Pacific region, as shown in Fig. 2-5.

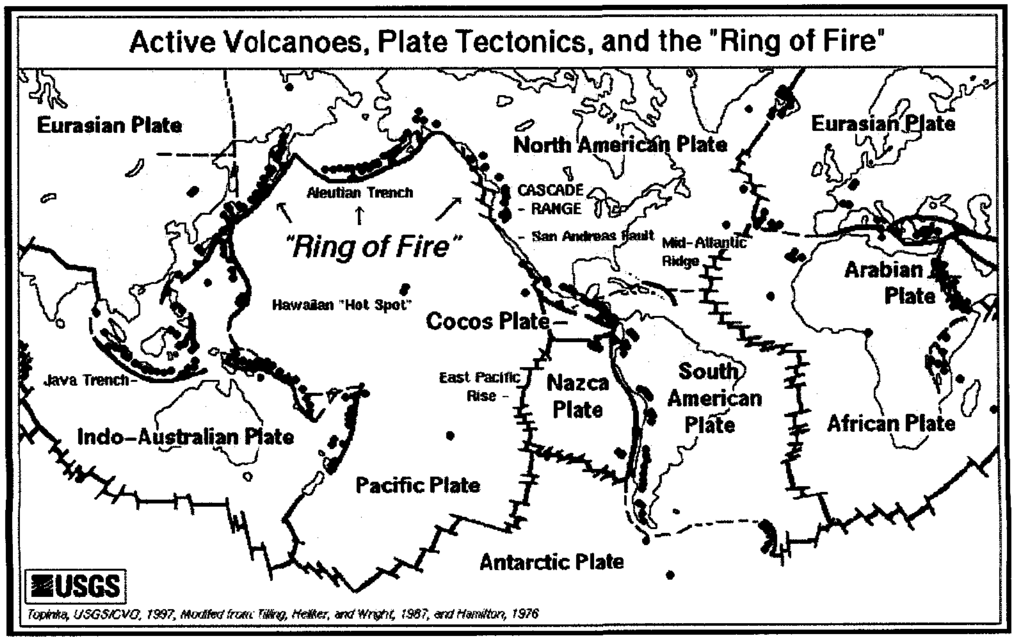

Figure 2-5: Location of the major planetary faults (USGS, 2006)

After the massive Aleutian earthquake tsunami of 1 April 1946, the Pacific tsunami warning system was established in 1949 in Hawaii. Up until now, there have been no tsunami warning systems for the Atlantic and Indian Oceans, because tsunamis occur very infrequently in these oceans. However, following the major tsunami which occurred in the Indian Ocean on December 26, 2004, tsunami warning systems are now being developed for both the Indian and Atlantic Oceans. At present, there is no priority for establishing a tsunami warning system for the Arctic Ocean, mainly because of very low population density around its rim.

Furthermore, we cannot have a global tsunami warning system mainly because the four major oceans are separated and different countries border different oceans. Also, some of the physical characteristics of the three oceans are such that three separate tsunami warning systems are needed: one for the Pacific, one for the Atlantic and one for the Indian Ocean as explained in Table 2-1.

Table 2-1: Tsunami characteristics of the four planetary oceans (Murty *et al.*, 2006)

Parameter	**Pacific Ocean**	**Atlantic Ocean**	**Indian Ocean**	**Arctic Ocean**
Area (km^2)	166,241,000	86,557,000	73,427,000	9,485,000
Average depth (m)	4,188	3,735	3,872	1,038
Deepest point (m)	Mariana Trench 11,033	Puerto Rico Trench 8,648	Java Trench 7,725	Eurasian Basin 5,450
Number of trenches	18	3	1	None
Unpopulated area (%)	About 20	About 30	About 55	Almost all of it
Length scale available (km).	6,447	4,284	4,284 – if we omit the unpopulated area, it is about 2,000	1,540
Ocean-wide tsunamis	Yes	No	Yes	Rare-extremely strong dissipative influence by ice cover
Tectonic-converging plates producing tsunamigenic earthquakes	Yes	No, at mid-Atlantic Ridge, the plates are diverging	Yes	Some, but not as strong as in Pacific and Indian Oceans
Frequency of tsunami occurrence	High	Rare	Rare	Rare
Frequency dispersion	High	N/A – since no ocean-wide tsunamis	Low	Small
Amplitude dispersion (nonlinear effects at the coast)	High	High	High	Moderate: Ice cover does not permit significant amplification of tsunami waves at the coast
Tsunami travel times	Up to 23 hrs	Only local tsunamis travel within minutes	Up to 10 hrs to most populated area	Local tsunamis. Several minutes to at most a couple of hours
Available warning time to most populated areas	Generally sufficient	Because of local tsunamis, only several minutes	1 to 4 hours	Small-mostly several minutes
Importance of initial conditions	High	High	High	High
Importance of boundary reflections	Low	Low, since tsunami originate close to the coast	High	Moderate, ice cover does not allow significant refection of waves
Relevance of boundary conditions	Low	Medium	High	Medium
Effect of Coriolis force	Noticeable	Highly noticeable	Noticeable	High, since Coriolis force is strong
Type of boundary conditions to be used	Radiation type	Not important since tsunamis are local	Reflective boundaries	Combination of radiative and reflective boundaries
Initial withdrawal of the ocean	Sometimes, at some locations	Rare	Sometimes, at some locations	Not obvious due to ice cover
Which wave is the highest?	Among 3rd to 5th	Usually 1st wave	Usually 2nd wave	Usually 1st or 2nd wave
Nature of physical process	Hyperbolic	Parabolic	Elliptic	Half way between parabolic and elliptic

3. LITERATURE REVIEW

3.1. Introduction

Since the occurrence of the 2004 Indian Ocean tsunami, tsunami research received significant attention all around the world. Many scientists and tsunami experts initiated an extensive tsunami research program, based on evidence on the earthquake and tsunami collected from the tide gauge stations, field surveys and sediment deposits, as well as data from satellite altimetry. Archaeologists, geomorphologists and geologists got involved in studying old tsunami deposits in order to provide more data on past events. But many details of the tsunami dynamics are still poorly understood, and realistic source models are not yet available.

One of the important problems in tsunami wave simulation is to establish the limits of validity of the various solutions due to simplifying assumptions. For tsunami waves generated from impact landslides, explosions, volcanic eruptions, projectile impacts and asteroids, the water flow is highly deformed and interacts with air so that we have to use compressible flow theory to best describe the flow characteristics. Due to the complexity of those aspects, Charles Mader (2004) introduced some basic notions, procedures and codes in his book *Numerical Modeling of Water Waves.* He did put more emphasis on incompressible water waves, mainly because most tsunamis are generated from earthquakes. Fortunately most tsunami waves generated by earthquake can be simulated by those incompressible models. Laboratory tests and field observations also support this assumption. Nowadays the widely used numerical models are derived from nonlinear shallow water, long wave equations using appropriate initial and boundary conditions. Three-dimensional models (based on Navier-Stokes equations) require huge computer resources and have limited practical applications. Two-dimensional models (2-DV) based on shallow water equations, derived from the Navier-Stokes equations, are widely used.

The evolution of the earthquake-generated tsunami waves has three distinctive stages: generation, propagation, and coastal inundation. Numerical experiments have provided feasible and useful descriptions of the tsunami wave propagation and inundation. This chapter begins with presentation of a common approach used in tsunami modeling, based on the assumption of the vertical displacement of ocean water that is analogous to the ocean bottom displacement during a submarine earthquake, and the use of nonlinear shallow water, long-wave model to simulate its physical transformation as it radiates outward from the source region. Then a detailed analysis of moving from knowledge of the tsunami mechanism to the numerical modules is given.

3.2. Wave theory

A great variety of water waves exists. Water wave motions include storm waves generated by wind over the oceans, flood waves in rivers, seiche or long-period oscillations in harbor basins, tidal bores or moving hydraulic jumps in estuaries, tsunami waves generated by earthquakes, and waves generated by explosions near or under the water. The main difficulty in studying water wave motion is the fact that the free surface boundary is unknown. Water wave motions are so varied and complex that any attempt to classify them may be misleading. Any definition corresponds to an idealized situation that never occurs. For example, a purely two-dimensional motion does not exist. However, this is a convenient mathematical concept that is physically best approached in a tank with parallel walls. Boundary layer effects and transverse components still exist although they are small and may be neglected in many applications of the theory. Essentially, two kinds of water waves exist: oscillatory waves and translatory waves. In an oscillatory wave, the transport of fluid or mass transport does not occur. The wave motion is then analogous to the transverse oscillation of a rope. A translatory wave involves a transport of fluid in the direction in which the wave travels. For example, a moving hydraulic jump such as a tidal bore is a translatory wave. An oscillatory wave can be progressive or standing; in a translatory wave, water is transported in the direction of the wave travel. In an Eulerian system of coordinates, a surface wave problem generally involves three unknowns: the free surface elevation (or total water depth), the pressure (generally known at the free surface), and the particle velocity.

The equations of fluid dynamics are representations of the laws of conservation of mass, momentum, and energy applied to a fluid. The general equations are often called the Navier-Stokes equations. In addition, one needs an equation of state to describe the properties of the fluids. The equation of state expresses the fact that the pressure is everywhere a function of the density and the energy per unit of mass. In hydrodynamics, the water wave theories are generally classified into two families. They are the "small amplitude wave theories" and the "long wave theories." The small amplitude wave theories are the linearized theories of the first categories of power series, i.e., the power series in terms of H/L. The long wave theories use the numerical method of solution for the nonlinear long wave equations. These two families include a number of variations and some intermediate cases with some of the characteristics of both families. For example, the Cnoidal wave and the solitary wave are considered as particular cases (steady state) of the long wave theories, because they are nonlinear shallow water waves.

As discussed above, tsunami being a water wave, it generally can be represented by three kinds of wave forms: sinusoidal wave, solitary wave or Stokes wave. Sinusoidal wave is the same as the one used in the theory of Airy, where it is assumed that D/L (D is water depth; L is wave length) is small. The sinusoidal wave used in the shallow water equation is given below in Figure 3-1. As a consequence, the equations of the fluid dynamics are simplified considerably. The pressure is hydrostatic and the horizontal velocity distribution is uniform. Special cases of the sinusoidal wave theory are the deep water, long wave ($D/L > 0.5$) and shallow water ($D/L < 0.05$) cases.

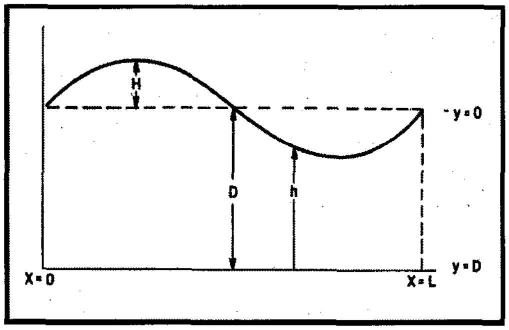

Figure 3-1: Schematic diagram of a sinusoidal wave

The Cnoidal solitary wave theory of Laitone is mathematically rigorous. At a first order of approximation, the vertical distribution of horizontal velocity is uniform. There is no mass transport. The terms in $(H/D)^2$ (H is wave height) are neglected. Laitone solitary wave theory is appropriate for (H/D) less than 0.3. The wave length used for the solitary wave is the length between approximately ±0.05 maximum wave heights, because the wave length is infinite. The wave profile is shown in Figure 3-2.

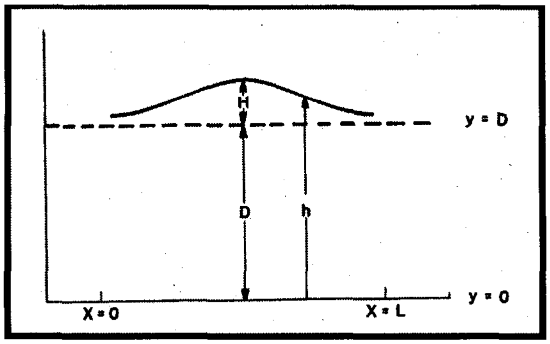

Figure 3-2: Schematic diagram of a solitary wave

The Stokes waves at a second order of approximation are characterized by the sum of two sinusoidal components of period T and $T/2$, respectively. As a result, the wave crest becomes peaked and the troughs become flatter, as shown in Figure 3-3. The wave profile can even be characterized by the appearance of a hump in the middle of the wave trough. Similarly, the elliptical particle path is deformed and tends to hump under the crest and flatten under the trough. For Stokes waves, the depth D divided by the wave length L should be greater than 0.125 and less than approximately 2.0.

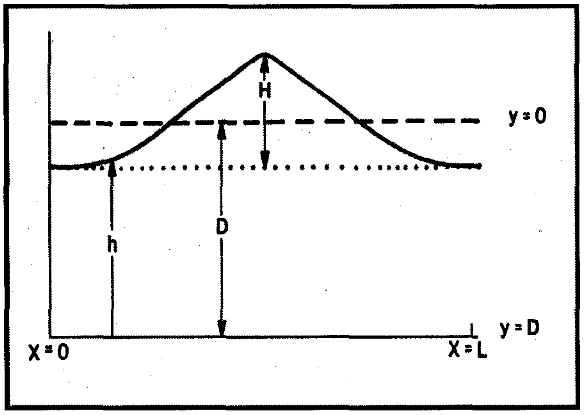

Figure 3-3: Schematic diagram of a Stokes wave

All these three kinds of waves were tested and compared by Mader *et al.* (2004) in his monograph. A choice among Airy wave, solitary wave and Stokes wave as input parameter in tsunami numerical modeling can be set by the user. In sinusoidal wave forms, the tsunami waves only appear as the main wave front; while in solitary wave or Stokes wave forms, the tsunami waves display a main wave front followed by a train of small wave, and generally the second or third wave is the maximum wave. These resemble more the profile of a real tsunami wave, so, if possible, one would better use Stokes wave forms as initial waves to simulate tsunami generation, propagation and inundation in the future. At present, because the Stokes wave is more complicated and hard to wire to the parameters required in the generation phase, and also due to the restriction of the generation model, the widely used tsunami initial wave form is the sinusoidal wave. Furthermore, realistic source models are not available and even if the earthquake source is known, the shallow water model can not model the tsunami wave generated by the source within a factor of 2 to 10 errors. An important aspect in the tsunami research field is dedicated to reproducing the realistic tsunami source model. The realistic tsunami can resemble neither a single sinusoidal wave, nor a Stokes wave; but by a mixture of them.

3.3. Methodologies for modeling tsunami generation

Since tsunami travel time is reversible, in the sense that the travel times are exactly the same, no matter in which direction the tsunami travels from a given physical domain, i.e.; from an epicentre in the ocean to a coastal site; vice-versa, from a coastal site to an epicentre in the ocean, the inverse Wave Tracing Techniques (Abe *et al.,* 1973; Satake *et al.,* 1993) are generally used to plot the generation region. The data used to plot are collected from tide gauge records, satellite altimetry, geodetic field measurements and Global Positioning System (GPS) and from seismic waves. The interpretation and study of such a complex data set is not easy. Tsunami sources can be constrained by the open-ocean satellite measurements and available seismic analysis, by the first arrival times on tide gauge records, by geodetic field measurements and Global Positioning System data. The details of the seismic deformation have substantial uncertainties. The ambiguities and difficulties of interpreting the distinctive seismic data for tsunami events are reflected by the substantially different source (generation) models derived from the different observed data sets. For instance, geodetic field measurements and Global Positioning System data can provide a source interpretation, while inversion studies of satellite tsunami data offer another version of the source. Source delineation is limited by the accuracy of the observed arrival times, by the bathymetry data used in the numerical simulations, and by non-linear and dispersive effects. Even with the same data set using different deducing method, the source patterns are different.

During the generation phase, the widely used generation mechanisms can be explained as follows: a sea floor disturbance due to an earthquake that reshapes the sea surface into an initial tsunami wave. An assumption was made that this sea surface displacement is the same as the ocean bottom displacement, due to incompressibility of the ocean water; an algorithm developed by Okada *et al.* (1985) is used to calculate the distribution of coseismic uplift and subsidence resulting from the motion of the buried fault. The fault parameters that are required to compute the deformation of the ocean bottom are: location of the epicentre, area of the fault, dip, rake, strike, and amount of slip on the fault (Figure 3-4 and Table 3-1). These parameters are based on definitions from Aki and Richards (1980). Strike is determined by the trench orientation; dip and slip are taken from the Harvard CMT solution (USGS); focal depth is based on the finite fault inversion of Ji *et al.* (2004).

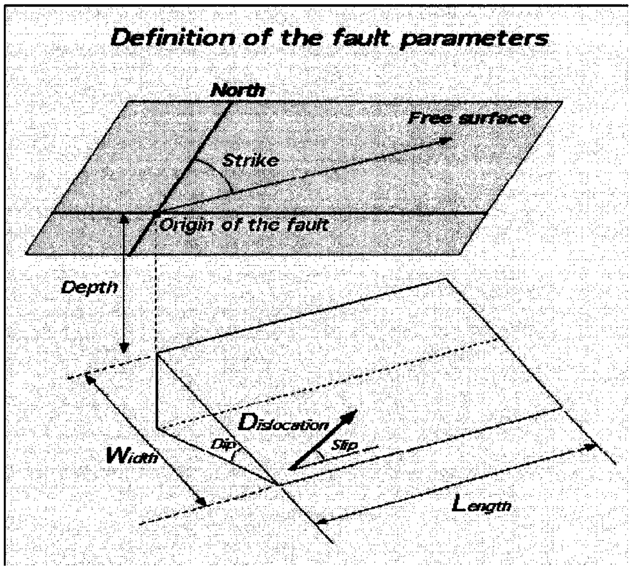

Figure 3-4: Schematic diagram of fault parameters

Table 3-1: Parameters based on the definitions of Aki and Richard (1980)

Earthquake Parameter	**How to decide the parameters**
Strike	Determined by the trench orientation
Dip	Taken from the Harvard CMT solution
Slip	Taken from the Harvard CMT solution
Length	Can be estimated by several approaches
Depth	Based on the finite fault inversion (Ji *et al.*, 2004)
Position	Can be estimated by several approaches
Moment	Based on normal mode analysis (Stein *et al.* and Okal *et al.*, 2005)

The earthquake's total rupture extent can be estimated using several methods. One of them is the finite fault seismic data inversion (Ji *et al.*, 2004; Yagi *et al.*, 2005) which yields fault lengths; another traditional method to delineate earthquake fault zones is plotting the aftershocks which occured in the first 24 hours following the main shock (Inverse Ray-tracing Method) [NEIC, 2004]. The aftershocks are expected to cluster within the slip zone. In this case, the fault extent is constrained by the observed tsunami travel times. Figure 3-5 displays the tsunami arrival time constraints on the fault zone.

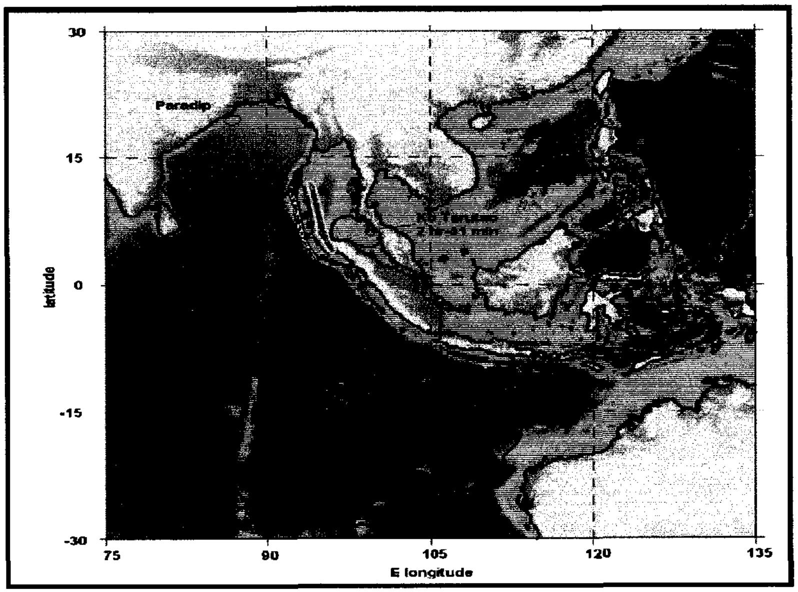

Figure 3-5: the 2004 Sumatra earthquake uplift as constrained by tsunami travel times (Kowalik *et al.*, 2005a)

As one may notice, the trench curvature of earthquake does not have a regular shape. To better accommodate the curve, usually the fault plane is broken into several segments. How to depict accurately the fault plane is mainly based on observed tsunami first motions on tide gauges. One of the source deformations for the 2004 Indian Ocean tsunami is shown in Figure 3-6. The free-surface profiles exhibit an elevated waveform on the western side and a depression waveform on the eastern side of the fault plane.

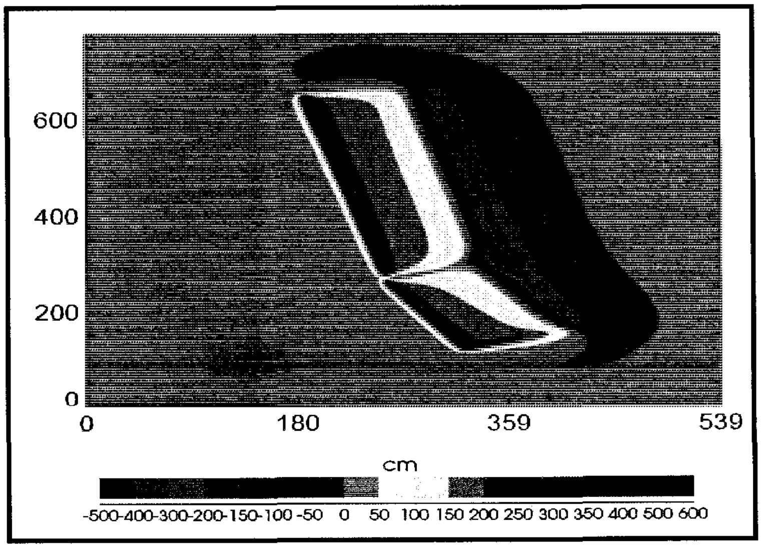

Figure 3-6: Source deformations of 2004 Indian Ocean Tsunami (Kowalik *et al.*, 2005a)

3.4. Defining the tsunami source region for the 2004 Indian Ocean tsunami

Fine *et al.* (2005) used wave arrival times at coastal tide gauges and satellite altimetry records to define the source region for the Indian Ocean tsunami of 26th December 2004. They calculated a curved 1000 km long and 250 km wide tsunami source region, centered over the Sunda subduction zone. According to these authors, this agreed well with the source derived from broadband geophysical data. The authors stated that, embedded in this general region, there are hot spots, associated with the southern fast-slip and northern slow-slip domains, which served as distinct source areas for the tsunami.

Large faults must form over time, presumably through small slip events followed in time by larger slip events (Wells and Coppersmith, 1994). Consequently, large single-event displacements tend to occur on structures that have already accumulated large total displacements. Therefore, the structures responsible for the December 26, 2004, event should be evident in the offshore bathymetry, unless they are buried under loose sediment. In the Bay of Bengal, sediments from rivers contribute to a massive sediment fan that covers the entire downgoing plate from north to south, but almost all sediments are diverted west of the overriding plate. The subduction zone is therefore expressed along the entire rupture length, with deformation and erosion of the overriding plate in plain view (see Figure 3-7). Watts *et al.* (2005) calculated four separate sources along a 1200 km long rupture zone for the Indian Ocean tsunami of December 2004. The total earthquake duration from these four sources was indicated to be of 331 seconds. The four segments shown in Figure 3-7 are described by Watts *et al.* (2005) as follows:

Segment 1 covers the Southern arc of the ruptured subduction zone, facing in a general South-West direction perpendicular to rupture. The faulting trends north along two relatively sharp bends, one to the north and one to the south of the segment. Here, the overriding plate is at its steepest, and the water depth is largest along the ruptured subduction zone, at around 5100 m in the deepest part of the Java trench. Segment 2 presents a long and relatively straight section of the subduction zone that trends almost North-South along the rupture. The most notable feature of this segment is the nearly uniform profile of the overriding plate, with a steep rise from the subduction trench to a shallow ridge, followed by a descent into a deeper basin further east. Segment 3 features a change in orientation and shape, notably a widening of the distance between the subduction zone and the basin to the east. The basin is narrower here, more in the form of a trench. The ridge is shallow enough to form a number of small islands. Segment 4 undergoes a change in orientation, as well as a change in structure, which is more complex and broken than before. A significant number of larger islands are formed on the overriding plate.

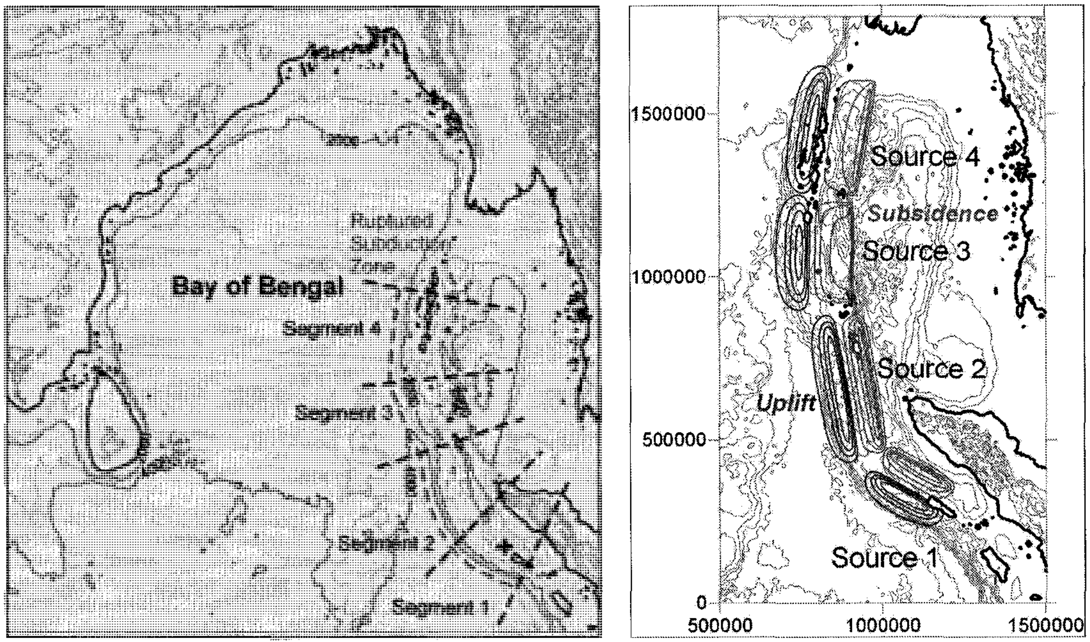

Figure 3-7: (a) Simulation grid for the Bay of Bengal. (b) Earthquake tsunami sources along rupture. Axes are in UTM coordinates centered on 0^0 Lat., 85^0 Long. E. (Watts et al., 2005)

Given the different shapes and orientations of the subduction zones described above, Watts et al., 2005 considered each segment as a distinct tsunami source (Figure 3-7b). Therefore, it was considered that each tsunami source had unique and different earthquake parameters that captured the morphology of its own segment. This means that a single rupture event will be represented by the sum of the four smaller rupture segments with distinct sea floor morphology (Table 3-2). Here d_0 is the focal depth, φ is the strike, λ_0 is the rake, δ is the slip angle, Δ is the maximum slip distance, l_0 is the fault length, W is the fault width, μ is the shear modulus, M_0 is the total seismic moment release, L is a characteristic wave length of the tsunami and H is a typical amplitude of the tsunami, (see Table 3-2).

Table 3-2: Source parameters for the four segments (Watts *et al.*, 2005)

Parameters	Segment 1	Segment 2	Segment 3	Segment 4
x_o (longitude)	1091550	917000	830000	867300
y_o (latitude)	370600	665000	1075100	1439300
D (km)	25	25	25	25
ϕ (degrees)	300	350	0	10
λ_0 (degrees)	90	90	90	90
δ (degrees)	11	13	15	11
Δ (m)	30	30	30	25
l_0 (km)	220	410	300	350
W (km)	90	90	150	150
μ (Pa)	$4.0\ 10^{10}$	$4.0\ 10^{10}$	$4.0\ 10^{10}$	$4.0\ 10^{10}$
M_o (J)	$1.8\ 10^{22}$	$3.4\ 10^{22}$	$4.0\ 10^{22}$	$4.0\ 10^{22}$
L (km)	90	90	150	150
H (m)	-9.2	-9.5	-7.6	-7.4

3.5. Tsunami propagation and inundation

The derived surface deformation was used as the initial condition for tsunami propagation. Past evidence suggests that tsunami waves consist of a train of several large, approximately sinusoidal waves of about 1 meter in height moving in the deep ocean at approximately the speed of $\sqrt{gD}$ or 210 meters per second on the average Pacific Ocean depth of 4500 meters, having periods of 10-30 minutes and wave lengths of 200-600 kilometers. It is the first four or five large waves that are of primary interest. In the phase of propagation, all the numerical models of tsunami waves currently used by NOAA, Cornell, and the universities of California, Washington, Alaska, and Hawaii, or WCATWC assume that the flow is described by the shallow water equations or a minor variation of them. The shallow water equations can be derived in a number of ways and in a variety of forms, all of which rely on the basic assumption that the flow is vertically hydrostatic, or, equivalently, that the vertical acceleration of water particles is negligible. Maximum tsunami height, commonly several hours after the first arrival, can result from reflection at a coast or resonance within a bay, in response to local coastal shape and bathymetry.

The capabilities of various tsunami models are listed in Table 3-3. From the table, LGW and COMCOT models use plane coordinate system. To convert from 3-D globe to 2-D map, a projection has to be used. For a large regional area, the projection mathematically distorts and shrinks a portion of the spheroid onto flat paper. Accordingly a good representation of accurate bathymetry must be spherical coordinate system. Predicting wave run-up on an open coast is important in estimating the area affected by storm waves and tsunamis.

Table 3-3: Characteristics of the current tsunami numerical models

Model Parameters	LGW	COMCOT	SWAN	MIRONE	ZUNI	MOST	TSUN2	UAF
Generation	Y	Y	Y	Y	Y	Y	Y	Y
Propagation	Y	Y	Y	Y	Y	Y	Y	Y
Inundation	Y	Y	Y	Y	Y	Y	Y	Y
Wave theory	Airy	Airy	Airy	Airy	Stokes	Airy	Airy	Airy
Nonlinear	Linear	Linear	Nonlinear	Nonlinear	Non-linear	Nonlinear	Nonlinear	Nonlinear
Finite Difference	Y	Y	Y	Y	Y	Y	Y	Y
Coordinate System	Plane	Plane	Spherical	Spherical	Plane	Spherical	Spherical	Spherical
Coriolis	N	N	Y	Y	N	Y	Y	Y
Friction	Y	Y	Y	Y	N	Y	Y	Y
Surface Stress	N	N	N	N	N	N	N	N
Boundary Condition	bad	good	bad	bad	bad	better	good	better
Nested Grid	N	Y	Y	N	Y	Y	Y	Y
Dispersion	N	N	N	N	Y	Y	Y	Y

Notes: 'Y' means used; 'N' means not used. 'better' means is better compared with all other models

3.6. Other numerical models for tsunami generation and propagation

Annunziato and Best (2006) mentioned certain numerical models which were employed in the modeling of the December 2004 tsunami event. Specifically, they referred to (1) WL Model (Delft Hydraulics, Netherlands), (2) MOST Model (NOAA, US) and (3) INGV Model (Italy).

According to Annunziato and Best (2006), all these models were initialized in a rather subjective manner, since characteristics of the generating earthquake are not fully known. For the Delft Hydraulics model, the calculation starts with an initial disturbance of about 650 km along the fractal ocean, in front of Banda Aceh. The results are mainly animations and the calculated times slightly underestimate the observed arrival time of the first waves. For the MOST Model (Method of Splitting Tsunami model), according to Annunziato and Best (2006), one of the problems raised was the presence of an initial wave with a 3 cm amplitude which cannot be properly explained. Also, the MOST model must have a single high friction factor in order to remain numerically stable. The INGV Model is a shallow water wave model which uses a finite difference numerical scheme. The authors also mentioned the JRC (Joint Research Center of the European Commission) Model, which uses the ETOPO-5 ocean bathymetry (depth data at 5 minutes of arc in both latitude and longitude) and employs the simple non-dispersive long gravity wave assumption. For computing travel times of the tsunami, however, diffraction has been included in a somewhat simplified manner. Murty *et al.* (2006, a, b, c) showed that the numerical modeling of the Indian Ocean tsunami was somewhat different from that of the Pacific Ocean. Tsunami waves in the Pacific Ocean - the largest of all oceans - may reach maximum tsunami travel times of the order of one day. Hence, trans-oceanic reflection of tsunamis is not very important and the tsunami propagation can be treated as a hyperbolic problem. If only a part of the Pacific Ocean is modeled, one may be able to use the simple radiative-type boundary condition. On the other hand, the Indian Ocean is significantly smaller than the Pacific Ocean and maximum tsunami travel times are of the order of 10 hours. Hence trans-oceanic reflection of tsunamis must be taken into account, making thus the problem somewhat elliptic, one has to use reflective boundary conditions.

Geist *et al.* (2007) compared observed tsunami heights with wave amplitudes computed from different tsunami forecasting and hazard assessment models. The following information is reproduced from their paper.

Several studies indicated that far-field tsunami amplitudes can be estimated from the scalar seismic moment of the earthquake (Comer 1980, Ward 1980, Okal 1988, Pelayo and Wiens 1992). Empirical and theoretical relationships that link far-field tsunami amplitudes with seismic moment include attenuating effects of the geometric spreading as a function of the propagation distance (R) (Wu 1981, Mei 1989). Abe (1979, 1995) provided an empirical relationship relating tsunami height (in meters) (Ht) to the earthquake moment magnitude (Mw) as follows,

$$\log Ht = Mw - \log R - 5.55 + C, \tag{4}$$

where $C = 0.0$ for interplate thrust earthquakes and $C = 0.2$ for back-arc events and where R is the distance (measured in kilometres) from the epicentre. Because this regression equation overpredicts the tsunami wave heights in the near field, a local limiting tsunami height (Hr) that is independent of distance was proposed by Abe (1981, 1995) as,

$$\log Hr = 0.5Mw - 3.30 + C, \tag{5}$$

Abe (1995) indicated that, statistically, Hr represents the mean local run-up and that $2 \times Hr$ approximates the maximum local run-up. Abe (1995) provided a detailed statistical comparison for local tsunamis, while Furumoto (1996) provided a test for this relationship at far-field distances. To determine how these empirical relations fared for the 2004 Sumatra–Andaman earthquake, the authors used an earthquake moment magnitude, Mw, with a value of 9.0, which was determined soon after the event, using 300 to 500-seconds period surface waves (Lay *et al.*, 2005). At regional distances, the far-field relationship (Eq. 4) for example, slightly underpredicts the mean observed run-up heights in southeast India (Yeh *et al.*, 2005); Ht = 2.8 m; while values of 2.5–5.2 m were reported. This is consistent with the reported mean run-up heights in Dawei, Myanmar (Satake *et al.*, 2006b); Ht = 2.3 m; while values of 0.9–2.9 m were reported. In contrast, along an azimuth in line with the tsunami beaming pattern, the empirical Eq. (5) greatly underpredicts the mean observed tsunami run-up in Sri Lanka (Liu *et al.*, 2005; Goff *et al.*, 2006) (Ht = 1.7 m; while values of 2.5–7.0 m were reported). Locally, the mean (Hr = 16 m) and maximum limiting run-up height ($2 \times Hr$=32 m) were very close to the run-up heights observed along the western Aceh Province of Sumatra: 30 to 35 m (Borrero *et al.*, 2005; Tsuji *et al.* 2005; Jaffe *et al.* 2006).

Hebert *et al.* (2007) modeled the 2004 Indian Ocean tsunami, with particular reference to the Mascarene Islands. They used two different source models. These fault parameters are shown in Table 3-4.

Table 3-4: Faults parameters used for the model (Hebert *et al.*, 2007)

Sub-fault	Coordinates (lat. N, long. E)	Strike, Dip, Rake (°)	Length (km)	Slip (m) (Model A)	Slip (m) (Model B)
1	(13.0, 92.9)	10, 15, 100	150	3	8.5
2	(10.3, 92.8)	359, 14, 98	450	5	8.5
3	(7.3, 93.1)	345, 13, 95	240	12	8.5
4	(5.4, 93.75)	337, 12, 92	200	16	8.5
5	(3.8, 94.5)	325, 12, 92	200	12	8.5
6	(2.9, 95.6)	300, 12, 92	120	3	8.5

The central earthquake depth was considered to be 20 km, the fault width was taken to be 130 km throughout the rupture, and the rigidity was fixed at 45 x 10^9 N/m^2. This model yielded a total seismic moment of 6.76 x 10^{22} Nm, or an equivalent magnitude, Mw, of 9.16.

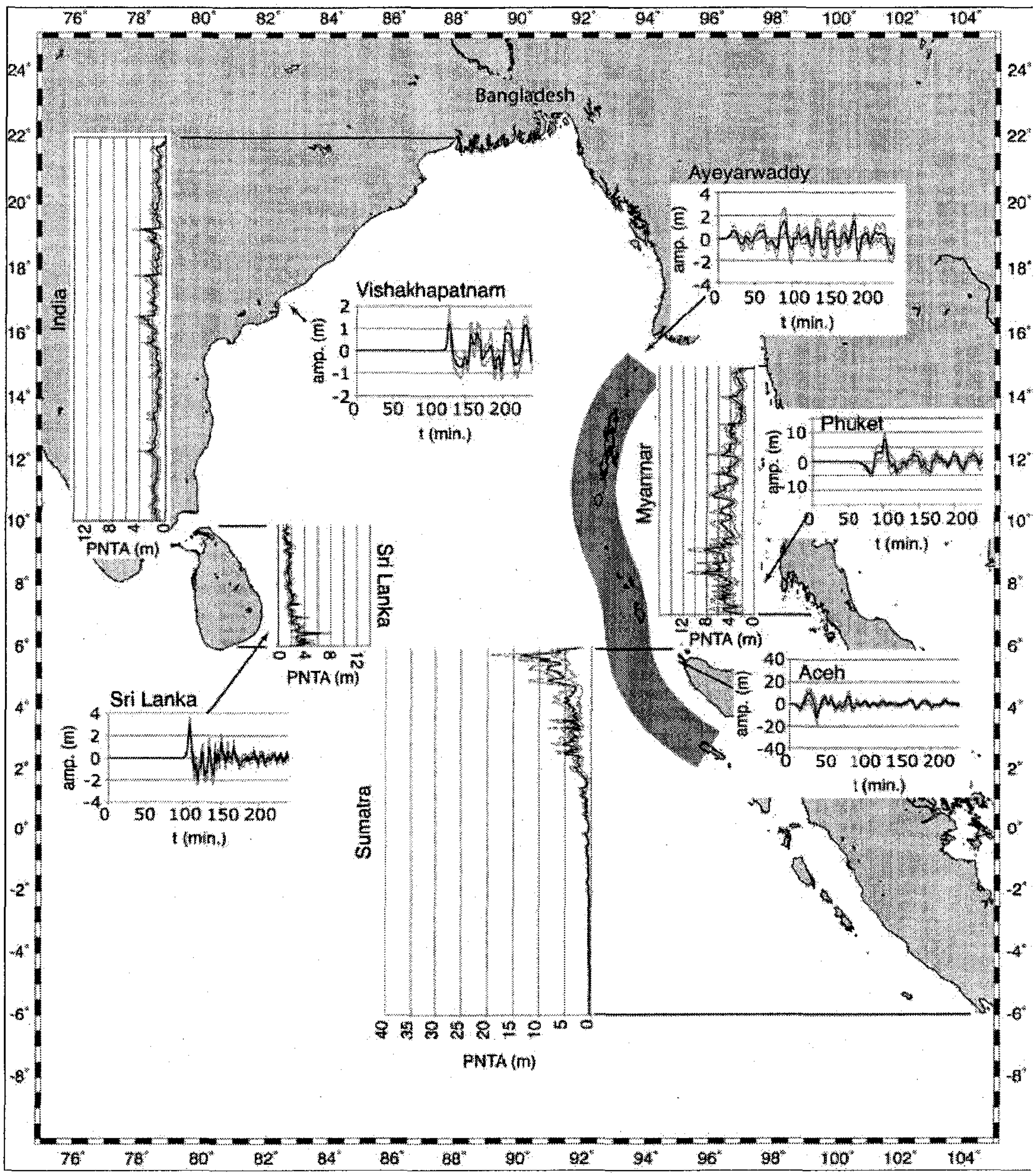

Figure 3-8: Peak nearshore tsunami amplitude and synthetic nearshore marigrams in the Bay of Bengal for the $\bar{u} = 9m$, $L = 1600km$ case ($Mw = 9.14$). Variations in nearshore tsunami amplitude are shown as a function of latitude for four coastlines (average, heavy line; extrema, light lines). Variations in marigrams (average, heavy line; extrema, light lines) for five representative locations also shown. (Geist *et al.*, 2007)

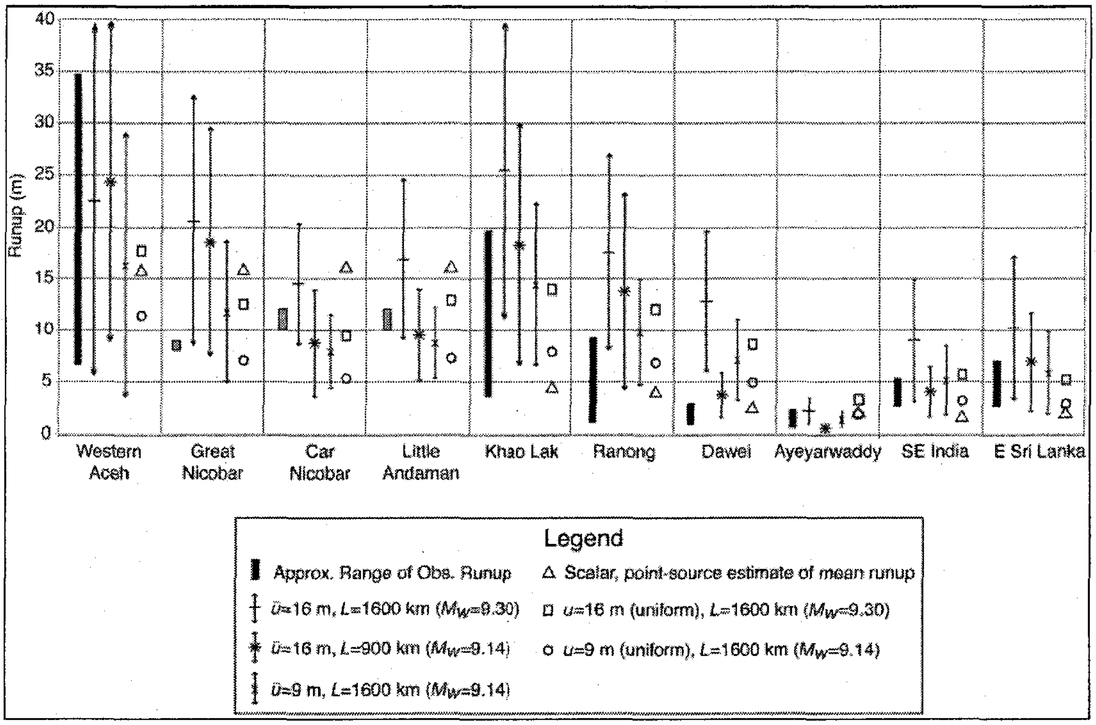

Figure 3-9: Comparison of tsunami run-up observations (black bars, gray for single location observations) with estimates from three sets of end-member source parameters using the stochastic source model. Modeled run-up is approximated by applying an amplification factor of 2 to the peak nearshore tsunami amplitudes. Range for each model is caused by variation in slip distribution patterns and propagation paths from subevents. Also shown for comparison are mean run-up estimates from Abe's (1995) expression (triangle) and mean run-up from uniform slip models: 9 m (circle) and 16 m (square). Approximate latitude range and reference for run-up surveys are as follows: western Aceh, 4.6^0–5.7^0 N (Borrero, 2005; Tsuji *et al.*, 2005; Jaffe *et al.*, 2006); Great Nicobar, Car Nicobar, and Little Andaman (Jain *et al.*, 2005); Khao Lak 8.3^0–9.2^0N (Tsuji *et al.*, 2006); Ranong, 9.2^0–10.0^0N, Dawei, 13.6^0–14.1^0N, and Ayeyarwaddy 15.7^0–15.8^0 (Satake *et al.*, 2006b); Southeast India 10.4^0–13.4^0 N (Yeh *et al.*, 2005); East Sri Lanka, 6.7^0–8.8^0 N (Liu *et al.*, 2005; Goff *et al.*, 2006).

Another generation mechanism, other than the conventional approach of determining the ocean surface displacement as a result of seabed motion, can be explained in terms of the balance of forces (Rivera *et al.,* 2006). Rivera *et al.* (2006) pointed out that a common approach in modeling the generation and propagation of tsunami waves can be based on the assumption of a kinematic vertical displacement of ocean water. The phenomenon is analogous to the ocean bottom displacement during a submarine earthquake and fits well with the use of a non-dispersive long-wave model for simulating its physical transformation as it radiates outward from the source region. Rivera *et al.* (2006) used a somewhat new generation mechanism and a highly dispersive wave model. The new generation model assumed that transient ground motion during the earthquake could accelerate horizontal currents with opposing directions near the fault line whose successive convergence and divergence generate a series of potentially destructive oceanic waves.

The new dynamic model incorporated the effects of the earthquake moment magnitude, the ocean compressibility (through the use of buoyancy frequency), the effects of focal and water depths, and the orientation of ruptured fault line in the tsunami magnitude and directivity.

For tsunami wave simulation, the nonlinear momentum-based wave model included essential wave propagation and transformation mechanisms such as refraction, diffraction, shoaling, partial reflection and transmission, back-scattering, frequency dispersion, as well as resonant wave-wave interaction. Using this model and a coarse-resolution bathymetry, the new mechanism was tested for the Indian Ocean tsunami of December 2004. A new flooding and drying algorithm, that considered waves coming from every direction, was also proposed for the simulation of the inundation of low-lying coastal regions.

Table 3-5 lists the source parameters used by Rivera *et al.* (2006)

Parameters	Description	Value
M_w	Moment Magnitude	9.1 (7.1 after 3 hours)
d_0	Focal Depth	10 km
ρ	Water Density	1025 kg/m^3
Δs	Distance in the slope term (width of disturbed area)	165 km
ν	Kinematic viscosity of seawater	0.0000122m^2/s
N_z	Buoyancy (Brunt-Vaisalla) Frequency	0.00713 /s
κ	Tuning parameter	0.5-

During a submarine earthquake, an upward force or pressure is exerted in the ocean column by the seabed (Figure 3-10). Similar to atmospheric pressure effect, this produces a horizontal pressure gradient which should accelerate currents opposite to the direction of the applied pressure gradient force (i.e. $\rho^{-1}\nabla P_e = a_x$, where ρ is water density, P_e, is seabed pressure and a_x is horizontal acceleration). It is postulated that a tsunami may occur if the prevailing downward force or pressure of the ocean column is exceeded by the pressure or force exerted by the seabed. Furthermore, it is also proposed that a seismic-induced pressure gradient force would accelerate currents across the fault. That is, a cross-fault current is generated as shown in Figure 3-10. The slope of the seabed may play an important role as it strongly affects the magnitude and direction of the induced currents. In the case of the 2004 Indian Ocean tsunami, the increasing water depths towards the west could mean that westerly currents are generated by the quake.

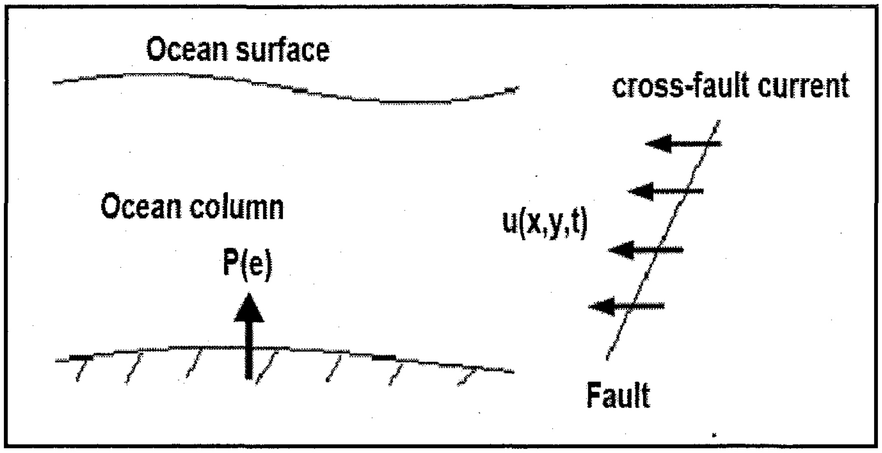

Figure 3-10: Schematic illustration of the proposed tsunami generation model (Rivera *et al.*, 2006)

Figure 3-10 implies that, if the earthquake moment magnitude is high enough, the pressure exerted at the ocean bottom may exceed the pressure exerted by the atmosphere and the water column. This in turn produces an excess pressure whose horizontal gradient (i.e. the pressure gradient force) and creates a horizontal acceleration of currents near the fault-line. The impulsive momentum of these horizontal currents and their succeeding convergence and divergence can produce a series of waves that radiate away from the source.

The tsunami generation mechanism that was proposed may be used to study the waves generated during volcanic eruptions or landslides. During these geologic events, ground accelerations can produce opposing horizontal ocean currents whose successive divergence and convergence can generate potentially destructive tsunami waves. It was assumed that the ocean currents produced by the ground motion oscillate at a frequency that is dependent on the local water depth and the gravitational acceleration. The oceanic currents produced during the submarine earthquake oscillate in time t can be written as:

$$\mu(x,y,t) = \kappa \alpha N_z t \frac{\Delta h}{\Delta s} \sin(\omega t) \tag{6}$$

where $\mu(x,y,t)$ is the magnitude of the induced horizontal current (m/s), κ is a non-dimensional tuning parameter, α is a variable that include factors related to both the seismic disturbance and the ocean column, N_z is the Brunt-Vaisalla frequency (or buoyancy frequency of the ocean column). $\frac{\Delta h}{\Delta s}$ is the bathymetric slope of the disturbed seabed, and ω is a local current frequency given by $\omega = \frac{2\pi}{T_c}$. Here, T_c is the period of current oscillation which is given by $\frac{1}{2}\sqrt{\frac{h}{g}}$ in which h is the water depth and g is gravitational acceleration.

The author of this thesis noticed that, with the proposed generation model, the observed features of the Indian Ocean tsunami, such as the initial drying of areas to the east of the source region and the initial flooding of western coasts, were correctly simulated. The formation of a series of tsunami waves with periods and lengths comparable to observations were also properly modelled with the new generation model. Furthermore, the shoaling behaviour of tsunami waves during flooding of coastal areas was also satisfactorily simulated through the use of the new wave run-up algorithm.

Puspito and Gunawan (2005) modeled the December 2004 Indian Ocean tsunami using a numerical model initially developed by Imamura *et al.* (1995) at Tohoku University, Japan. Generally speaking, there was good agreement between the calculated and observed travel times, whereas the computed tsunami heights were considerably smaller than the observed ones.

3.7. Critical analysis of the state-of-the-art about tsunami modeling research

Following an extensive literature review, the author of the present thesis identified that, although the validity of the shallow water approximation becomes more tenuous in the inundation and flooding regimes, these equations still perform surprisingly well at describing basic features of ocean flows, and are often the most efficient and least expensive practical models.

The Okada deformation model assumes a linear deformation of the Earth, coupled to ignoring initial wave current and instantaneous occurrence of the earthquake. These assumptions and simplification produce a big bias between the results generated from this model and observed data. Table 3-6 summarized the difference.

Notably, the traditional method only considers the initial wave amplitude; the latter method only considers initial wave current. Neither of these methods is satisfying. With requirements for more accurate results, neither Okada algorithm, nor the initial current model generate compelling solutions. Generation models should take into account both waves and currents. The smaller the bias of the source, the bigger the errors displayed in the propagation and inundation stage. Clearly, more concern should be devoted to tsunami generation modeling, and collaboration and team work is also needed as this requires multi-disciplinary expertise.

Table 3-6: Difference between assumptions of the Okada deformation model and real tsunami

No.	Okada Deformation Model	Real Tsunami
1.	Linear vertical deformation of the Earth	Nonlinear deformation of the Earth
2.	No horizontal deformation	Can be up to 3 times more important than the vertical component.
3.	The earthquake occurs simultaneously	Slow main-shock and lots of aftershocks
4.	The water is incompressible	The water is compressible
5.	The output is sinusoidal wave	Real tsunami waves are combination of short waves and long waves
6.	No initial wave current	Initial wave current
7.	One wave	A serials of waves
8.	Finite fault plane parameters	Unclear

The most basic information a tsunami warning center requires, is represented by the expected arrival times of the first tsunami wave at selected coastal locations originating from the area of tsunami generation. Almost always, the first wave in a tsunami event is not the wave with the greatest amplitude, nevertheless, tsunami travel time charts are generally constructed for the first wave, rather than for the wave with the highest amplitude. Advanced knowledge of travel times for the first wave, provides some additional valuable time for evacuation, if an evacuation is needed. Also, tsunami travel times can be pre-computed, independent of the seismic moment magnitude of the earthquake, only for the first wave. The advantage of this zero-order of approximation used to calculate tsunami travel time is that tsunami travel times to selected locations can all be pre-computed in advance. Since, at present one cannot predict precisely the location and time of occurrence of a tsunamigenic earthquake, it is not possible to construct tsunami travel time charts for all possible future tsunamis. In any case, travel time information is required for coastal locations, where disaster mitigation procedures have to be invoked during real tsunami events. The heights of the subsequent waves are not known till the event actually happens, and hence no predetermination of the travel time of the highest wave can be made.

CHAPTER 2

NUMERICAL MODELING OF TSUNAMI

4. INTRODUCTION

Until now, only the Indian Ocean tsunami of 26 December 2004 provided the most complete information and data needed for conducting tsunami research. This information includes earthquake fault plane parameter, satellite altimetry, tide gauge records and field survey data. By comparing expected data with measured ones, numerical models can be calibrated and validated. Thus, in the scientific literature after the 2004 Indian Ocean tsunami, all numerical models such as MOST, UAF, GEOWAVE, etc. were actively used by authors and researchers to validate their models. These validated tsunami models were then improved thereafter by analyzing the bias with observed data; in the long run, they were used to predict and simulate future potential tsunami events. In this chapter, tsunami travel times were obtained using the MIRONE model and then calibrated with observed data. The travel times were also calculated using another numerical model – GEOWARE. The 2004 Indian Ocean tsunami was analyzed using the authoritative fault plane mechanism of NOAA and the numerical results were calibrated using collected tide gauge records. Then, the calibrated MIRONE models were used to simulate two other tsunami events, namely, the Makran Subduction Zone tsunami in part 7 and Cascadia Subduction Zone tsunami in part 8, respectively. This model represents better the oscillatory wave trains that were observed during the event. The comparison of the model results with observations at tide gages shows the simulations are in good agreement with collected data. The general flowchart shows in Figure 4-3.

4.1. The MIRONE numerical model – Theoretical framework

MIRONE, nonlinear shallow water based model, is a suite of integrated numerical codes designed for simulating tsunami generation, propagation and subsequent run-up onto the shoreline. MIRONE is authored by a geophysicist, Joaquim Luis, from University of Algarve, Portugal. The nonlinear, shallow water, long wave code SWAN (Mader *et al.*, 2004) has been embedded to model the propagation of a tsunami wave. The resulting shoaling, flooding and coastal amplification of the tsunami waves are modeled by the embedded TSUNAMI N_2 model. TSUNAMI N_2 is authored by Professor Fumihiko Imamura from Tohoku University, Japan. MIRONE is a Windows and MATLAB-based framework tool that allows the display and manipulation of a large number of grids format through its interface with the GDAL library. Its main purpose is to provide users with an easy-to-use graphical interface to the more commonly used programs of the GMT package. However, it also suffers from important limitations — speed and especially memory consumption are the most important ones.

In order to simulate the tsunami generation and propagation, the equations of motion and continuity were formulated in spherical polar coordinates (Luis *et al.* 2005). λ, ϕ and R, are defined as the longitude, the latitude and the distance from the Earth's center, respectively. If the origin of the system is located on the ocean surface, it is more suitable to introduce a vertical coordinate $Z = R - R_0$. Here, R_0 is the radius of Earth which is assumed to be equal to 6,370km. Because the Earth is not a perfect sphere, the equations given below describe better the large scale motion relative to the geo-potential and not to the spherical surfaces. For further discussion of this problem the reader is directed to Grill *et al.* (1982). The vertically-averaged equations of motion and continuity in the spherical system are expressed as:

$$\frac{\partial u}{\partial t} + \frac{u}{R_0 \cos\phi}\frac{\partial u}{\partial \lambda} + \frac{v}{R_0}\frac{\partial u}{\partial \phi} - (2\Omega + \frac{u}{R_0 \cos\phi})v \sin\phi = -\frac{g}{R_0 \cos\phi}\frac{\partial \zeta}{\partial \lambda} - \frac{\tau_\lambda^b}{\rho_0 d} \tag{7}$$

$$\frac{\partial v}{\partial t} + \frac{u}{R_0 \cos\phi}\frac{\partial v}{\partial \lambda} + \frac{v}{R_0}\frac{\partial v}{\partial \phi} + (2\Omega + \frac{u}{R_0 \cos\phi})v \sin\phi = -\frac{g}{R_0}\frac{\partial \zeta}{\partial \lambda} - \frac{\tau_\phi^b}{\rho_0 d} \tag{8}$$

$$\frac{\partial \zeta}{\partial t} - \frac{\partial \eta}{\partial t} + \frac{1}{R_0 \cos\phi}\frac{\partial ud}{\partial \lambda} + \frac{1}{R_0 \cos\phi}\frac{\partial (dv\cos\phi)}{\partial \phi} = 0 \tag{9}$$

In the above equations, u is the velocity in the λ (E-W) direction, v denotes the velocity in the ϕ (N-S) direction, ζ is the sea level, η is the bottom displacement, t is the time, g is the Earth's gravitational acceleration (g=9.81 m/s^2), ρ is water density, and d is the total depth $d = H + \zeta - \eta$. The Coriolis parameter was taken to be $f = 2\Omega \sin\phi$, and it is a function of the Earth's angular velocity $\Omega = 7.29 \times 10^{-5} s^{-1}$ and of the latitude, ϕ. The components of the bottom friction force are nonlinear functions of velocity:

$$\tau_\lambda^b = ru\sqrt{(u^2+v^2)} \quad \text{and} \quad \tau_\phi^b = rv\sqrt{(u^2+v^2)} \tag{10}$$

To simplify the bottom friction terms in Eqs. (7) and (8), the following notation is introduced:

$$\frac{\tau_\lambda^b}{\rho_0 d} = \frac{ru\sqrt{(u^2+v^2)}}{\rho_0 d} = R_x u \qquad \frac{\tau_\phi^b}{\rho_0 d} = \frac{rv\sqrt{(u^2+v^2)}}{\rho_0 d} = R_y v \tag{11}$$

The dimensionless bottom friction coefficient, r, was taken equal to 3.3×10^{-3}.

In order to identify important steps in the construction of a global numerical code, basic numerical formulas for the spherical coordinate system were developed. The computation was conducted in a space staggered grid (C grid) as shown in Fig.4-1. The velocity grid points (u) denoted as horizontal bars are offset from the velocity grid points (v, vertical bars). Sea level grid points were denoted by crosses. The grid size (space step) along the E-W direction was $h_\lambda = R_0 \cos\phi\Delta\lambda$. Index $j = 1, n$ stands for space stepping along the parallels of latitude, thus the distance along the parallels was expressed as jh_λ. As the parallels of latitudes become very small circles near the poles, this geographical region needed to be either excluded from consideration or introduced into computation through a different map projection. Hence, the Poles were excluded from the computational domain in this thesis. The space step along the north-south direction is $h_\phi = R_0 \Delta\phi$. The index k stands for the space stepping along the meridians of longitude. Locations of grid points on the sphere are given by their j and k-coordinates. The u, v and ζ points are organized into triplets as shown by the triangles in Fig.4-1.

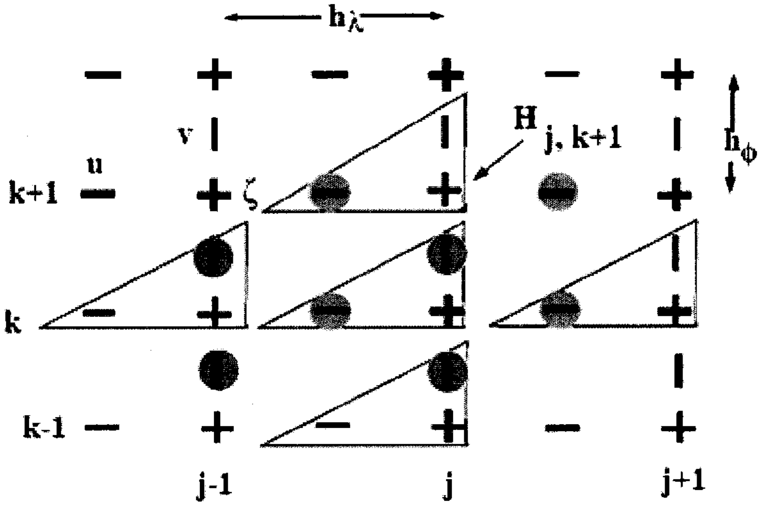

Figure 4-1: Spatial grid distribution in the spherical system of coordinates (Kowalik *et al.,* 2006)

The depth is defined at the sea level points. To resolve some terms in the equations of motion the v velocity is needed at the u locations and vice versa. For this reason the blue and red circles are introduced to explain how the averaged values are constructed. The four values given by blue circles, when averaged will define the averaged v velocity at the u point location. This point location is given by $u_{j,k}$. The average of v velocity at this location is

$$v^{-u} = \frac{1}{4}(v_{j,k-1} + v_{j,k} + v_{j-1,k} + v_{j-1,k-1}) \tag{12}$$

In a similar way the average u velocity (four reddish circles) at the $v_{j,k}$ point is

$$u^{-v} = \frac{1}{4}(u_{j+1,k} + u_{j+1,k+1} + u_{j,k+1} + u_{j,k}) \tag{13}$$

The solution of equations (7-9) is usually advanced in time by the two-time-level numerical scheme (Kowalik *et al.* and Murty *et al.* 1993, Imamura *et al.,* 1996). For the spatial derivatives, the second order of approximation is constructed.

$$\begin{aligned} u_{j,k}^{m+1} &= u_{j,k}^{m} - \frac{gT}{h_\lambda}(\zeta_{j,k}^{m} - \zeta_{j-1,k}^{m}) + Tv^{u,m} + \frac{T\tan\phi_k^{\zeta}}{R_0} v^{u,m} u_{j,k}^{m} - TR_{x,j,k}^{m} u_{j,k}^{m} - \frac{u_p^m T}{h_\lambda}(u_{j,k}^{m} - u_{j-1,k}^{m}) \\ &- \frac{u_n^m T}{h_\lambda}(u_{j+1}^{m} - u_{j}^{m}) - \frac{Tv_p^{u,m}}{h_\phi}(u_{j,k}^{m} - u_{j,k-1}^{m}) - \frac{Tv_n^{u,m}}{h_\phi}(u_{j,k+1}^{m} - u_{j,k}^{m}) \end{aligned} \tag{14}$$

$$v_{j,k}^{m+1} = v_{j,k}^{m} - \frac{gT}{h_\phi}(\zeta_{j,k+1}^{m} - \zeta_{j,k}^{m}) + Tfu^{u,m+1} - \frac{T\tan\phi_k^{v}}{R_0} u^{v,m} u^{v,m+1} - TR_{y,j,k}^{m} v_{j,k}^{m} - \frac{Tu_p^{v,m}}{h_\lambda}(v_{j,k}^{m} - v_{j-1,k}^{m})$$

$$-\frac{Tu_n^{v,m}}{h_\lambda}(v_{j+1,k}^m - v_{j,k}^m) - \frac{Tv_p^m}{h_\phi}(v_{j,k}^m - v_{j,k-1}^m) - \frac{Tv_n^m}{h_\phi}(v_{j,k+1}^m - u_{j,k}^m) \qquad (15)$$

$$\zeta_{j,k}^{m+1} = \zeta_{j,k}^m - \frac{T}{h_\lambda}(flux_{\lambda,j+1,k} - flux_{\lambda,j,k}) - \frac{T}{\cos\phi_k^\zeta}(flux_{\phi,j,k} - flux_{\phi,j,k-1}) + \eta_{j,k}^{m+1} - \eta_{j,k}^m) \qquad (16)$$

In this numerical approach the purpose was to construct the high order of approximation in space for the continuity equation. For this purpose Kowalik et al (2005) expanded the upwind/downwind flux code proposed by Mader *et al.* (2004). For large scale computations, the upwind/downwind is essential as it displays strong stability. The original code has been improved by an additional interpolation between the grid points. The resultant code given by equation 7 and 9 is close to the third order of approximation in space.

$$flux_{\lambda,j,k} = u_p^{m+1}(\zeta_{p,\lambda}^m - \eta_{j-1,k}^m) + u_n^{m+1}(\zeta_{n,\lambda}^m - \eta_{j,k}) + u_{j,k}^{m+1}\frac{H_{j,k} - H_{j-1,k}}{2} \qquad (17)$$

$$\zeta_{n,\lambda}^m = (0.5 + u_n^{m+1}\frac{T}{h_\lambda})\zeta_{j-1,\lambda}^m + (0.5 - u_n^{m+1}\frac{T}{h_\lambda})\zeta_{j,k}^m) \qquad (18)$$

$$\zeta_{n,\lambda}^m = (0.5 + u_n^{m+1}\frac{T}{h_\lambda})\zeta_{j-1,\lambda}^m + (0.5 - u_n^{m+1}\frac{T}{h_\lambda})\zeta_{j,k}^m) \qquad (19)$$

$$u_p^{m+1} = 0.5 \times (u_{j,k}^{m+1} + \left|u_{j,k}^{m+1}\right|) \text{ and } u_n^{m+1} = 0.5 \times (u_{j,k}^{m+1} - \left|u_{j,k}^{m+1}\right|) \qquad (20)$$

$$flux_{\phi,j,k} = \cos\phi_k^v[v_p^{m+1}(\zeta_{p,\phi}^m - \eta_{j,k}^m) + v_n^{m+1}(\zeta_{n,\phi}^m - \eta_{j,k+1}) + v_{j,k}^{m+1}\frac{(H_{j,k} + H_{j,k+1})}{2}] \qquad (21)$$

$$\zeta_{p,\phi}^m = (0.5 + v_p^{m+1}\frac{T}{h_\phi})\zeta_{j,k}^m + (0.5 - v_p^{m+1}\frac{T}{h_\phi})\zeta_{j,k+1}^m) \qquad (22)$$

$$\zeta_{n,\phi}^m = (0.5 + v_n^{m+1}\frac{T}{h_\phi})\zeta_{j,k}^m + (0.5 - v_n^{m+1}\frac{T}{h_\phi})\zeta_{j,k+1}^m) \qquad (23)$$

$$v_p^{m+1} = 0.5 \times (v_{j,k}^{m+1} + \left|v_{j,k}^{m+1}\right|) \qquad \text{and} \qquad v_n^{m+1} = 0.5 \times (v_{j,k}^{m+1} - \left|v_{j,k}^{m+1}\right|) \qquad (24)$$

Above, the wave period is T and the index m refers to the time step. The integration domain extends in latitude from 25^0S to 25^0N. The boundaries included both wet and dry points. Along the coastal (dry) points the normal velocity was set to zero. At the wet boundary points, (along 25^0S latitude) the radiation condition, established by Reid and Bodine in 1968, was used.

To demonstrate the pattern of the energy trapped over the various bathymetric features, Kowalik *et al.* (2005) considered the energy flux method. In the rectangular system of coordinates, with the x-coordinate along east-west direction and the y coordinate along north-south direction, the u component of the velocity along direction x could be combined with the sea level (ζ) in order to define the east-west component of the energy flux vector (Kowalik and Murty, 1993a):

$$E_x = \rho g H u \zeta \tag{25}$$

Similarly, the north-south component of the energy flux vector is defined (with v, the velocity component along the y-direction) as,

$$E_y = \rho g H v \zeta \tag{26}$$

where ρ is water density, g is Earth's gravity acceleration ($g = 9.81\,\mathrm{m/s^2}$), and H is the ocean depth. The energy flux vector for the progressive wave is always propagating into the same direction as the sea level velocity and its direction is perpendicular to the wave front. To preserve the direction of the energy flux in the case of progressive waves, the velocity and sea level elevation remain in phase (Henry *et al.* and Foreman *et al.*, 2001). Energy flux units represent energy flux per unit width and per unit time. In order to derive the total energy flux, the above expressions must be multiplied by the length of the cross-section and then integrated over the wave period.

To make sure that the results resemble the real situation, additional precautions as shown below are applied when using the shallow water models:

SOURCE – wave length must be 10 times longer than the depth.
PROPAGATION – wave length must be 40 times longer than deep ocean depth and period needs to be longer than 15 minutes.
RUN-UP – period needs to be longer than 15 minutes.
FLOODING – period needs to be longer than 10 minutes and the slope needs to be greater than 2 percent.

Wave equations solved by IOC, Tsunami N2 code are in the form of Saint-Venant:

$$\frac{\partial \eta}{\partial t} + \frac{\partial M}{\partial x} + \frac{\partial N}{\partial y} = 0; \quad M = u(h+\eta) = ud; \quad N = v(h+\eta) = vd \tag{27}$$

$$\frac{\partial M}{\partial t} + \frac{\partial}{\partial x}\left(\frac{M^2}{d}\right) + \frac{\partial}{\partial y}\left(\frac{MN}{d}\right) + gd\frac{\partial \eta}{\partial x} + \frac{gm^2}{d^{7/3}} M\sqrt{M^2+N^2} = 0 \tag{28}$$

$$\frac{\partial N}{\partial t}+\frac{\partial}{\partial x}\left(\frac{MN}{d}\right)+\frac{\partial}{\partial y}\left(\frac{N^2}{d}\right)+gd\frac{\partial \eta}{\partial y}+\frac{gm^2}{d^{7/3}}N\sqrt{M^2+N^2}=0 \qquad (29)$$

Where: M , N discharge fluxes in x - and y -directions per unit width. They are related to u and v ; $d=h+\eta$ is the total depth; $h(x,y)$ is still water depth; $\eta(x,y,t)$ is the surface displacement; m is the Manning roughness coefficient.

It is noteworthy that SWAN and TSUNAMI N_2 are two completely separate models which can simulate tsunami generation, propagation and inundation respectively. Dr. Luis combined these two models and chose the propagation model from SWAN and the inundation model from the TSUNAMI N_2. Recently developed TSUNAMI N_2 was renamed as the TWO-LAYERS Model by Imamura. At the present stage, this model was not available to us. The MIRONE model was used to simulate tsunami propagation in the present thesis.

4.2. Techniques of numerical modeling for tsunami propagation

It has long been a goal of coastal engineers to produce a computational wave model that is capable of accurately simulating wave motion from deep water, through the surf zone, to shoreline. To do this, a hydrodynamic model would have to include, among others, nonlinear shoaling, refraction, diffraction, wave-wave interaction, breaking, and wave run-up. As it is currently impractical to introduce the full solution of the Navier-Stokes equations over any significant physical domain at ocean level, approximate models must be used. For tsunami modeling, the numerical difficulties lie in the diverse spatial scales of these flows. On the deep ocean, tsunami wavelengths are often on the order of several hundred kilometers, requiring thus a large computational domain. In the near shore region tsunami energy is compressed and focused by bathymetry in often unpredictable ways, requiring grid spacing that is orders of magnitude smaller. That is to say, numerical model have to be able to model global propagation and local inundation simultaneously. Based on the above analysis, and considering the planetary ocean bathymetry and topography as an example, at least five aspects must be taken into account.

4.2.1. Boundary conditions

To obtain solutions of the wave propagation over a finite domain, appropriate boundary conditions have to be specified in the numerical model. For a perfectly reflective vertical wall, the horizontal velocity normal to the wall is always zero. The corresponding values of the surface elevation and the tangential velocity, in theory, could be obtained from the governing equations. For the nearshore areas, boundaries include both wet and dry points. Along the coastal (dry points) the normal velocity is set by zero. Even with the relatively large space step, the new dry and wet points may be generated due to run-up or run-down. So a numerical scheme for the wetting and drying needs to be introduced. The total depth ($D+\zeta-\eta$) is usually taken as the parameter to be tested for the presence of the wet or dry points (Flather *et al.* and Heaps *et al.* (1975); Imamura *et al.* (1996)). The wet and dry points are identified by setting the average (undisturbed) ocean depth as positive (wet points) and elevations (dry points) as the negative values. The total depth in the dry grid points is taken as zero $d = D+\zeta = 0$. A simple run-up condition was hence used. The following steps were taken when the dry point ($j_{wet}+1$) was located to the right of the wet point j_{wet}.

$$IF(\zeta^{m}(j_{wet}) > -H(j_{wet}+1)), \quad \text{then} \quad u^{m}_{j_{wet}+1} = u^{m}_{j_{wet}} \tag{30}$$

If wetting is possible (as indicated by the above condition), the velocity from the wet point is extrapolated to the right (dry point), but sea level is calculated using the equation of continuity. The model has been calibrated and tested by comparing it with analytical solutions, as well as through laboratory experiments. Setting a movable, vertical wall boundary conditions diminish the reflective wave in coastal areas. The boundary condition will be used to calculate the inundation along the coastal zone.

To illustrate the moving boundary algorithm, the one-dimensional case is used as an example. As shown in Figure 4-2, the real bathymetry has been replaced by a staircase representation. The total depth, H, is calculated and recorded at grid points $i-1$, i and $i+1$, while the volume flux is computed at grid points $i-\frac{1}{2}$, $i+\frac{1}{2}$ and $i+\frac{3}{2}$. As shown in Figure 4-2(a), the i - th cell is a wet cell in which the total depth is negative and the volume fluxes are zero. The shoreline is somewhere between the i - th and the $i+1$ - th grid points. Then, the volume flux at the $i+\frac{1}{2}$ - th grid point is assigned to be zero. Therefore, the shoreline does not move to the on-shore direction. When the water surface is rising as shown in Figure 4-2(b), however, the volume flux at the $i+\frac{1}{2}$ - th grid point is no longer zero. The shoreline may move one grid point to the on-shore direction. After the total depth has been updated from the continuity equation, the following algorithm is used to determine whether or not the shoreline should be moved. If $H_i > 0$, possible cases can be summarized as:

① If $H_{i+1} \leq 0$ and $D_{i+1} + \zeta_i \leq 0$, then the shoreline remains between grid points i and $i+1$, the volume flux $P_{i+\frac{1}{2}}$ remains zero;

② If $H_{i+1} \leq 0$ and $D_{i+1} + \zeta_i > 0$, then the shoreline moves to between grid points $i+1$ and $i+2$, the volume flux $P_{i+\frac{1}{2}}$ may have a nonzero value, while $P_{i+\frac{3}{2}}$ is assigned to be zero. The flooding depth is $H_f = D_{i+1} + \zeta_i$;

③ If $H_{i+1} > 0$, then the shoreline moves to between grid points $i+1$ and $i+2$. The volume flux $P_{i-\frac{1}{2}}$ may have a nonzero value, while $P_{i+\frac{3}{2}}$ has a zero value. The flooding depth is $H_f = \max(D_{i+1} + \zeta_i, D_{i+1} + \zeta_{i+1})$;

In the above cases, the time-step index has been omitted for simplicity. The algorithm is developed for a two-dimensional problem and the corresponding y-direction algorithm has the same procedure as that for the x-direction.

To save computing time, the regions that represent permanent dry (land) can be excluded from the computation by installing a depth criterion. Moreover, when H is very small, the associated bottom friction term become very large and, accordingly, a lower bound of the water depth is used to avoid the difficulty. The finite difference approximation for the continuity equation correctly accounts for positive and zero values of the total depth on each side of a computational grid. The treatment of flooding and ebbing grid cells guarantees mass conservation while accounting for the flooding and ebbing of land. The occurrence of a zero value for the total depth H on one side of a cell implies zero mass flux until H becomes positive. A grid cell is considered a dry cell only if the total water depths at all sides are zero or negative.

(a) Case 1

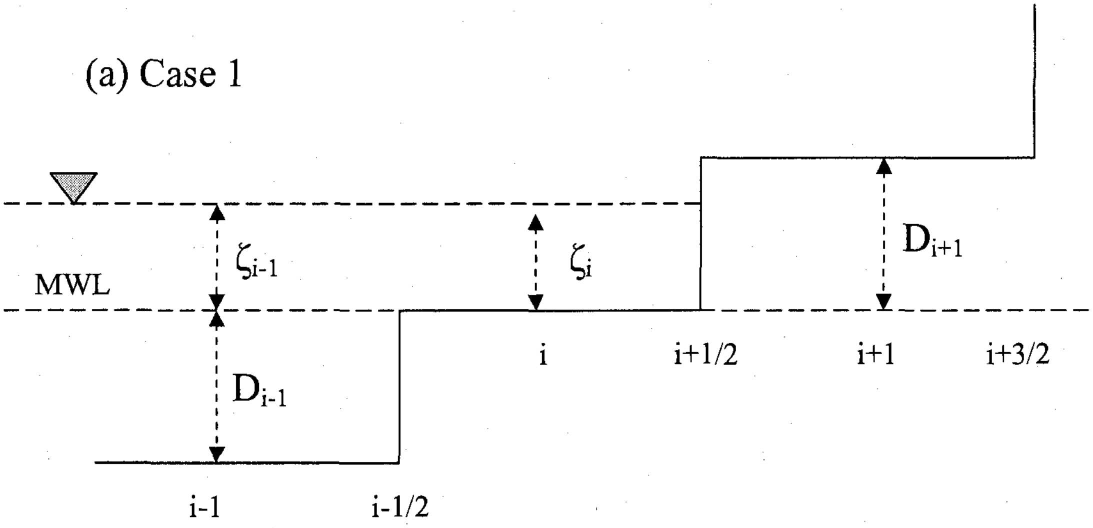

(b) Case 2

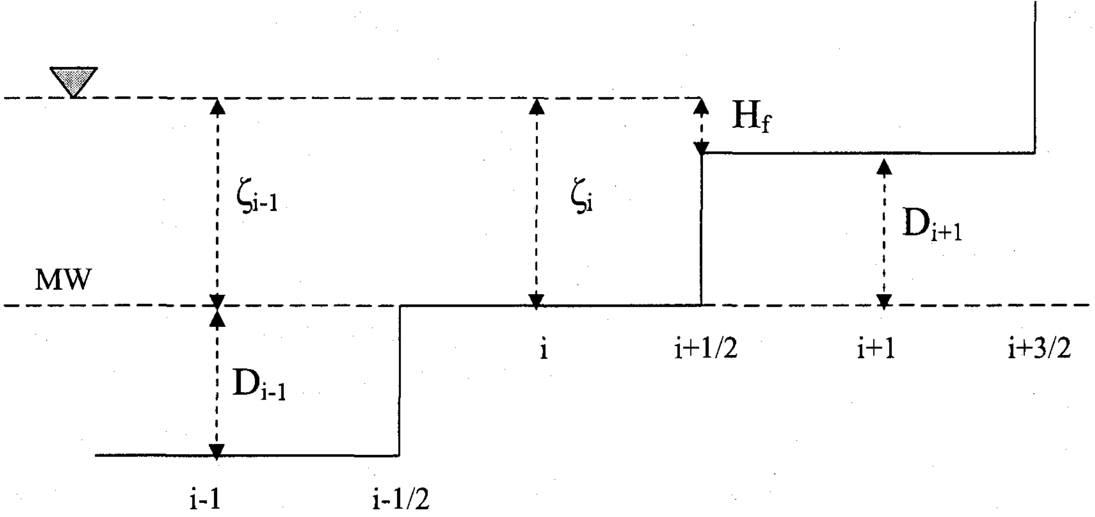

Figure 4-2: A schematic sketch of moving boundary treatment

In the open sea boundary, several different conceptual methods were introduced. Continuous boundary conditions are based on the conservation of mass. The physical meaning is what goes out from the boundary equals what comes in from the boundary. The standard SWAN code does a linear extrapolation at a continuous boundary which works if the wave arrives at the boundary simultaneously — however it will send back a false wave if the arriving wave is curved, hence there displays a reflective wave. MIRONE software adopted another method to diminish the reflective wave. A cosine curve was used on arrays to diminish the water depth. Because wave speed depends on $\sqrt{gh}$, at small depths the wave runs very slowly. MIRONE uses this fact to construct an imaginary border at which the depth gradually goes to zero. Ideally in this way the wave never reaches the border and therefore is not reflected. Another concept which also was widely used in numerical modeling is a standard strategy to place the boundaries far from the site of interest, so that the boundaries are far removed from the source of the wave and the wave has decayed before it arrives at a continuum boundary. But this strategy greatly increases computational demands, and it may not be appropriate for larger region and long-term simulations. An absorbing boundary condition, also called radiation boundary condition, which was established by Reid *et al.* and Bodine *et al.* (1968), allowed waves to propagate out of the domain with minimum reflection. Its physical meaning is that the outgoing waves should be absorbed by the computational boundary, so that no artificial reflections are sent back into the interior. These boundary conditions typically involve a wave velocity, since the goal is to simulate the outward movement of waves. The radiation conditions are taken at the open ocean boundaries:

$$U_{j,k}^{m} = \pm d_{j,k}^{m-1}\sqrt{\frac{g}{D_{j,k}}} \tag{31}$$

$$V_{j,k}^{m} = \pm d_{j,k}^{m-1}\sqrt{\frac{g}{D_{j,k}}} \tag{32}$$

Where: U — velocity in x direction (i index); V — velocity in y direction (y index);
d — total water depth; D — water depth; g — gravity.

This situation creates difficulties in cases where the waves are dispersive. Dispersive waves are characterized by the presence of two different wave velocities: the phase velocity and the group velocity, and each of these velocities can vary with wave number and wave frequency. Up until now, boundary conditions have been successfully constructed in numerical models.

4.2.2. Cyclic boundary condition

Since the globe is a spheroid in geographical meaning, when the entire globe is cut along meridian longitude, the huge computational domain requires a cyclic boundary condition for the sea level and the E-W velocity on this meridian. One must choose the latitude/longitude boundaries of his custom grid in degrees and minutes. Precision is to the nearest minute. Latitudes must be between 90^0 North and 90^0 South. Longitude values must be between 180^0 west and 180^0 east. The grid may not cross both 0^0 and 180^0. If one wishes his grid to span the entire globe longitudinally (only relevant for the case of the ETOPO2 Global Topography), one can choose bounds of 180^0W to 180^0E, or from 0^0E to 0^0E. Therefore, a strong background of geography is needed and the knowledge of bathymetry and topography is a must. As parallels of latitudes become very small circles near the poles, this geographical region needs to be either excluded from consideration or introduced into computation through a different map projection. Meanwhile accurate bathymetry is not available at the North Pole, so that the maximum calculation domain ranges from 80^0 in the South to 84^0 in the North.

4.2.3. Bottom friction and Coriolis force

All numerical codes consider bottom friction and the Coriolis force effect. In reality, when the computation domain is small, the Coriolis force is ignored as it only has a secondary effect on tsunami waves. For global tsunami propagation, Kowalik used the 2 minutes ocean bathymetry to simulate the 2004 Indian Ocean tsunami propagation into the three oceans and did include the Coriolis force. The results demonstrated that the Coriolis force has an important effect on the tsunami wave. Also due to the difficulty of deciding a value for the bottom friction coefficient, all models neglect bottom friction and currently only an upper limit for flooding can be obtained without a realistic friction model.

4.2.4. Model schemes

Model schemes are based not only on finite difference, but also on finite volume and finite element algorithms. Each approach has certain advantages and disadvantages. Finite difference algorithms are widely used in contemporary tsunami numerical models with upwind and downwind schemes. Finite volume offers the best stability and efficiency, finite element models offer the best geometric flexibility, while finite differences are the simplest to work with.

4.2.5. Nested-grid schemes

Numerical difficulties associated with simultaneously modeling global propagation and local inundation are due to diverse flow regimes. Globe scale tsunami waves move throughout the entire domain, needing various levels of refinements at different times and locations. Nested-grid schemes, also called adaptive mesh refinement, allow a very coarse grid to cover parts of the domain where no significant waves are present. They also allow higher refinement levels to track moving waves in deep ocean by using an algorithm in which set moving sub-grids may appear or disappear at any time. As waves approach the shoreline and get compressed by the sea bottom, higher refinement level grids appear to be capable of capturing the inundation and run-up. SWAN model uses a relay method that transmits the wave signals from the source to shore area. But wave signals can spread and radiate out to all directions, so that only partial wave signals and energy, which dominated in the former process, were included at each of the subsequent steps. This is because the relay method obtained wave signal only from one direction, which lead to underestimate of the wave height.

The parameters which users have to figure out and input into MIRONE model are listed below:

Sumatra case, grids at 2 minutes of arc spacing

6.0	dt (time step (s) for simulations)
50	grn (save grids at this cycle interval (it depends on dt))
0.0	cf (Coriolis)
0.0	cc (bottom stress of de chezy)
0.0	sfx (x wind stress)
0.0	sfy (y wind stress)
1	polar (polar=0 no polar; 1 north lat; -1 south lat; 2 Mercator)
1.0	rough (coefficient for FLOODING = actual height/ideal height; 1.0 no roughness)
10	cumint (cumint * dt = time at which the virtual tide gauges are writen - only used with -T option)
0.0	pistal
0.0	pistbl
0.0	pistab
0.0	pistbb
0.0	pistar
0.0	pistbr
0.0	pistat
0.0	pistbt
#	(ind 1 for piston, 2 for continuative, 3 for reflective in order of left,bottom,right,top of rectangle)
2	indl
2	indb
2	indr
2	indt
0	iopt (0 for extrapolated continuative boundary; 1 for linear continuative boundary)

4.3. GEOWARE model introduction and its application

The GOEWARE software was provided by Geoware Ltd. of Honolulu, USA (www.geoware.com). The simulation is based on the shallow water approximation for gravity waves; no wave diffraction or other hydrodynamic effects are currently included. The ETOPO2 oceanic bathymetry with a resolution of 2 minutes of arc is the input data and the output is represented by the tsunami travel time contours in hours. Travel times were obtained from the computation of the arrival of the first significant wave, starting from the Green-Du Boys formula (1978) which is generally valid for the propagation of long gravity waves, $c = \sqrt{gD}$. Here, c is the propagation speed, g is acceleration due to gravity, and H is the water depth. The distance from the epicenter at time T, is a function of the angle, α, and can be calculated by integrating the above equation

$$s(\alpha,T) = \int_{0}^{T} \sqrt{gh(x)}dx \qquad (33)$$

where x is the generic coordinate along a radius starting from the epicenter. The operation is repeated until the required time is elapsed. It is therefore possible to draw iso-time lines, which represent the position of the wave at that particular time. The package contains two programs (ttt and ttt_pick) which calculates tsunami travel times and sample the grid at given locations, respectively. The TTT (Tsunami Travel Times) programs calculate the first-arrival travel times on a grid for a tsunami generated at a given epicenter. Accurate topography and bathymetry are the key parameters which affect results. TTT comes with preprocessed bathymetry grids of spherical 2 minutes, 5min, 10min, 15min, 20min and 30min of arc in the world ocean which are derived from the bathymetry resource data of ETOPO2 and ETOPO5. The technique used to compute travel times over the entire grid is an application of Huygens principle which states that all points on a wave-front are point sources for secondary spherical waves. From the starting point, times are computed to all surrounding points. The grid point with minimum time is then taken as the next starting point and times are computed from there to all surrounding points. The starting point is continually moved to the point with minimum total travel time until all grid points have been evaluated. Several scripts (Bourne shell and DOS batch jobs) illustrate how to make graphs such as color images and contour maps from the travel times, using the Generic Mapping Tools (GMT) software. One problem of this model is that it does not take wave diffraction into account; i.e. it does not curve the wave front round obstacles, hence when the wave hits an island, it appears to shadow casts behind. Also the GEOWARE model is a DOS system based model. The commands and process used in the current thesis are as follows:

```
C:\Geoware\ttt\data>ttt ind_topo_2m.i2 -Tttt_ind_2m.b -E92.61/4.61 -N64 -S -V
Normalization factor = 0.999197
C:\Geoware\ttt\data>ttt ind_topo_5m.i2 -Tttt_ind_5m.b -E92.61/4.61 -N64 -S -V
Normalization factor = 0.999197
C:\Geoware\ttt\data>ttt ind_topo_10m.i2 -Tttt_ind_10m.b -E92.61/4.61 -N64 -S -V
Normalization factor = 0.999197
C:\Geoware\ttt\data>ttt ind_topo_15m.i2 -Tttt_ind_15m.b -E92.61/4.61 -N64 -S -V
Normalization factor = 0.999197
C:\Geoware\ttt\data>ttt ind_topo_20m.i2 -Tttt_ind_20m.b -E92.61/4.61 -N64 -S -V
Normalization factor = 0.999197
C:\Geoware\ttt\data>ttt_pick -Gttt_ind_2m.b=1 stations.d > traveltime-2.d -V -H
ttt_pick: Sampled 33 points from grid ttt_ind_2m.b=1 (4201 x 3001)
C:\Geoware\ttt\data>ttt_pick -Gttt_ind_5m.b=1 stations.d > traveltime-5.d -V -H
ttt_pick: Sampled 33 points from grid ttt_ind_5m.b=1 (1681 x 1201)
C:\Geoware\ttt\data>ttt_pick -Gttt_ind_10m.b=1 stations.d > traveltime-10.d -V -H
ttt_pick: Sampled 33 points from grid ttt_ind_10m.b=1 (841 x 601)
C:\Geoware\ttt\data>ttt_pick -Gttt_ind_15m.b=1 stations.d > traveltime-15.d -V -H
ttt_pick: Sampled 33 points from grid ttt_ind_15m.b=1 (561 x 401)
C:\Geoware\ttt\data>ttt_pick -Gttt_ind_20m.b=1 stations.d > traveltime-20.d -V -H
ttt_pick: Sampled 33 points from grid ttt_ind_20m.b=1 (421 x 301)
```

The GEOWARE model was also used to calibrate the calculated tsunami travel times derived from the MIRONE Model. A careful check found that GEOWARE and MIRONE are based on the same concept and theory with respect to calculating the tsunami travel time. Thus, the calculated tsunami travel times from the two models can be verified against each other, and also, they can be compared with observed travel times.

Figure 4-3: Numerical modeling procedures of flowchart

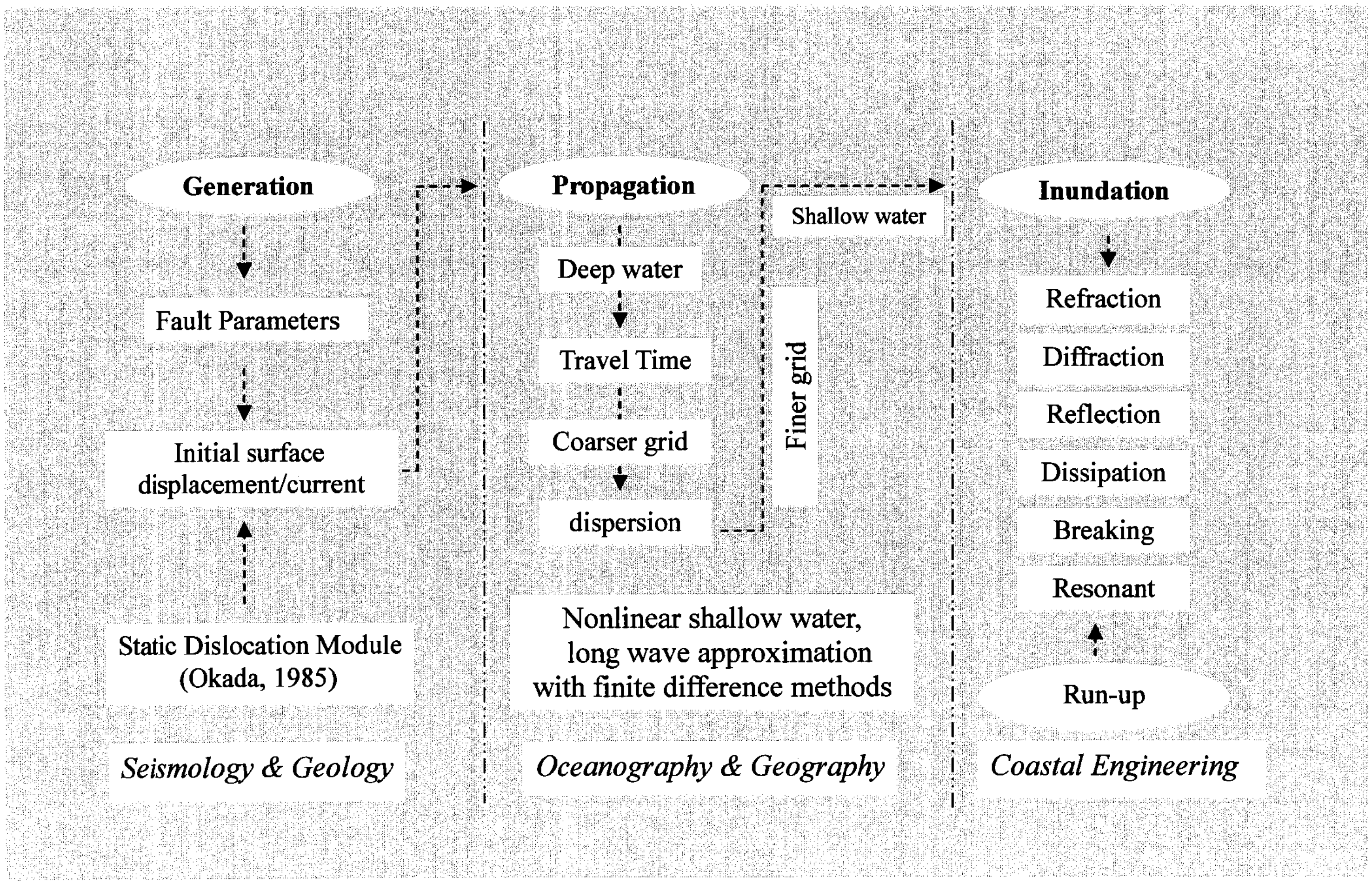

5. BATHYMETRY AND TOPOGRAPHY

All bathymetry and topography database used in the thesis can be found and downloaded from the NGDC website http://www.ngdc.noaa.gov/mgg. GEBCO bathymetry is available from the website http://www.nbi.ac.uk/bodc/gebco.html on behalf of the International Hydrographic Organization. During 1988 the National Geophysical Data Center (NGDC) decided to integrate its collection of worldwide aeromagnetic survey data into the already existing GEODAS (GEOphysical DAta System) data management system. GEODAS is an interactive database management system developed by the NGDC for use in the assimilation, storage and retrieval of geophysical data. The data included digital sounding data, digitized contour line data and previously grided products from a variety of sources: Marine Trackline Geophysical Survey Data, Hydrographic (bathymetric) Survey Data, Aeromagnetic Survey Data and GEODAS Girded Data including ETOPO2 Global Bathymetry, US Coastal Relief Model and Great Lakes Bathymetry. Digitized bathymetry for the World Ocean at a scale varying from 1:10 million to 1:500,000 depending on data density is available. A collection of varying resolution bathymetry grids, ranging from a global 30 minutes grid (ETOPO30), to a global 2 minutes grid (ETOPO2) are used in the numerical model. The horizontal datum is WGS84 and the vertical datum is mean sea level. ETOPO5 was generated from a digital data based on land and sea-floor elevations, on a 5-minute latitude/longitude grid. The resolution of the grided data varies from true 5-minutes for the ocean floors, the USA, Europe, Japan, and Australia, to 1 degree in data-deficient parts of Asia, South America, northern Canada, and Africa. Data sources for ocean areas are as follows: U.S. Naval Oceanographic Office; USA, W. Europe, Japan/Korea: U.S. Defense Mapping Agency; Bureau of Mineral Resources of Australia; Department of Industrial and Scientific Research of New Zealand; balance of world land masses: U.S. Navy Fleet Numerical Oceanographic Center. ETOPO2 (Smith and Sandwell, 1997), the grided data of global ocean depth from bathymetry soundings and satellite gravity data, are less reliable in the shallow ocean. All depth values less than 500 m were eliminated since no other data describe the regions of the slope and rise.

The Smith & Sandwell database is a worldwide set of 2-minutes girded ocean bathymetry derived from 1978 satellite radar altimetry of the sea surface. The version contained in ETOPO2 is 8.2. The ETOPO2, with cell centered-registration, has the number of cells: 5,400 rows of data (180 x 30), each with 10,800 columns of data (360x30). For survey-based data searches by geographic area, year of survey, source, platform/project, survey identifier, or data type are available. The data in GEODAS databases are of the best quality NGDC can obtain. Most of them have gone through extensive processing at their place of origin. The data records present geophysical data with corresponding times and positions. Documentation that varies within the survey is also included with the data records. GEODAS Gridded Databases come with software with which the user can create custom grids. One may change the cell size of his custom grid from that of the source Grid Database. However, the cell size must be a multiple of the source database cell size. Be aware that cell size and area are related and certain combinations will not work. For example, if one choses a latitude/longitude bounds minutes value of an odd number (e.g. 3 minutes), one would not be able to have a cell size of 2 minutes.

In conclusion, at present, the world ocean bathymetries which are widely used are derived from ETOPO5 or ETOPO2 respectively. Depending on our source Grid Database and our output Grid Cell Size, we may be restricted in our boundaries. Initial values for a particular source Grid Database are the outer bounds of that database. Extending bounds beyond that will only result in the extra cells being filled with the Empty Grid Cell value. The widely acceptable ETOPO2 bathymetry is the most accurate one available for the Indian Ocean. In North America, the best ocean bathymetry could be ETOPO1. So, in the context of the present thesis, ETOPO2 database was used to simulate the 2004 Indian Ocean Tsunami and the Arabia Sea Tsunami while ETOPO1 database was used to simulate the Cascadia Potential Tsunami.

6. NUMERICAL MODELING OF THE DECEMBER 26, 2004 INDIAN OCEAN TSUNAMI

The 2004 Sumatra-Andaman earthquake, with a magnitude ranging from 9.0 to 9.3 (accepted values by the Pacific Tsunami Warning Center), originated in the Indian Ocean, just north of the Simeulue island, off the western coast of northern Sumatra, Indonesia. This region is located at the extreme west end of the "Ring of Fire", an earthquake belt that accounts for 81 percent of the world's largest earthquakes. The earthquake occurred at 00:58:53 UTC (07:58:53 local time) on December 26, 2004. This devastating earthquake occurred due to thrust-faulting on the interface of the India plate and the Burma microplate with a vertical uplift of 5.0 to 10.0 m of the ocean floor. This created a massive tsunami with wave run-ups reaching up to 40 meters and killed more than 210,000 people, making it the deadliest disasters in modern history. The resulting tsunami devastated the shores of Indonesia, Sri Lanka, South India, Thailand and other countries around the Indian Ocean. It caused serious damage and deaths, as far as the east coast of Africa, with the farthest recorded death due to this tsunami occurring at Port Elizabeth in South Africa, some 8,000km away from the epicenter.

6.1. Geography and wave climates in the Indian Ocean

Among the four oceans, only the Indian Ocean does not extend into higher latitudes of the northern hemisphere; as the northern part of the Indian Ocean ends with the Bay of Bengal on its eastern side and with the Arabian Sea on its western side. The Arabian Sea, in turn, ends in its two marginal seas, namely, the Persian Gulf and the Red Sea. Compared to the Pacific Ocean, the Indian Ocean is much smaller in size, so that, usually, it is the second or the third wave in a tsunami wave train that has the highest amplitude. The highest wind wave amplitudes occur in the Indian Ocean and tsunami waves can extract energy from the wind waves through Reynold's eddy stresses and further grow to larger amplitudes (Murty *et al.*, 2005).

Table 6-1 lists the maximum storm surge heights and astronomical high tide above mean sea level for the Indian coast. Even though rare, occasionally, a tsunami can occur at the same time a storm surge is generated due to a tropical or extra-tropical cyclone. This can lead to even bigger wave heights, causing thus even more destruction.

Table 6-1: Natural hazards data for the coast of India (*India Coastal Engineering Code*)

Multi Hazard Data for West Coast of India			
Name of Coast State	Maximum Storm Surge Heights (m)	Astronomical High Tide above Mean Sea Level (m)	Flood Proneness (m)
Gujarat	2.5 – 5.0	1.1 – 4.1	10 – 12
Dadra & Nagar Haveli	5.0	1.9	*
Daman & Diu	5.0	1.1	*
Maharashtra	2.9 – 4.2	1.9	*
Goa	3.4	1.0	*
Karnataka	3.2 – 3.7	0.8	*
Kerala	2.3 – 3.5	0.8	3 – 5
Multi Hazard Data for East Coast of India			
Name of Coast State	Maximum Storm Surge Heights (m)	Astronomical High Tide above Mean Sea Level (m)	Flood Proneness (m)
Tamil Nadu	2.7 – 6.0 (except 11.0 near Tondi)	0.5	7 - 10
Pondicherry	3.0 – 4.5	0.5	10
Andhra Pradesh	3.0 – 6.0	0.68	*
Orissa	2.7 – 9.8	0.9 – 1.40	*
West Bengal	12.0 – 12.5	2.6	*
Karnataka	3.2 – 3.7	0.8	*
Andaman & Nicobar	*	1.0	3 – 6

Note: * to be estimated

6.2. Indian plate tectonic features

About 225 million years ago, India was a large island still situated off the Australian coast, and a vast ocean (called Tethys Sea) separated India from the Asian continent. When Pangaea broke apart about 200 million years ago, India began to forge northward. By studying the history of the Tethys, scientists have reconstructed India's northward journey. About 80 million years ago, India was located roughly 6,400 km south of the Asian continent, moving northward at a rate of about 9 m a century. When India rammed into Asia about 40 to 50 million years ago, its northward advance slowed by about half. The collision and associated decrease in the rate of plate movement are interpreted to mark the beginning of the rapid uplift of the Himalayas. Because both these continental landmasses have about the same rock density, one plate could not be subducted under the other. The pressure of the impinging plates could only be relieved by thrusting skyward, contorting the collision zone, and forming the jagged Himalayan peaks (Fig 6.1). Historical earthquakes in the region are indicative of the active tectonic collision process that is taking place along the entire southern and southeastern boundary of the Eurasian plate as it collides with the Indian plate and adjacent microplates.

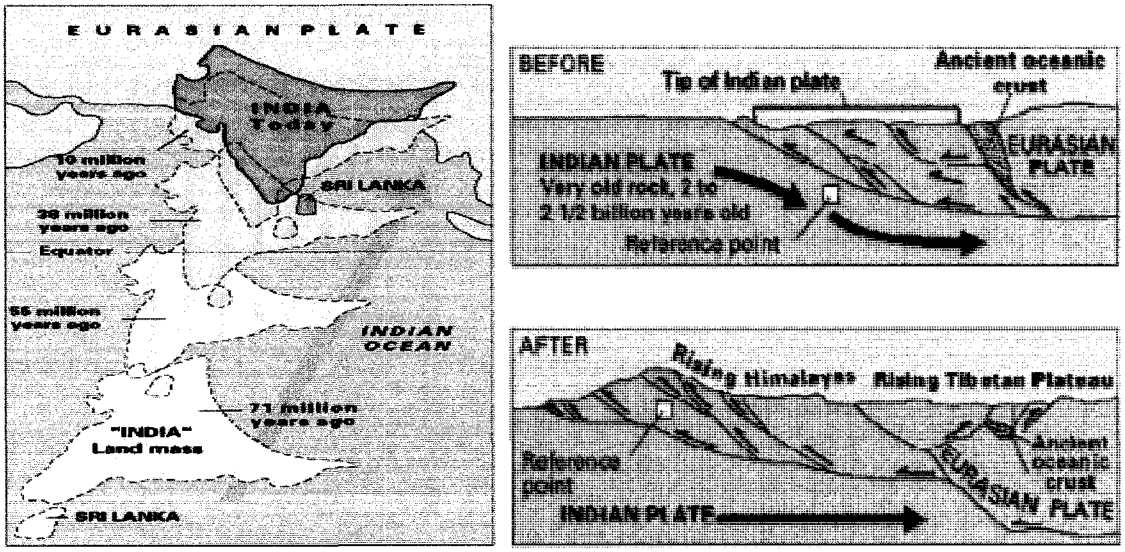

Figure 6-1: The India tectonic plate has been drifting and moving in a north/northeast direction, for millions of years colliding with the Eurasian tectonic plate and forming the Himalayan Mountains. (Source: USGS, 2006)

6.3. Sunda Subduction Zone (Andaman to Sumatra region)

Migration of the Indian tectonic plate and collision with the Eurasian tectonic plate has developed a diffuse zone of deformation and seismicity in the entire South Asia region. The India Plate is part of the great Indo-Australian Plate, which underlies the Indian Ocean and the Bay of Bengal, and is drifting northeast at an average of 6 cm/year. The India Plate meets the Burma Plate (which is considered a portion of the great Eurasian Plate) at the Sunda Trench. At this point the India Plate subducts under the Burma Plate, which carries the Nicobar Islands, the Andaman Islands and northern Sumatra. These structures are generally described as the Australia-Indian (or downgoing) plate subducting beneath the Asian (or overriding) plate, with a largely East-West direction of convergence. The Bay of Bengal consists mostly of the Australia-Indian plate; with a sequence of islands running north-south along the eastern edge of the bay denoting the plate boundaries and the edge of the subduction zone. The India Plate slips deeper and deeper beneath the Burma Plate until the increasing temperature and pressure drive volatiles out of the subducting plate. These volatiles rise into the mantle above and trigger melting which exits the earth's mantle through volcanoes. The volcanic activity has created the Sunda Arc.

The direction of convergence of the India Plate relative to the overriding plate of the subduction zone (thick arrows on map below) is oriented oblique to the trench axis. For an oblique subduction zone such as this, strain can be partitioned in one of two ways as shown in the Figure 6-2 below (from Geist *et al.*, 1999; see also Michel *et al.,* 1990). The Sumatra subduction zone is characterized by decoupled fault, in which nearly pure thrust faulting occurs along the inter-plate thrust and trans-current, strike-slip faulting occurs in the overriding plate.

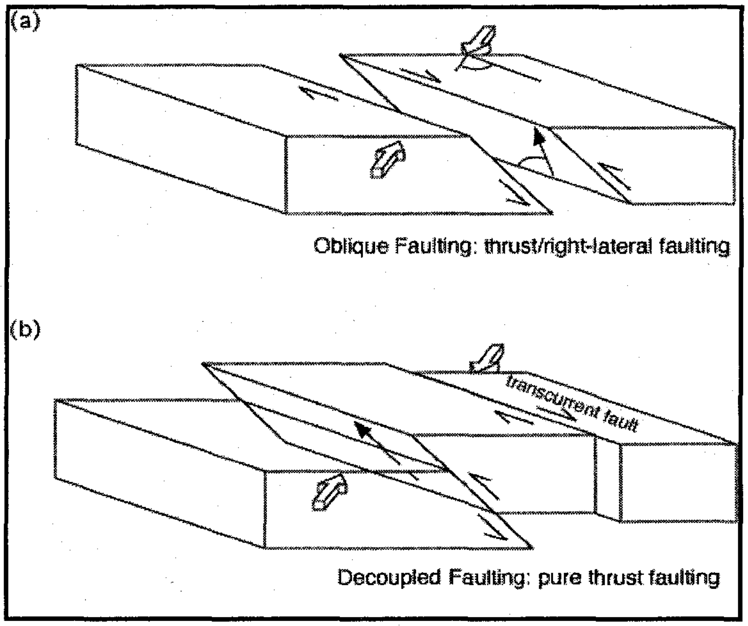

Figure 6-2: Models of fault (from Geist, 1999; see also Michel 1990)

6.4. Earthquake generation process

The December 2004 earthquake was unusually large in its geographical extent. An estimated 1200 km of fault-line slipped about 15 m along the subduction zone where the India Plate dives under the Burma Plate. The slip did not happen instantaneously, but took place in two phases over a period of several minutes, the faulting released elastic strain that had accumulated for centuries. Seismographic data indicate that the first phase involved the formation of a rupture about 400 km long and 100 km wide, located 30 km beneath the sea bed. The rupture proceeded at a speed of about 2 km/s or 7200 km/h, beginning off the coast of Aceh and proceeding north-westerly over a period of about 100 seconds. A pause of about another 100 seconds took place before the rupture continued northwards towards the Andaman and Nicobar Islands. The oblique motion is partitioned into thrust-faulting, which involved slip directed at a large angle to the orientation of the trench, and strike-slip faulting, which occurs on the eastern boundary of the Burma microplate and involves slip directed approximately parallel to the trench. Because aftershocks occur on and very near the fault planes of main shocks, the length of the aftershock zone suggests that main-shock fault-rupture may have extended north of epicenter by an amount significantly larger than 500 km. The waves did not originate from a point source, as mistakenly depicted in some illustrations, but radiated outwards along the entire 1200 km length of the rupture. This greatly increased the geographical area over which the waves were observed, reaching as far as Mexico and Chile. Currently available models of the December 26 main-shock fault displacement differ in many interesting details, but are consistent in implying that fault-rupture propagated to the northwest from the epicenter and that substantial fault-rupture occurred hundreds of kilometers northwest of the epicenter. The data upon which the modeling is based does not allow confident resolution of the extent of the rupture beyond about 500 km northwest of the main-shock epicenter.

6.5. Observational data

In response to the Indian Ocean tsunami, the international community quickly initiated and organized post-tsunami survey plans. The primary objective of the post-tsunami surveys was to collect physical evidence and eyewitness accounts on maximum tsunami heights, maximum run-up heights, inundation distances, areas of inundation, and tsunami deposits. Those data are first-hand field survey data. My supervisor, Dr. Ioan Nistor, together with several professors from the University of Ottawa and McMaster University conducted one of the surveys in Thailand (Phuket and Khao Lak) and Indonesia (Banda Aceh). Results of the field survey data can be found in several published papers.

The Sumatra event was the first major tsunami detected by satellite altimetry. Moreover, the event was observed by four satellite systems (TOPEX/POSEIDON, Jason-1, Envisat and Geosat) rather than just a single system. The Jason-satellite, jointly operated by NASA and the French space agency (CNES), was strategically placed during cycle 109, track 129 (Gower *et al.*, 2005), providing accurate measurement of the tsunami wave height in the Indian Ocean. As indicated by Figure 6-3, the tracks crossed the spreading front of the tsunami waves twice: in the north in the Bay of Bengal and in the south about 1200 km southward from Sri Lanka. In addition to augmenting the overall data coverage, the satellite data yielded snapshots of the spatial structure of the tsunami waves for the open Indian Ocean for which there are no sea level recorders. The satellite traversed this north to south tracking during the time period of 2:51 to 3:02 UTC (from latitude 12^0 S to latitude 20^0), or about 2 hours after the main earthquake shock (Kulikov *et al*, 2005).

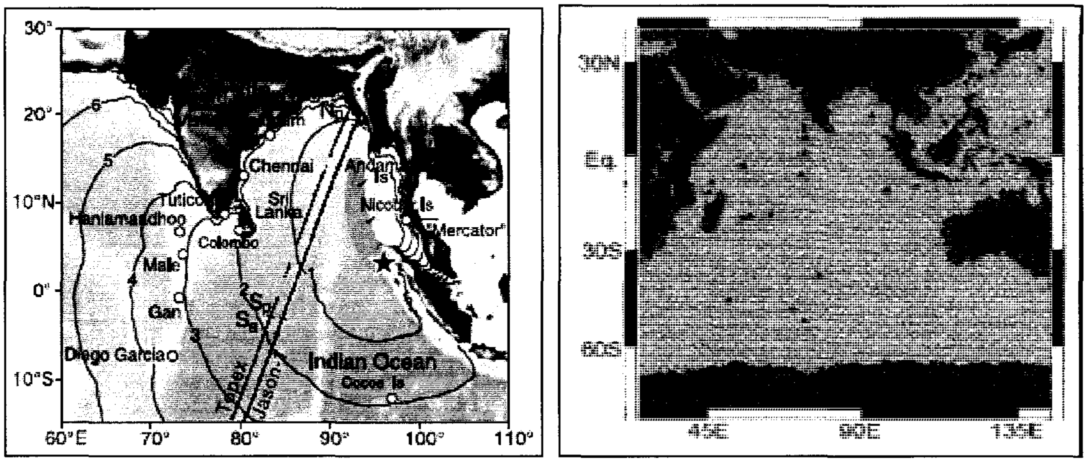

(a) (b)

Figure 6-3: (a). The blue and red lines show the tracks of the Topex/Poseidon and Jason-1 satellites that passed over the Indian Ocean about two hours after the December 26, 2004 earthquake. The red star marks the earthquake epicenter; the shaded gray area bordered by a dashed line specifies the aftershock region. The gray lines are calculated hourly isochrones of tsunami travel time. (b). picture shows location of tide gages round Indian Ocean. (FINE *et al.*, 2005)

Even though more than 50 tide gauges were located around the Indian Ocean, only a few had useful records for tsunami wave studies and 9 stations reported in real-time conditions. The following Table 6-2 lists data derived from 33 tide gauge records around the Indian Ocean. Wave arrival times obtained from a number of coastal tide gauges in the Indian Ocean were used to delineate the source region of the tsunami. The data are used to calibrate numerical models and can also be used to estimate the tsunami arrival time for tsunami early warning systems in the case of future events. The University of Hawaii Sea Level Center (supported by NOAA) maintains a network of sea-level stations in the Indian Ocean that report real-time sea-level data on Global Sea Level Observing System (GLOSS) sites http://www.gloss-sealevel.org/. Five tide gauge stations (Colombo, Hanimaadhoo, Male, Gan and Diego Garcia) have digital tsunami records which were posted on their website. http://ilikai.soest.hawaii.edu/uhslc/iotd/. Cocos Islands data are obtained from the National Tidal Centre, Australian Bureau of Meteorology. Seven tide gauge station (Paradip, Vishakapatnam, Chennai, Tuticorin, Okaha, Kochi and Mormugao) records are obtained from the National Institute of Oceanography, India (which can be found on their website http://www.nio.org/jsp/tsunami.jsp). The rest of the tide gauge records are obtained from http://www.drs.dpri.kyoto-u.ac.jp/sumatra/index-e.html and can also be found on the website http://nctr.pmel.noaa.gov/sumatra20041226.html..

Table 6-2: tsunami arrival times derived from tide gauge records

No.	COUNTRY	STATION	LONGITUDE	LATITUDE	OBSERVED(h)
1	Thailand	Ranong	98.580	9.970	3.67
2		Kuraburi	98.080	9.130	3.17
3		Ta Phao Noi	98.030	7.670	2.33
4		Krabi	99.200	8.170	3.33
5		Ta Ru Tao	100.000	6.080	3.00
6		Yacht Mercator	98.280	7.750	1.63
7	Indonesia	Pelabuhan Ratu	103.090	-9.590	2.00
8		Sibolga	98.460	1.450	1.33
9	Maldive	Hanimadhoo	73.180	6.770	3.53
10		Male	73.520	4.180	3.25
11		Gan	73.170	-0.680	3.32
12	India	Vishakhapatnam	83.280	17.650	2.60
13		Chennai	80.320	13.100	2.60
14		Tuticorin	78.200	8.750	3.47
15		Okha	69.080	22.470	8.10
16		Paradip	86.700	20.260	2.52
17		Kochi	76.200	9.580	4.64
18		Mormugao	73.800	15.420	5.92
19		Khozikode	75.430	11.150	4.73
20		Kollam	76.630	8.900	4.65
21		Thiruvananthapura	77.000	8.410	4.18
22		Kavaratti Island	72.710	10.530	4.52
23		Andrath Island	73.160	11.000	4.54
24		Chetlat Island	76.830	11.760	5.38
25		Minicoy Island	73.020	8.480	4.20
26	Sri Lanka	Colombo	79.830	6.930	2.83
27	Mauritius	Port louis	57.300	20.090	5.00
28	Oman	Salalah	54.000	16.930	7.28
29	Kenya	Lamu	40.900	-2.270	9.15
30	Tanzania	Zanzibar	39.180	-6.150	9.82
31	Australia	Cocos	96.880	-12.130	2.35
32	UK	Diego Garcia	72.380	-7.300	3.77
33	Seychelle	Pt. La Rue	55.530	-4.570	7.42

Note: The negative sign in the latitude column stands for locations in the South hemisphere.

Perhaps for the first time in the history of tsunami science, there were numerous detailed eyewitness observations of coastal tsunami impact in the form of video digital recordings (e.g., http://www.waveofdestruction.org/tsunami-videos/). These provided visual estimates of wave height and, in some cases, rough arrival times of successive tsunami waves. These observational data are essential for validating numerical models for tsunami-wave propagation over the ocean and run-up/inundation in coastal areas, for improving our understanding of the fault-plane mechanism and for understanding the tsunami interaction with the coastal area.

6.6. Earthquake mechanism and tsunami generation

Since earthquakes are generated underneath the Earth's crust, they cannot be detected by naked eye or direct view, but have to be either inversely derived from observed tsunami data or detected through the use of seismic wave data.. In the analyzed literature, a series of numerical simulations of tsunami generation and propagation were performed for the December 26, 2004, earthquake, each using different fault-plane mechanisms to test the numerical models. Results were compared with data from field surveys and available tidal-gauge records. The details of the coseismic deformation that generated these powerful waves still have substantial uncertainties. Among the earthquake generation mechanisms, the two most recognized were: one based on the fault mechanisms provided by USGS (Ji, 2005); and another based on the NOAA fault-plane parameters suggested by Stein and Okal (2005). The USGS fault-plane parameters (Table 6-3) were calculated using the Harvard University CMT solution. The estimated length of the fault plane was 500 km; the estimated width was 150 km. Because the strike angle was 320°, which denotes the angle from the North to the fault line in a clockwise direction, the fault line pointed Northwest. For the seismic moment 3.575×10^{29} dyne-cm, the rigidity of Earth's crust can be estimated as $\mu = 4.35 \times 10^{10}$ N/m^2.

Table 6-3: Fault Parameters from USGS

Fault Parameters	Fault Plane
Fault depth	10 km
Length of fault plane	500 km
Width of fault plane	150 km
(Strike, Dip, Slip)	(320°, 11°, 110°)
Dislocation	11m

Figure 6-4 shows the corresponding displacement of the submarine bottom based on USGS fault parameters. The maximum bottom displacement, thus the surface initial wave height is close to 7 meters.

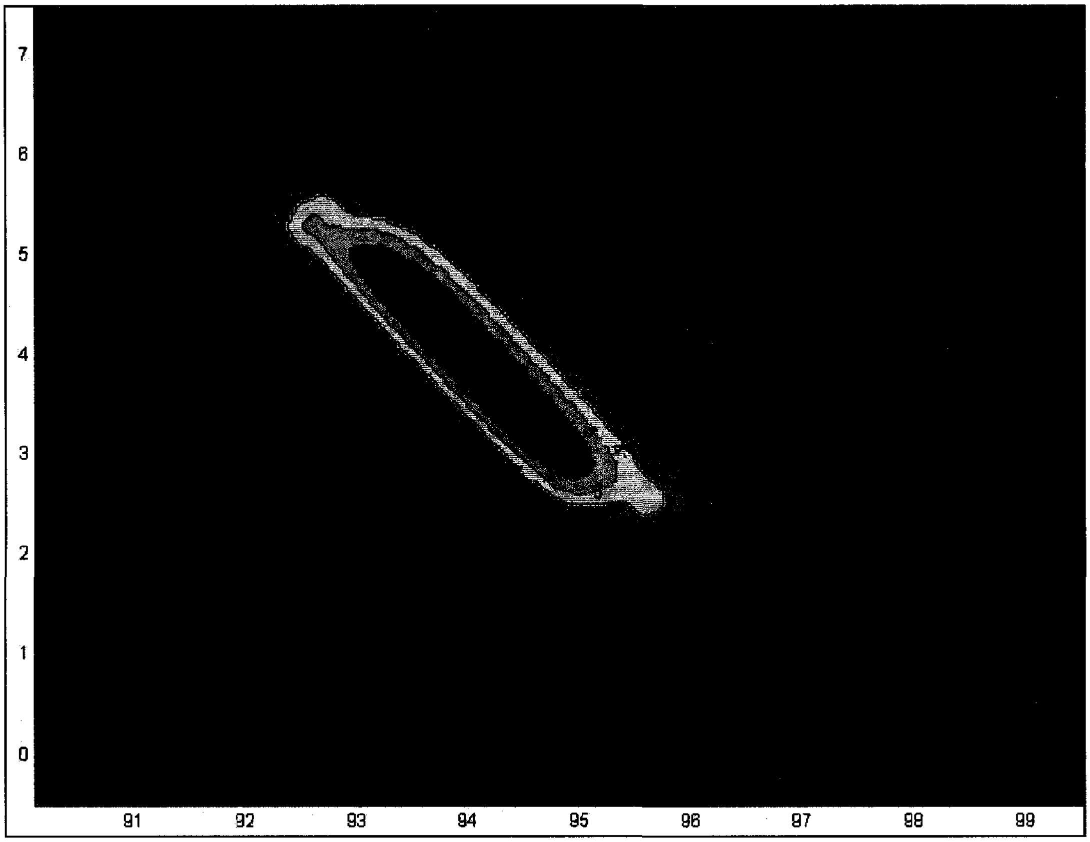

Figure 6-4: Calculated displacement of the submarine bottom by using USGS fault parameters (max. ~7m)

The NOAA fault-plane parameters (Table 6-4) suggest that the fault slip occurred over the northern part of the rupture zone. Three sub-fault planes are oriented along the northern Sunda Trench. The total length of the fault zone is 1170 km; the width of the fault plane is kept as a constant at 150 km. Using $\mu = 4.35 \times 10^{10}$ N/m^2 for rigidity of Earth's crust, the total seismic moment is estimated as 1.135×10^{30} dyne-cm, which is significantly larger than the estimate with the USGS fault-plane mechanism. The finite fault model shown here implies that the width of the earthquake rupture, measured perpendicular to the Sunda trench, was about 150 kilometers, and that the maximum displacement on the fault plane was about 15 meters. Figure 6-5 shows the corresponding displacement of the submarine bottom based on NOAA fault parameters.

Table 6-4: Source parameters from NOAA

Source Parameters	Fault Plane 1	Fault Plane 2	Fault Plane 3
Fault depth	5 km	5 km	5 km
Length of fault plane	200 km	670 km	300 km
Width of fault plane	150 km	150 km	150 km
(Strike, Dip, Slip)	(300°, 13°, 90°)	(345°, 13°, 90°)	(365°, 13°, 90°)
Dislocation	15 m	15 m	15 m

Figure 6-5: Calculated displacement of the submarine bottom by using NOAA fault parameters (max. ~10m)

From what has been described above for the generation process, it is clear that the NOAA fault plain mechanism is more reliable and closer to the reality but is still of questionable validity. Numerical simulation of the tsunami propagation shows that, although a very coarse grid size was adapted for the simulations, the results, based on the NOAA fault-plane mechanism, match the field survey data fairly well along the coastlines of Sri Lanka, India, and Indonesia. However, there are still several discrepancies in both arrival time and wave amplitude between numerical results and tide-gauge data. The discrepancies could be caused by the large grid size used and uncertainties in the fault-plane mechanism, keeping in mind also that the effects of slow rupture propagation have not been considered in the present study. According to the initial free-surface profiles calculated, the NOAA fault-plane mechanism is more energetic and would generate a much larger tsunami. Furthermore, because the NOAA fault plane stretched farther north, the generated tsunami would have much more severe impacts on the coast of Sri Lanka and the east coast of India.

6.7. Tsunami travel time

Tsunami travel time from the source region to a given location is an important parameter in tsunami prediction and for the early warning systems. The Indian Ocean tsunami arrival times have been collected for many locations. This data set represents a tremendous possibility for the comparison of observed data with the model results. Tsunami records from a number of tide gauges in the Indian Ocean are of sufficiently high quality and resolution for the accurate estimation of tsunami arrival times. The epicenter of the earthquake generated on 26th December off the Sumatra coast was at located at 92.61 E longitude and 4.61 N latitude. However there were hundreds of aftershocks in an area north of the earthquake epicenter, about 1200 km long. Figure 6-6 shows the tsunami travel time chart using the tsunami epicenter at 92.61 E longitude and 4.61 N latitude.

In water depth of 2000 m, the tsunami wave celerity is about 140m/s; a bathymetric error of 500 m will cause an uncertainty of ± 18 m/s, thus introducing a 12% uncertainty in the speed of the tsunami wave. To eliminate such known sources of error, precise bathymetries surveys including ocean bottom topographic details must be planned and conducted. Strictly speaking, the travel time is an integration over the bathymetries data; hence the deviations indicate uncertainties or lack of precise knowledge of the bathymetry. From the earthquake epicenter to Port Luis, the computation gives a travel time of about 6.85 hours, whereas the observed time was about 5.0 hours. Thus, the computed time overestimates the tsunami travel time in this case by 1.85 hours, an error of 37%, which indicates a cumulative error of bathymetry of over 1000 meters. The numerical results show the correct phase of the leading wave, but the arrival time of the leading wave has an average error of 21 minutes in the model. However, considering the low grid resolution (2 minutes) and the coarse bathymetry, the numerical results match the tide-gauge records fairly well. The tsunami hit the coasts of Thailand and Sri Lanka in 2 hours, the Maldives within 4 hours, and eastern Africa in about 10 hours. Table 6-5 lists the calculated arrival times from the MIRONE model and the observed times for 27 tide gauge locations.

Table 6-5: Model calculation time compared with observation time

No.	Country	station	Longitude	Latitude	Observed travel time	Calculated travel time	
						ETOPO2	Difference
1	Thailand	Ranong	98.58^{0}E	9.97^{0}N	3h40min	3h30min	+10min
2		Kuraburi	98.08^{0}E	9.13^{0}N	3h10min	3h	+10min
3		Ta Phao Noi	98.03^{0}E	7.67^{0}N	2h20min	1h48min	+32min
4		Krabi	99.2^{0}E	8.17^{0}N	3h20min	3h	+20min
5		Kantrang	99.87^{0}E	8.67^{0}N	4h50min	5h	-10min
6		Ta Ru Tao	100.0^{0}E	6.08^{0}N	3h	3h36min	-36min
7		Yacht Mercator	98.28^{0}E	7.75^{0}N	1h38min	2h12min	-34min
8	Indonesia	Pelabuhan Ratu	103.09^0 E	9.59^0 S	2h	2h14min	-14min
9		Sibolga	98.46^{0}E	1.45^{0}N	1h20min	1h42min	-22min
10	Maldives	Hanimadhoo	73.18^{0}E	6.77^{0}N	3h32min	4h	-28min
11		Male	73.52^{0}E	4.18^{0}N	3h15min	3h6min	+9min
12		Gan	73.17^{0}E	0.68^{0}S	3h19min	3h42min	-23min
13	India	Vishakhapatnam	83.28^{0}E	17.65^{0}N	2h36min	3h12min	-36min
14		Chennai	80.32^{0}E	13.10^{0}N	2h36min	2h48min	-12min
15		Tuticorin	78.20^{0}E	8.75^{0}N	3h28min	3h36min	-8min
16		Okha	69.08^{0}E	22.47^{0}N	8h06min	8h18min	-12min
17		Paradip	86.7^{0}E	20.26^{0}N	2h31min	2h42min	-11min
18		Kochi	76.26^{0}E	9.96^{0}N	4h40min	4h54min	-14min
19		Mormugao	73.80^{0}E	15.42^{0}N	5h55min	5h54min	+1min
20	Sri Lank	Colombo	79.83^{0}E	6.93^{0}N	2h50min	3h	-10min
21	Mauritius	Port louis	57.30^{0}E	20.09^0 S	5h	6h51min	-1h51min
22	Oman	Salalah	54.0° E	16.93° N	7h17min	6h48min	+29min
23	Kenya	Lamu	40.90^0 E	2.27° S	9h9min	8h30min	+39min
24	Tanzania	Zanzibar	39.18° E	6.15°S	9h49min	8h42min	+67min
25	Australia	Cocos	96.88^{0}E	12.13^{0}S	2h21min	2h26min	-5min
26	UK	Diego Garcia	72.38^{0}E	7.30^{0}S	3h46min	4h1min	-15min
27	Seychelles	Pt. La Rue	55.53^{0}E	4.57^{0}S	7h25min	7h14min	+11min
Absolute average difference							21min

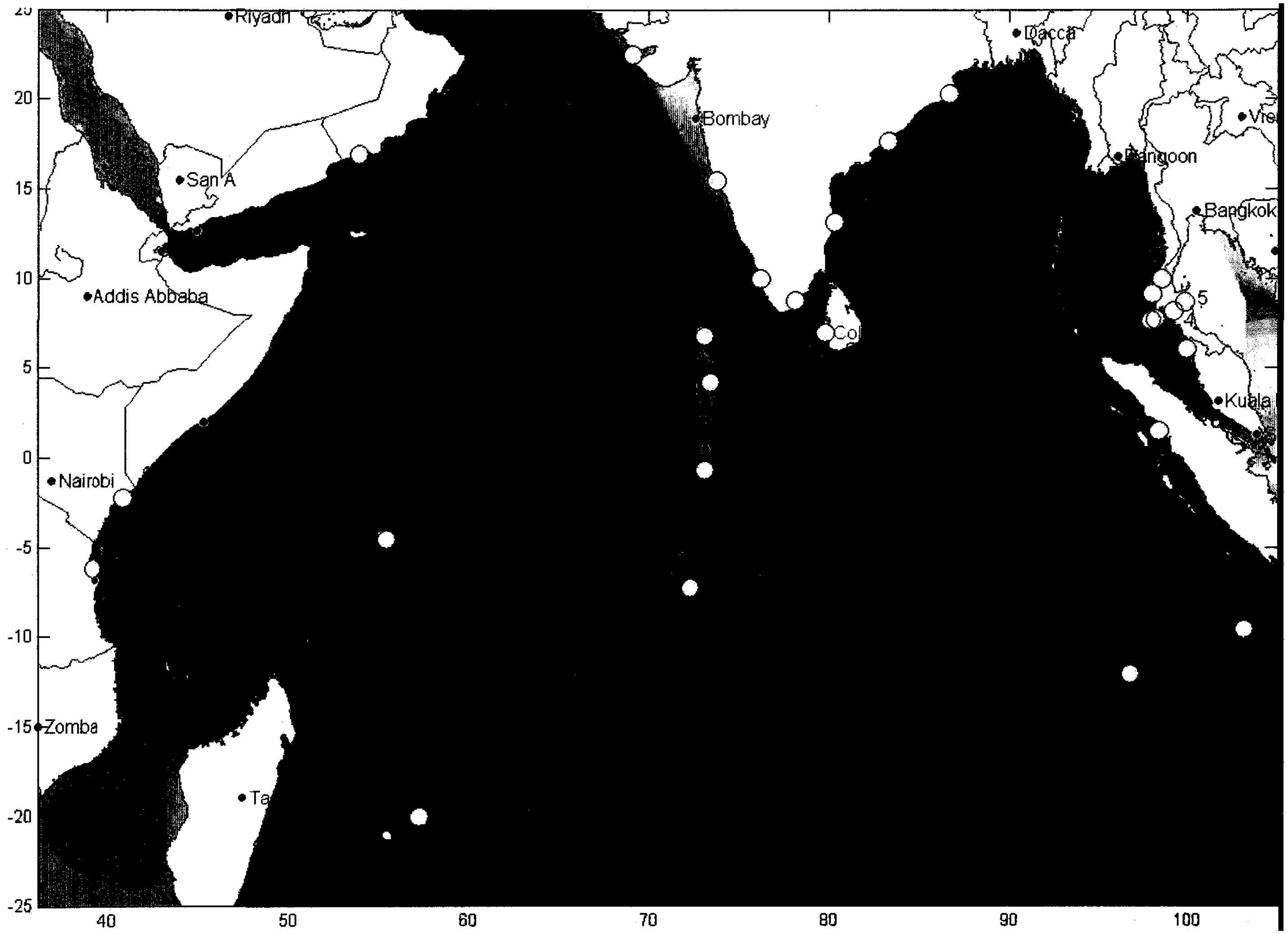

Figure 6-6: Computed tsunami travel time for the 2004 Indian Ocean tsunami using the 2 minutes of arc bathymetry

6.8. Tsunami propagation

The simulated domain covers almost the entire Indian Ocean, ranging from 36°E to 105°E longitude and –25°S to 25°N latitude, with a grid size of 2 minutes of arc (ETOPO2). The dimension of the grid is 2,071 in the E-W direction by 1,501 in the N-S direction. The simulations were done on a desktop computer (2.0GB RAM and Athlon XP 2600+ CPU) and took 2 hours. Numerical stability requires that the time step should be smaller than $D/\sqrt{gh}$ (D is grid size). Taking the average depth of Indian Ocean as 4000m, the time step for numerical integration is therefore less than 9.26 seconds. This step was diminished to an even smaller value when tsunami wave propagates onto the shoreline, as the run-up scheme requires smaller time stepping. A smaller spatial step is important as the short-period waves can be obliterated during large distance of propagation when using large spatial steps. A tsunami wave with a 10 minute period in an average water depth of 4000m has a wavelength close to 120km. Such a wave length is discretized by the 2 minutes grid into about 32 mesh lengths. In the present study, the time step was 6 seconds and the total simulation time lasts about 9 hours until the tsunami wave reached Africa.

It was shown that with the MIRONE model, the observed features of the tsunami such as the initial drying of areas to the east of the source region, the initial flooding of western coasts and the formation of a series of waves are correctly simulated. During this computation, the maximum tsunami amplitude in every grid point was recorded. The plot of surface profile in the proximity of the generation domain is given in Figure 6-7. The maximum surface wave height approximates to 16.5 meters. As the 2004 Indian Ocean tsunami carried a wide spectrum of waves with periods from 10 to 60 min, the wavelength for the mid-ocean travel is in the range of 100 km to 600 km. A simple qualitative model for the long wave trapping may be based on different speed of the tsunami wave over and off the ridges. As the wave over ridges is slower and the wave off the ridges is faster, the joint tsunami wave front is curved in such a way that the energy is fluxed towards the ridge.

The strong directional signal in the tsunami generated by the elongated source dominates the Indian Ocean domain. The main energy lobe is directed towards South Africa and the secondary lobe points towards Sri Lanka, sending a noticeable signal into the Atlantic Ocean. Figure 6-8 demonstrate strong directionality of the tsunami wave propagation.

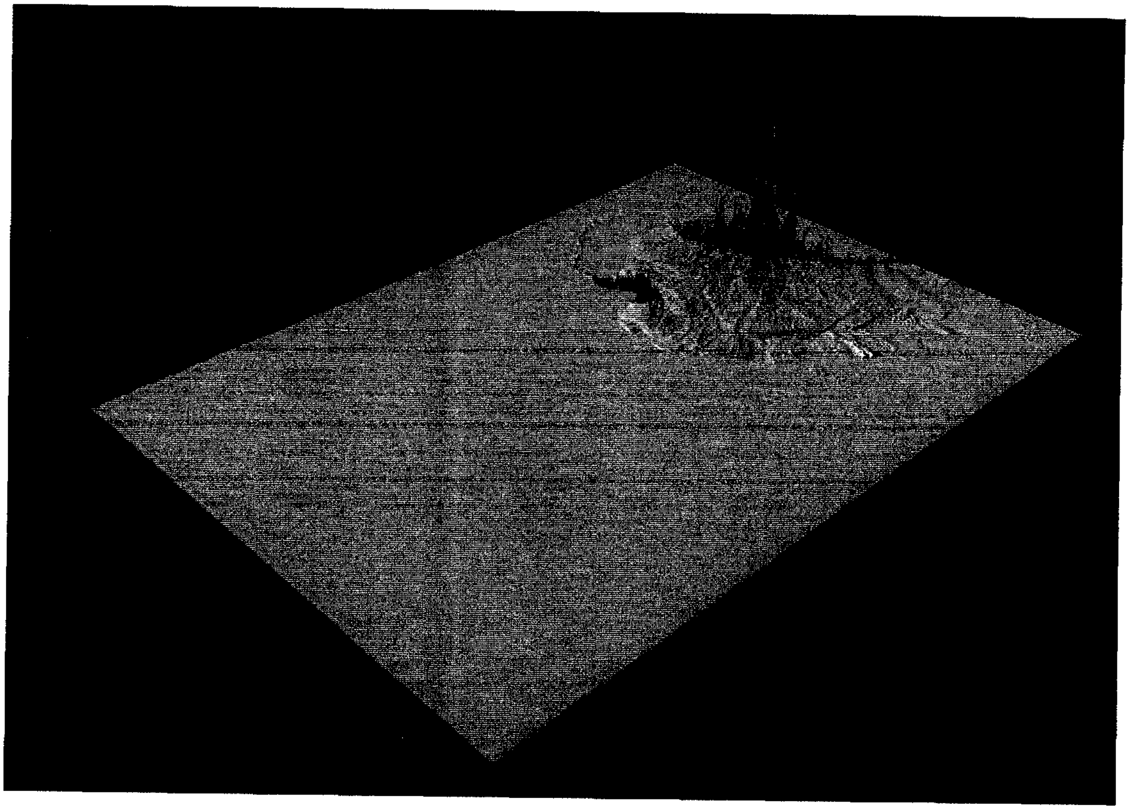

Figure 6-7: surface profile in the proximity of the generation domain at the time of 3 hours after earthquake.

The maximum amplitude is 24.5 m in the proximity of the fault, 9.3 m at the shore of Thailand, 8.1 m in Sri Lanka and up to 5 m in South Africa. This figure also depicts the amplitude enhancement in the shallow water and especially in the proximity of peninsulas and islands due to energy concentration through the refraction process. A large domain of the Arabian Sea is located in the shadow of the main energy beam. Both computation and observations demonstrate an increase of the tsunami amplitude up to 1.5 m at the coast of Oman at the tide gauge in Salalah. A simple explanation of the energy trapping using the continuity equation leads one to conclude that the amplitude should increase over the ridge due to shallower depth. At the same time, the role of the bottom friction appears to be negligible and therefore the tsunami can travel long distances without significant energy losses. The calculated maximum tsunami wave amplitudes along shorelines of Sri Lanka, India, and Aceh, Indonesia, based on the NOAA fault-plane mechanism, are shown in Figures 6-9.

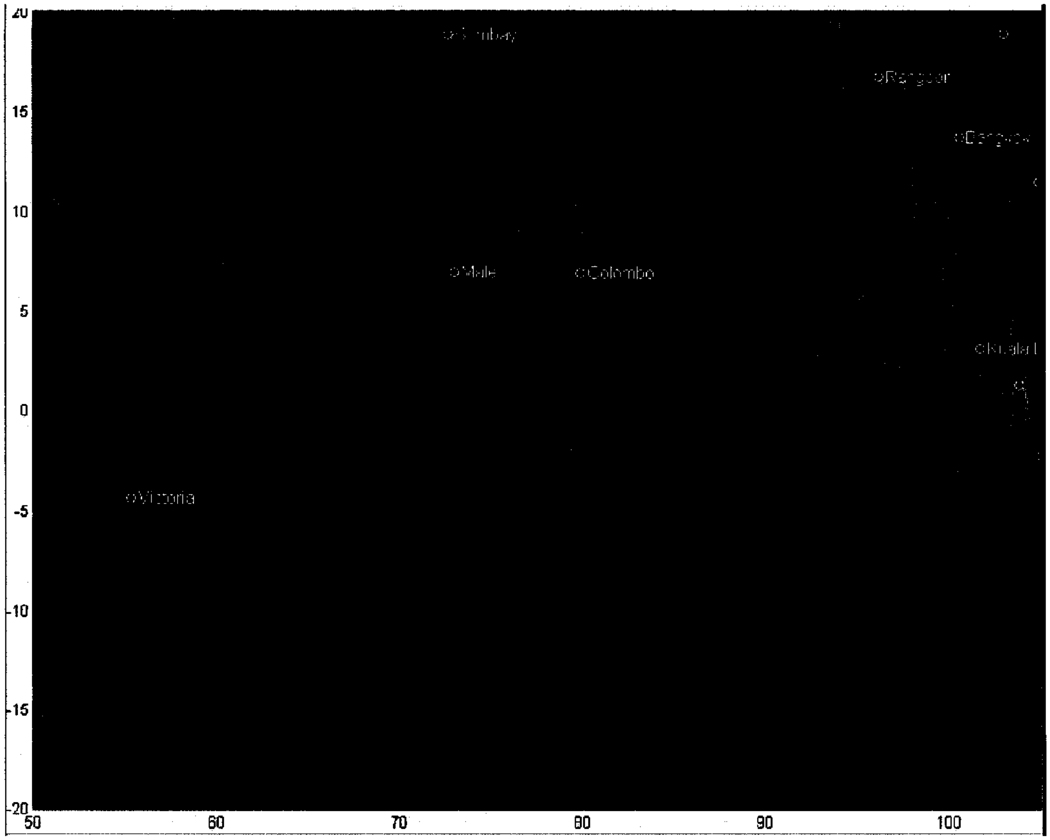

Figure 6-8: Strong directionality of tsunami wave propagation

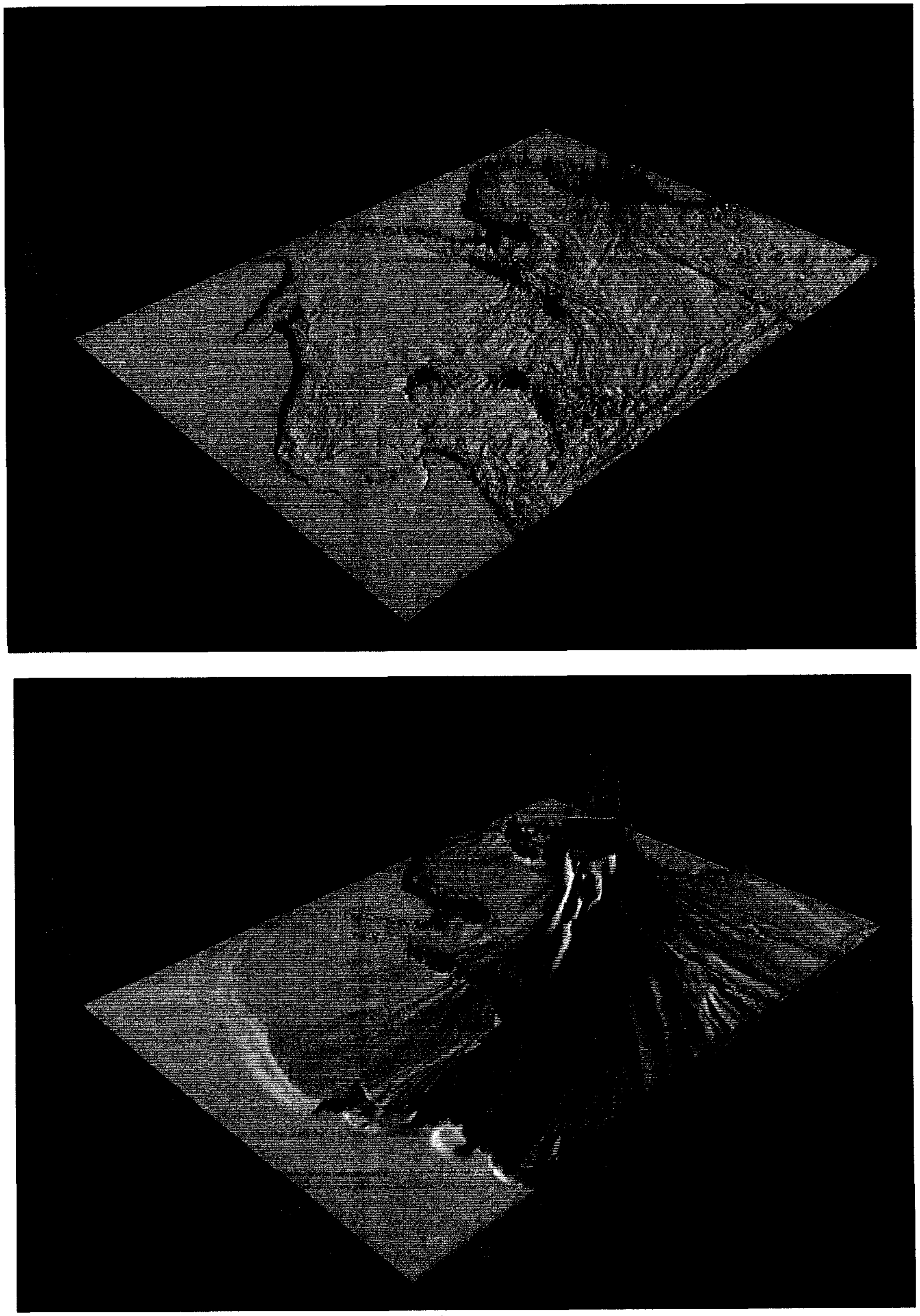

Figures 6-9: The calculated tsunami wave amplitudes and directionality in the Indian Ocean

Finally, evaluating the impact of the tsunami in the affected coastal regions will require higher resolution bathymetry/topographic data. Nonlinear effects, including non-hydrostatic and wave breaking, must also be studied and included in the simulation model. The overall agreement between the observational data and the numerical model results is reasonable, considering that the present model does not resolve the nearshore bathymetry and topography. The numerical results based on the USGS fault-plane mechanism (not presented here) significantly underestimated the wave heights everywhere. Other figures demonstrate the processes of tsunami propagation as shown in the appendix. Figure A-6 shows the ocean surface elevation and maximum wave amplitude of the 2004 Indian Ocean tsunami at different time step (t=0s, 1500s, 3000s, 6000s, 9000s, 12000s, and 15000s) after the earthquake occurrence.

The evolution of earthquake-generated tsunami waves has three distinctive stages: generation, propagation, and run-up. The MIRONE numerical model used here simulates the first two stages, providing a complete tsunami modeling capability with considerable accuracy. Due to lack of near shore bathymetry, the wave inundation and run-up are not considered here. Numerical experiments have provided plausible and useful descriptions of the tsunami propagation. The results also showed that there is significant need for further improvement, and, particularly in preparing the model grids, which may be addressed in future work.

6.9. Sensitivity test

Due to lack of instruments for measuring the wave and current in deep ocean or even in shallow waters, the only numerical output that can be compared with observations are tsunami travel times and wave heights. In this thesis, tsunami wave height and travel time are the two output parameters of numerical modeling which will be used to conduct sensitivity tests below.

Contrary to popular belief, tsunami travel times do not depend upon the magnitude of the under-ocean earthquake that generated the tsunami. Tsunami travel time is governed by the long gravity wave formula, which defines the speed of travel of the tsunami and is equal to the square root of water depth, multiplied by the acceleration due to gravity (Murty *et al.*, 1987). Once the earthquake epicenter is decided, the tsunami travel times only depend on the water depth. Of course there are higher order correction terms to the speed of tsunami travel, based upon dispersion characteristics. While these higher order terms are of scientific interest, nevertheless, for practical purposes, one can ignore the contributions from these terms, and use the simple long wave formula. For the Pacific Ocean, it has been clearly demonstrated that the computed tsunami travel times using the zero-order approximation are correct to plus or minus one minute for each hour of travel. This level of error is considered acceptable for tsunami early warning purposes. Therefore, spatial grid size is a dominant factor for the tsunami travel times. To understand how oceanic bathymetry affects tsunami wave propagation and to determine how smoothing the bathymetry affects the simulated tsunamis, the sensitivity tests of tsunami travel time is done using different available bathymetry grids, say 1 min, 2 min, 5 min, 10 min, 15 min, 20 min and 30 min of arc respectively.

The travel time obtained from the ETOPO2 is closer to the observed data. As we know, ETOPO1 was derived from ETOPO2 by using interpolation methods and it was expected to be closer to the reality than ETOPO2. But the results show that using this bathymetry was worse than using ETOPO2. A further study to trace the source data and deduce how the world oceanic bathymetry data sets are derived is important and will be addressed in a future study.

Table 6-6: tsunami travel time analysis from MIRONE model results using different grid size

No.	COUNTRY	STATION	LONGITUDE	LATITUDE	DEPTH1M	DEPTH2M	DEPTH10M	OBSERVED	CALCULATED1	RMS	CALCULATED2
7	Indonesia	Sibolga	98.460	1.450	-57.0	-24.0	-135.0	1.33	1.752	0.178	1.629
5	Thailand	Yacht Mercator	98.280	7.750	-18.0	-71.0	-79.0	1.63	2.242	0.375	2.043
6	Indonesia	Pelabuhan Ratu	103.090	-9.590	-5500.0	-5500.0	-5476.0	2.00	2.433	0.187	2.429
3	Thailand	Ta Phao Noi	98.030	7.670	-100.0	-135.0	-347.0	2.33	1.851	0.229	1.780
29	Australia	Cocos	96.880	-12.130	-27.0	-697.0	-3705.0	2.35	2.593	0.059	2.534
15	India	Paradip	86.700	20.260	-1.0	-1.0	-2.0	2.52	3.759	1.535	3.536
11	India	Vishakhapatnam	83.280	17.650	202.0	-2.0	17.0	2.60	3.251	0.424	3.304
12	India	Chennai	80.320	13.100	1.0	8.0	18.0	2.60	2.885	0.081	2.850
24	Sri Lanka	Colombo	79.830	6.930	-14.0	-35.0	-175.0	2.83	2.997	0.028	2.515
4	Thailand	Ta Ru Tao	100.000	6.080	-6.0	-5.0	-39.0	3.00	4.186	1.407	4.010
2	Thailand	Kuraburi	98.080	9.130	-30.0	-27.0	-15.0	3.17	2.927	0.059	2.917
9	Maldive	Male	73.520	4.180	16.0	-48.0	-338.0	3.25	3.141	0.012	3.169
10	Maldive	Gan	73.170	-0.680	-6.0	1.0	-2467.0	3.32	3.234	0.007	3.230
13	India	Tuticorin	78.200	8.750	-1.0	-1.0	16.0	3.47	3.646	0.031	3.079
8	Maldive	Hanimadhoo	73.180	6.770	46.0	-3.0	-11.0	3.53	3.311	0.048	3.427
1	Thailand	Ranong	98.580	9.970	-3.0	-1.0	-10.0	3.67	4.506	0.699	4.011
30	UK	Diego Garcia	72.380	-7.300	-39.0	-1057.0	-1178.0	3.77	3.631	0.019	3.610
20	India	Thiruvananthapura	77.000	8.410	6.0	-7.0	-56.0	4.18	4.000	0.032	3.667
23	India	Minicoy Island	73.020	8.480	-2117.0	-2181.0	-2135.0	4.20	3.483	0.514	3.505
21	India	Kavaratti Island	72.710	10.530	-1116.0	-1033.0	-2152.0	4.52	3.811	0.503	3.819
22	India	Andrath Island	73.160	11.000	-2004.0	-1922.0	-1900.0	4.54	3.808	0.536	3.876
16	India	Kochi	76.200	9.580	-14.0	-29.0	-87.0	4.64	6.139	2.247	4.277
19	India	Kollam	76.630	8.900	4.0	-1.0	-15.0	4.65	4.200	0.203	4.015
18	India	Khozikode	75.430	11.150	-63.0	-6.0	-191.0	4.73	8.265	12.496	5.866
25	Mauritius	Port louis	57.300	20.090	157.0	139.0	151.0	5.00	6.846	3.408	6.846
17	India	Mormugao	73.800	15.420	-1.0	-41.0	-47.0	5.92	6.000	0.006	5.520
26	Oman	Salalah	54.000	16.930	24.0	-2.0	-97.0	7.28	7.000	0.078	6.896
31	Seychelle	Pt. La Rue	55.530	-4.570	-18.0	-1.0	-51.0	7.42	7.105	0.099	6.950
14	India	Okha	69.080	22.470	1.0	-1.0	-16.0	8.10	8.000	0.010	7.580
27	Kenya	Lamu	40.900	-2.270	1.0	-1.0	-36.0	9.15	9.000	0.023	8.762
28	Tanzania	Zanzibar	39.180	-6.150	-1.0	-1.0	-1.0	9.82	10.724	0.817	9.498
RMS										0.922	

Table 6-7: tsunami travel time analysis from MIRONE model results using different grid size (continued)

STATION	LONGITUDE	LATITUDE	OBSERVED	RMS	ERROR	CALCULATED1	RMS	ERROR	CALCULATED2	RMS	ERROR
Sibolga	98.460	1.450	1.33	0.42		1.752	0.30		1.629	0.13	
Yacht Mercator	98.280	7.750	1.63	0.61		2.242	0.41		2.043	0.26	
Pelabuhan Ratu	103.090	-9.590	2.00	0.43		2.433	0.43		2.429	0.42	
Ta Phao Noi	98.030	7.670	2.33		-0.48	1.851		-0.55	1.780		-0.68
Cocos	96.880	-12.130	2.35	0.24		2.593	0.18		2.534	0.15	
Paradip	86.700	20.260	2.52	1.24		3.759	1.02		3.536	0.77	
Vishakhapatnam	83.280	17.650	2.60	0.65		3.251	0.70		3.304	0.62	
Chennai	80.320	13.100	2.60	0.29		2.885	0.25		2.850	0.08	
Colombo	79.830	6.930	2.83	0.17		2.997		-0.32	2.515		-0.53
Ta Ru Tao	100.000	6.080	3.00	1.19		4.186	1.01		4.010	0.64	
Kuraburi	98.080	9.130	3.17		-0.24	2.927		-0.25	2.917		-0.88
Male	73.520	4.180	3.25		-0.11	3.141		-0.08	3.169		-0.08
Gan	73.170	-0.680	3.32		-0.09	3.234		-0.09	3.230		-0.09
Tuticorin	78.200	8.750	3.47	0.18		3.646		-0.39	3.079		-0.59
Hanimadhoo	73.180	6.770	3.53		-0.22	3.311		-0.10	3.427		-0.09
Ranong	98.580	9.970	3.67	0.84		4.506	0.34		4.011	0.22	
Diego Garcia	72.380	-7.300	3.77		-0.14	3.631		-0.16	3.610		-0.18
Thiruvananthapura	77.000	8.410	4.18		-0.18	4.000		-0.51	3.667		-1.07
Minicoy Island	73.020	8.480	4.20		-0.72	3.483		-0.70	3.505		-0.70
Kavaratti Island	72.710	10.530	4.52		-0.71	3.811		-0.70	3.819		-0.71
Andrath Island	73.160	11.000	4.54		-0.73	3.808		-0.66	3.876		-0.70
Kochi	76.200	9.580	4.64	1.50		6.139		-0.36	4.277		-1.06
Kollam	76.630	8.900	4.65		-0.45	4.200		-0.64	4.015		-1.32
Khozikode	75.430	11.150	4.73	3.54		8.265	1.14		5.866		-0.96
Port louis	57.300	20.090	5.00	1.85		6.846	1.85		6.846	1.85	
Mormugao	73.800	15.420	5.92	0.08		6.000		-0.40	5.520		-0.62
Salalah	54.000	16.930	7.28		-0.28	7.000		-0.38	6.896		-0.49
Pt. La Rue	55.530	-4.570	7.42		-0.32	7.105		-0.47	6.950		-0.81
Okha	69.080	22.470	8.10		-0.10	8.000		-0.52	7.580		-0.53
Lamu	40.900	-2.270	9.15		-0.15	9.000		-0.39	8.762		-0.73
Zanzibar	39.180	-6.150	9.82	0.90		10.724		-0.32	9.498		-0.67
				14.11	-4.91		7.628	-7.998		5.123	-13.479
AVERAGE				0.88	0.29		0.693	0.400		0.512	0.642

Figure 6-10: comparison of tsunami travel time using Mirone model with different grid size

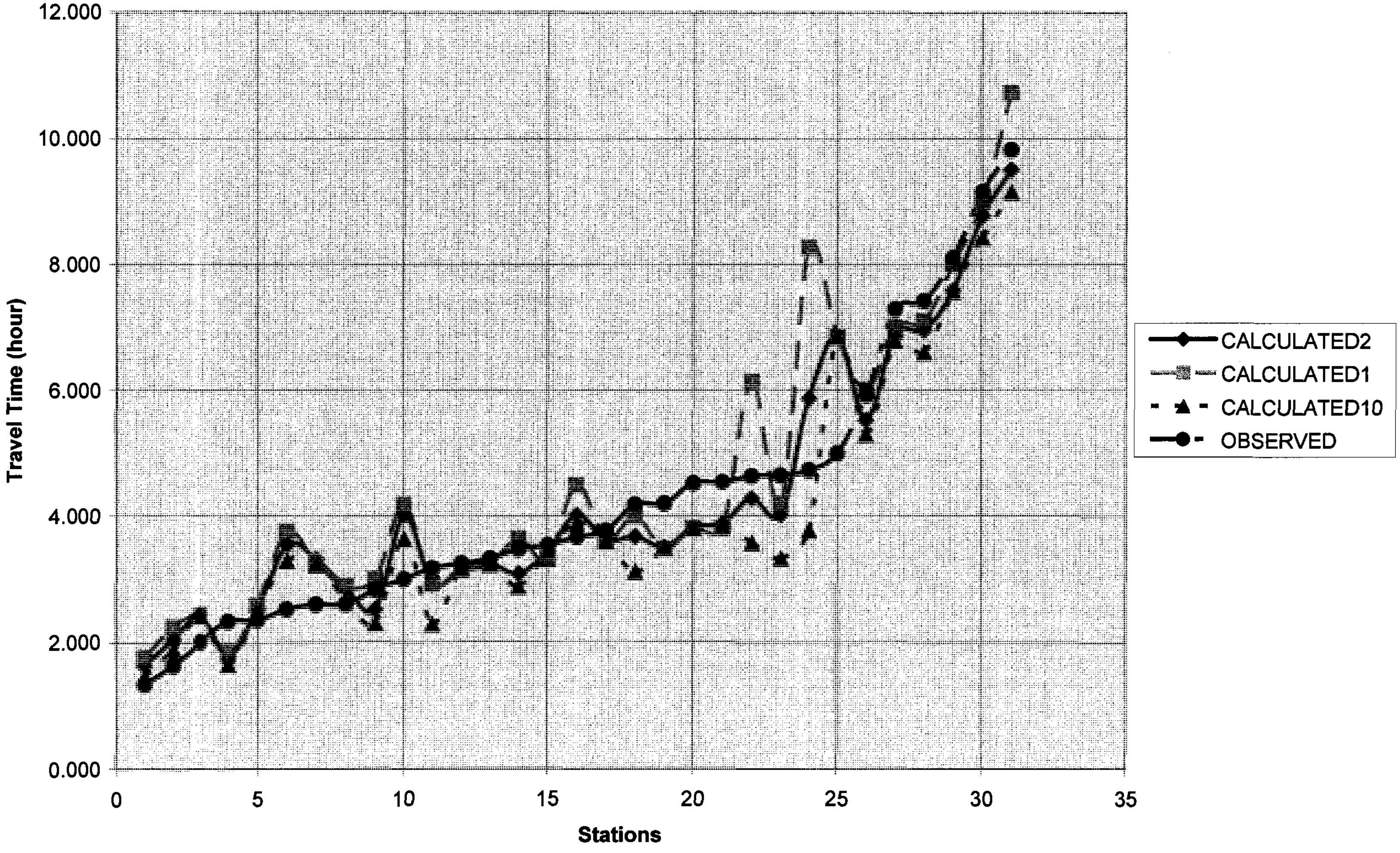

Table 6-8: tsunami travel time analysis from GEOWARE model results using different grid size

			ETOPO2			ETOPO5			ETOPO10
	STATION	OBSERVED	CALCULATED2	DIFFERENCE	ABSOLUTE	CALCULATED5	DIFFERENCE	ABSOLUTE	CALCULATED10
1	Sibolga	1.33	1.62009	-0.29009	0.29009	1.62578	-0.29578	0.29578	1.66161
2	Yacht Mercator	1.63	2.09540	-0.46540	0.46540	2.05252	-0.42252	0.42252	2.11913
3	Pelabuhan Ratu	2.00	2.39391	-0.39391	0.39391	2.40307	-0.40307	0.40307	2.4124
4	Ta Phao Noi	2.33	1.78166	0.54834	0.54834	1.78935	0.54065	0.54065	1.78947
5	Cocos	2.35	2.50097	-0.15097	0.15097	2.49481	-0.14481	0.14481	2.49552
6	Paradip	2.52	3.56991	-1.04991	1.04991	3.49608	-0.97608	0.97608	3.32788
7	Vishakhapatnam	2.60	3.03895	-0.43895	0.43895	3.06615	-0.46615	0.46615	3.08558
8	Chennai	2.60	2.75046	-0.15046	0.15046	2.70699	-0.10699	0.10699	2.7292
9	Colombo	2.83	2.49536	0.33464	0.33464	2.48595	0.34405	0.34405	2.47555
10	Ta Ru Tao	3.00	3.81410	-0.81410	0.81410	3.85958	-0.85958	0.85958	3.91158
11	Kuraburi	3.17	2.67042	0.49958	0.49958	2.68201	0.48799	0.48799	2.67912
12	Male	3.25	3.08772	0.16228	0.16228	3.10776	0.14224	0.14224	3.13777
13	Gan	3.32	3.14405	0.17595	0.17595	3.14380	0.17620	0.17620	3.15146
14	Krabi	3.33	4.03176	-0.70176	0.70176	4.08005	-0.75005	0.75005	3.31123
15	Tuticorin	3.47	2.89823	0.57177	0.57177	2.86214	0.60786	0.60786	2.91682
16	Hanimadhoo	3.53	3.27891	0.25109	0.25109	3.29098	0.23902	0.23902	3.30675
17	Ranong	3.67	3.80916	-0.13916	0.13916	3.97791	-0.30791	0.30791	3.63125
18	Diego Garcia	3.77	3.58712	0.18288	0.18288	3.55254	0.21746	0.21746	3.55312
19	Thiruvananthapura	4.18	3.41059	0.76941	0.76941	3.33648	0.84352	0.84352	3.35869
20	Minicoy Island	4.20	3.43522	0.76478	0.76478	3.44495	0.75505	0.75505	3.45877
21	Kavaratti Island	4.52	3.75444	0.76556	0.76556	3.76323	0.75677	0.75677	3.77945
22	Andrath Island	4.54	3.77780	0.76220	0.76220	3.78541	0.75459	0.75459	3.79897
23	Kochi	4.64	3.87483	0.76517	0.76517	3.90412	0.73588	0.73588	3.83164
24	Kollam	4.65	3.87688	0.77312	0.77312	3.51856	1.13144	1.13144	3.44778
25	Khozikode	4.73	3.96322	0.76678	0.76678	3.96536	0.76464	0.76464	3.99844
26	Port louis	5.00	6.96274	-1.96274	1.96274	7.04045	-2.04045	2.04045	7.07265
27	Chetlat Island	5.38	4.61518	0.76482	0.76482	4.38120	0.99880	0.99880	4.37065
28	Mormugao	5.92	5.72262	0.19738	0.19738	5.78452	0.13548	0.13548	5.68654
29	Salalah	7.28	6.74624	0.53376	0.53376	6.76484	0.51516	0.51516	6.73459
30	Pt. La Rue	7.42	6.72289	0.69711	0.69711	6.80870	0.61130	0.61130	6.73947
31	Okha	8.10	7.27520	0.82480	0.82480	7.74988	0.35012	0.35012	7.60278
32	Lamu	9.15	8.59115	0.55885	0.55885	8.37216	0.77784	0.77784	8.53259
33	Zanzibar	9.82	9.11110	0.70890	0.70890	9.15847	0.66153	0.66153	8.99027
	AVERAGE				0.57384			0.58548	

Table 6-9: tsunami travel time analysis from GEOWARE model results using different grid size (continued)

			ETOPO15			ETOPO20			ETOPO30
	STATION	OBSERVED	CALCULATED15	DIFFERENCE	ABSOLUTE	CALCULATED20	DIFFERENCE	ABSOLUTE	CALCULATED30
1	Sibolga	1.33	1.63946	-0.30946	0.30946	1.70902	-0.37902	0.37902	1.63309
2	Yacht Mercator	1.63	2.13607	-0.50607	0.50607	2.15624	-0.52624	0.52624	2.21656
3	Pelabuhan Ratu	2.00	2.41312	-0.41312	0.41312	2.42736	-0.42736	0.42736	2.44595
4	Ta Phao Noi	2.33	1.84113	0.48887	0.48887	1.83532	0.49468	0.49468	1.88764
5	Cocos	2.35	2.46863	-0.11863	0.11863	2.47791	-0.12791	0.12791	2.45668
6	Paradip	2.52	3.36591	-0.84591	0.84591	3.12221	-0.60221	0.60221	3.20492
7	Vishakhapatnam	2.60	2.8813	-0.28130	0.28130	3.00731	-0.40731	0.40731	2.8244
8	Chennai	2.60	2.49688	0.10312	0.10312	2.63094	-0.03094	0.03094	2.50604
9	Colombo	2.83	2.40612	0.42388	0.42388	2.38836	0.44164	0.44164	2.30537
10	Ta Ru Tao	3.00	3.93323	-0.93323	0.93323	3.90492	-0.90492	0.90492	3.97014
11	Kuraburi	3.17	2.72661	0.44339	0.44339	2.69938	0.47062	0.47062	2.52936
12	Male	3.25	3.125	0.12500	0.12500	3.14328	0.10672	0.10672	3.1465
13	Gan	3.32	3.11747	0.20253	0.20253	3.14487	0.17513	0.17513	3.11016
14	Krabi	3.33	3.18216	0.14784	0.14784	3.00397	0.32603	0.32603	2.88185
15	Tuticorin	3.47	2.87103	0.59897	0.59897	2.84355	0.62645	0.62645	2.95096
16	Hanimadhoo	3.53	3.2855	0.24450	0.24450	3.30849	0.22151	0.22151	3.28158
17	Ranong	3.67	3.67538	-0.00538	0.00538	3.30235	0.36765	0.36765	3.5849
18	Diego Garcia	3.77	3.51739	0.25261	0.25261	3.54863	0.22137	0.22137	3.51628
19	Thiruvananthapura	4.18	3.30568	0.87432	0.87432	3.38589	0.79411	0.79411	3.19687
20	Minicoy Island	4.20	3.43524	0.76476	0.76476	3.46033	0.73967	0.73967	3.44776
21	Kavaratti Island	4.52	3.76065	0.75935	0.75935	3.7878	0.73220	0.73220	3.78163
22	Andrath Island	4.54	3.77819	0.76181	0.76181	3.80384	0.73616	0.73616	3.79816
23	Kochi	4.64	3.93607	0.70393	0.70393	3.73478	0.90522	0.90522	3.6962
24	Kollam	4.65	3.58823	1.06177	1.06177	3.37507	1.27493	1.27493	3.61737
25	Khozikode	4.73	3.99055	0.73945	0.73945	4.03114	0.69886	0.69886	4.04278
26	Port louis	5.00	6.91805	-1.91805	1.91805	6.83645	-1.83645	1.83645	6.79149
27	Chetlat Island	5.38	4.349	1.03100	1.03100	4.37454	1.00546	1.00546	4.25519
28	Mormugao	5.92	5.60022	0.31978	0.31978	5.42925	0.49075	0.49075	5.34654
29	Salalah	7.28	6.67214	0.60786	0.60786	6.68463	0.59537	0.59537	6.64577
30	Pt. La Rue	7.42	6.67365	0.74635	0.74635	6.62175	0.79825	0.79825	6.55547
31	Okha	8.10	7.53533	0.56467	0.56467	7.66162	0.43838	0.43838	7.36103
32	Lamu	9.15	8.23088	0.91912	0.91912	8.24254	0.90746	0.90746	8.16372
33	Zanzibar	9.82	9.14432	0.67568	0.67568	8.89757	0.92243	0.92243	8.79543
	AVERAGE				0.57248			0.59798	

Table 6-10: Comparison and analysis of results derived from GEOWARE model and MIRONE model

STATION	LONGITUDE	LATITUDE	OBSERVED	G-EXPECTED2	RMS	G-EXPECTED10	RMS	M-EXPECTED2	RMS	M-EXPECTED10	RMS
Sibolga	98.460	1.450	1.33	1.62009	0.08415	1.66161	0.10997	1.629	0.08940	1.457	0.01613
Yacht Mercator	98.280	7.750	1.63	2.09540	0.21660	2.11913	0.23925	2.043	0.17057	1.886	0.06554
Pelabuhan Ratu	103.090	-9.590	2.00	2.39391	0.15517	2.4124	0.17007	2.429	0.18404	2.416	0.17306
Ta Phao Noi	98.030	7.670	2.33	1.78166	0.30068	1.78947	0.29217	1.780	0.30250	1.654	0.45698
Cocos	96.880	-12.130	2.35	2.50097	0.02279	2.49552	0.02118	2.534	0.03386	2.502	0.02310
Paradip	86.700	20.260	2.52	3.56991	1.10231	3.32788	0.65267	3.536	1.03226	3.287	0.58829
Vishakhapatnam	83.280	17.650	2.60	3.03895	0.19268	3.08558	0.23579	3.304	0.49562	3.220	0.38440
Chennai	80.320	13.100	2.60	2.75046	0.02264	2.7292	0.01669	2.850	0.06250	2.680	0.00640
Colombo	79.830	6.930	2.83	2.49536	0.11198	2.47555	0.12563	2.515	0.09923	2.298	0.28302
Ta Ru Tao	100.000	6.080	3.00	3.81410	0.66276	3.91158	0.83098	4.010	1.02010	3.640	0.40960
Kuraburi	98.080	9.130	3.17	2.67042	0.24958	2.67912	0.24096	2.917	0.06401	2.292	0.77088
Male	73.520	4.180	3.25	3.08772	0.02633	3.13777	0.01260	3.169	0.00656	3.175	0.00563
Gan	73.170	-0.680	3.32	3.14405	0.03096	3.15146	0.02841	3.230	0.00810	3.230	0.00810
Tuticorin	78.200	8.750	3.47	2.89823	0.32692	2.91682	0.30601	3.079	0.15288	2.880	0.34810
Hanimadhoo	73.180	6.770	3.53	3.27891	0.06305	3.30675	0.04984	3.427	0.01061	3.435	0.00902
Ranong	98.580	9.970	3.67	3.80916	0.01937	3.63125	0.00150	4.011	0.11628	3.889	0.04796
Diego Garcia	72.380	-7.300	3.77	3.58712	0.03345	3.55312	0.04704	3.610	0.02560	3.594	0.03098
Thiruvananthapura	77.000	8.410	4.18	3.41059	0.59199	3.35869	0.67455	3.667	0.26317	3.115	1.13423
Minicoy Island	73.020	8.480	4.20	3.43522	0.58489	3.45877	0.54942	3.505	0.48303	3.498	0.49280
Kavaratti Island	72.710	10.530	4.52	3.75444	0.58608	3.77945	0.54841	3.819	0.49140	3.807	0.50837
Andrath Island	73.160	11.000	4.54	3.77780	0.58095	3.79897	0.54913	3.876	0.44090	3.845	0.48303
Kochi	76.200	9.580	4.64	3.87483	0.58549	3.83164	0.65345	4.277	0.13177	3.576	1.13210
Kollam	76.630	8.900	4.65	3.87688	0.59771	3.44778	1.44533	4.015	0.40323	3.331	1.73976
Khozikode	75.430	11.150	4.73	3.96322	0.58795	3.99844	0.53518	5.866	1.29050	3.774	0.91394
Port louis	57.300	20.090	5.00	6.96274	3.85235	7.07265	4.29588	6.846	3.40772	6.846	3.40772
Mormugao	73.800	15.420	5.92	5.72262	0.03896	5.68654	0.05450	5.520	0.16000	5.302	0.38192
Salalah	54.000	16.930	7.28	6.74624	0.28490	6.73459	0.29747	6.896	0.14746	6.788	0.24206
Pt. La Rue	55.530	-4.570	7.42	6.72289	0.48596	6.73947	0.46312	6.950	0.22090	6.606	0.66260
Okha	69.080	22.470	8.10	7.27520	0.68030	7.60278	0.24723	7.580	0.27040	7.570	0.28090
Lamu	40.900	-2.270	9.15	8.59115	0.31231	8.53259	0.38120	8.762	0.15054	8.423	0.52853
Zanzibar	39.180	-6.150	9.82	9.11110	0.50254	8.99027	0.68845	9.498	0.10368	9.148	0.45158
RMS					0.66947		0.69012		0.61798		0.71812

Figure 6-11: comparison of tsunami trave time using Geoware model with different grid size

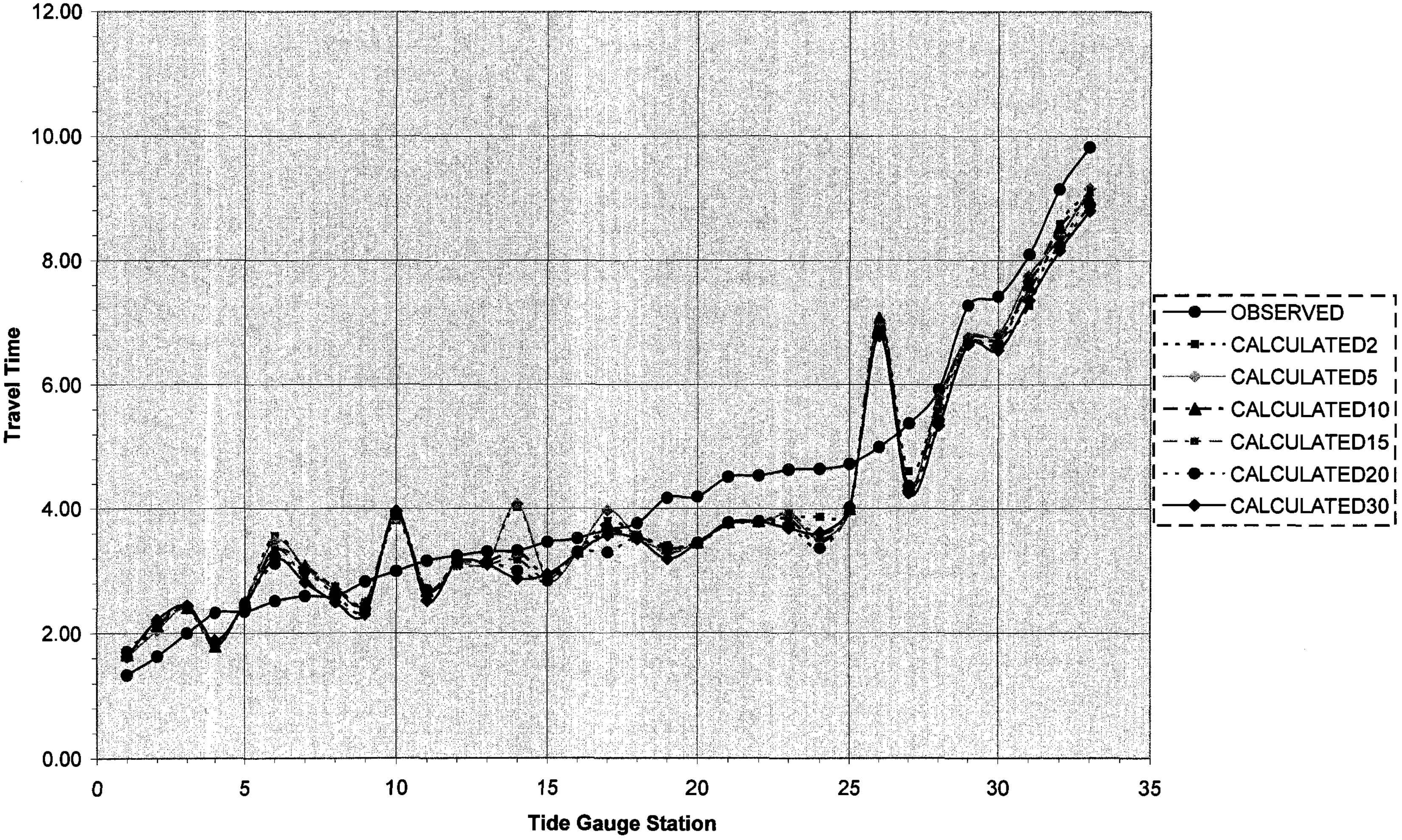

Table 6-11: Sensitivity test about wave height at different time steps

				t=3600			t=7200				
	LOCATION	LONGITUDE	LATITUDE	1min1sec.	1min3sec.	Difference	2min1sec.	2min3sec.	Difference	2min6sec.	Difference
1	A	98.33530	-0.44602	0.724891	0.7259	0.001009	0.745762	0.745712	5.00E-05	0.746005	0.000293
2	B	90.18140	-2.03715	1.15845	1.24223	0.08378	1.33454	1.33131	3.23E-03	1.30989	0.02142
3	C	97.45820	2.60634	2.56356	2.561	0.00256	2.72883	2.72905	2.20E-04	2.72992	0.00087
4	D	95.41160	4.84691	-5.49857	-5.50537	0.0068	6.37853	6.37904	5.10E-04	6.3802	0.00116
5	E	96.32120	7.50961	1.34514	1.33173	0.01341	1.45202	1.45156	4.60E-04	1.44977	0.00179
6	G	90.53880	7.21736	0.200688	0.179973	0.020715	0.715954	0.716168	2.14E-04	0.712969	0.003199
7	H	92.78030	2.34656	0.155438	0.192649	0.037211	2.67451	2.65567	1.88E-02	2.70032	0.04465
8	I	83.61670	-0.61670				1.54776	1.54448	3.28E-03	1.53858	0.0059
9	J	82.28300	3.15000				0.524378	0.52528	9.02E-04	0.526286	0.001006
10	K	88.28300	-3.41700				1.25669	1.25194	4.75E-03	1.23794	0.014
11	L	87.55000	0.61670				2.21848	2.22128	2.80E-03	2.22401	0.00273
12	M	89.71670	3.65000				1.54795	1.54705	9.00E-04	1.55432	0.00727
13	N	92.18300	2.41670				2.95569	2.96106	5.37E-03	2.89834	0.06272
14	O	95.85000	-0.88300				0.671321	0.672324	1.00E-03	0.67247	0.000146
15	P	89.18000	7.11670				0.625406	0.622298	3.11E-03	0.618075	0.004223
16	R	97.08330	8.51670				1.67818	1.67804	1.40E-04	1.67738	0.00066
17	S	82.48300	5.91670				0.472011	0.471711	3.00E-04	0.468866	0.002845
18	T	95.58300	4.38300				5.54675	5.54738	6.30E-04	5.54893	0.00155
	AVERAGE					0.0236407			2.59E-03		0.009802

Table 6-12: Sensitivity test about wave height at different spatial grid size

				t=3600					t=7200				
	LOCATION	LON	LAT	1min3sec.	2min3sec.	Difference	10min3sec.	Difference	1min3sec.	2min3sec.	Difference	10min3sec.	Difference
1	A	98.33530	-0.44602	0.7259	0.404579	0.321321	0.211743	0.514157	0.927671	0.745712	0.181959	0.68409	0.243581
2	B	90.18140	-2.03715	1.24223	1.16587	0.07636	1.32023	0.078	1.31186	1.33131	0.01945	1.37623	0.06437
3	C	97.45820	2.60634	2.561	2.40347	0.15753	1.6856	0.8754	2.96038	2.72905	0.23133	2.15069	0.80969
4	D	95.41160	4.84691	-5.50537	-3.79958	1.70579	-2.3558	3.14957	6.43825	6.37904	0.05921	4.38718	2.05107
5	E	96.32120	7.50961	1.33173	1.44335	0.11162	1.19794	0.13379	1.49898	1.45156	0.04742	1.4381	0.06088
6	G	90.53880	7.21736	0.179973	0.257182	0.077209	0.082098	0.097875	0.753387	0.716168	0.037219	0.717701	0.035686
7	H	92.78030	2.34656	0.192649	0.082149	0.1105	0.011187	0.181462	2.53311	2.65567	0.12256	2.71087	0.17776
8	I	83.61670	-0.61670						1.55025	1.54448	0.00577	1.31063	0.23962
9	J	82.28300	3.15000						0.527931	0.52528	0.002651	0.494616	0.033315
10	K	88.28300	-3.41700						1.23206	1.25194	0.01988	1.26005	0.02799
11	L	87.55000	0.61670						2.3018	2.22128	0.08052	1.99944	0.30236
12	M	89.71670	3.65000						1.66548	1.54705	0.11843	1.4256	0.23988
13	N	92.18300	2.41670						2.90577	2.96106	0.05529	2.8546	0.05117
14	O	95.85000	-0.88300						0.675394	0.672324	0.00307	0.656946	0.018448
15	P	89.18000	7.11670						0.648229	0.622298	0.025931	0.542353	0.105876
16	R	97.08330	8.51670						1.71235	1.67804	0.03431	1.30175	0.4106
17	S	82.48300	5.91670						0.430692	0.471711	0.041019	0.454464	0.023772
18	T	95.58300	4.38300						5.48519	5.54738	0.06219	4.12934	1.35585
	AVERAGE					0.3657614		0.71860771			0.063789		0.347329

Figure 6-12: locations of wave heights in the sensitivity test of numerical modeling

Figure 6-14: ETOPO1 with time step 1 second and 3 seconds at t=3600s

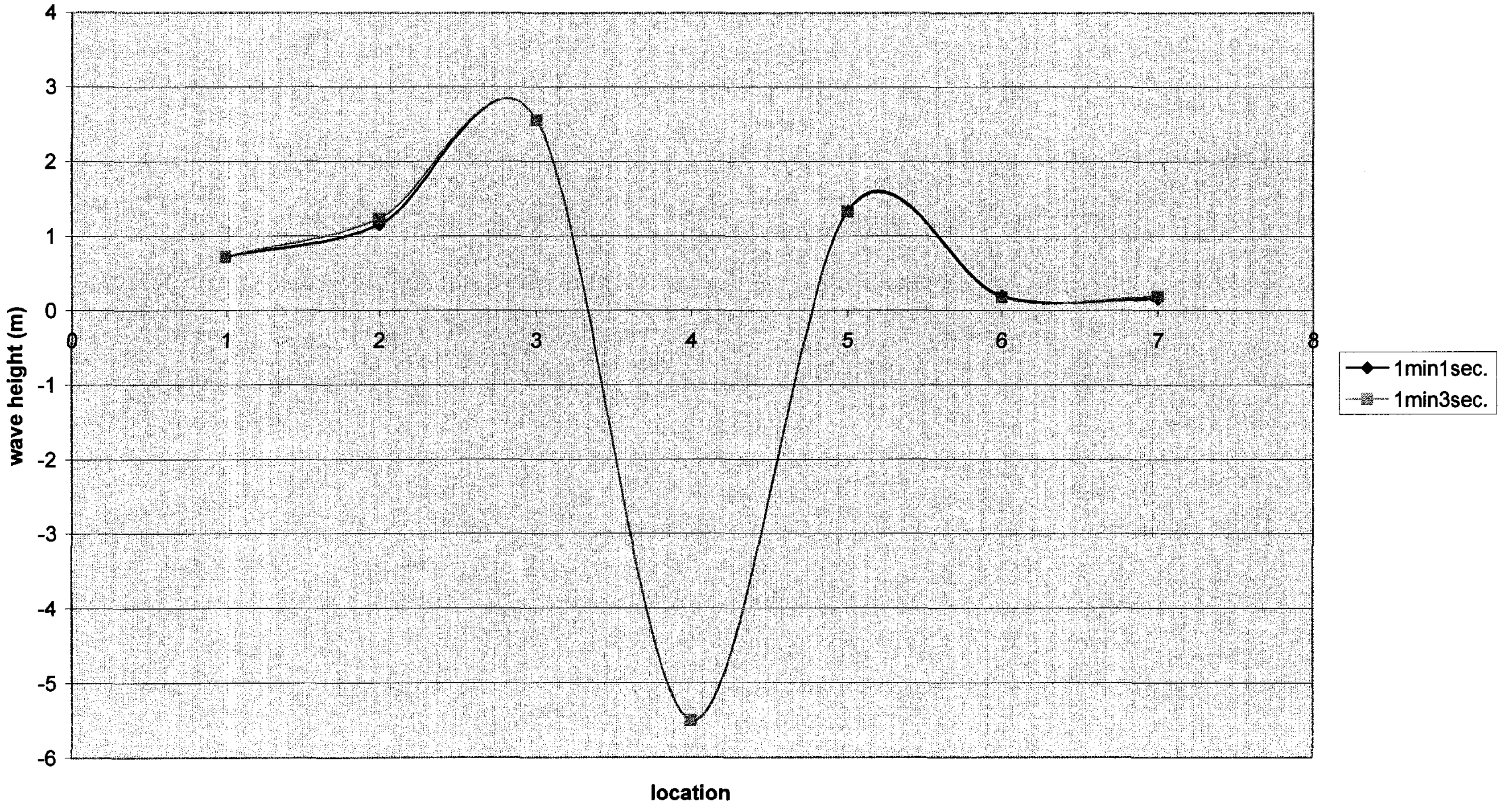

Figure 6-15: ETOPO2 with time step 1 second, 3 seconds and 6 seconds

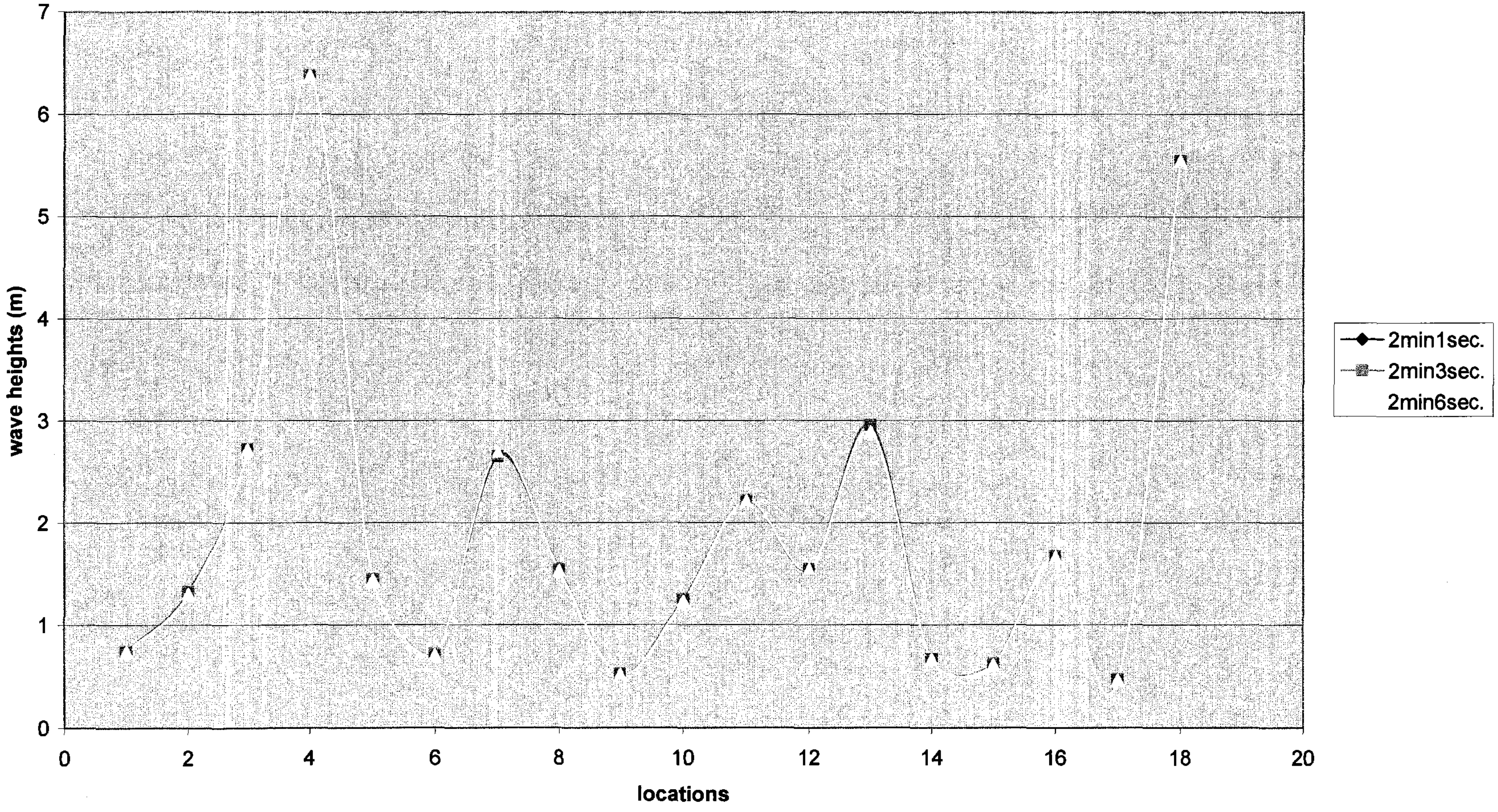

Figure 6-16: The same time step with different spatial grid size at t=3600s

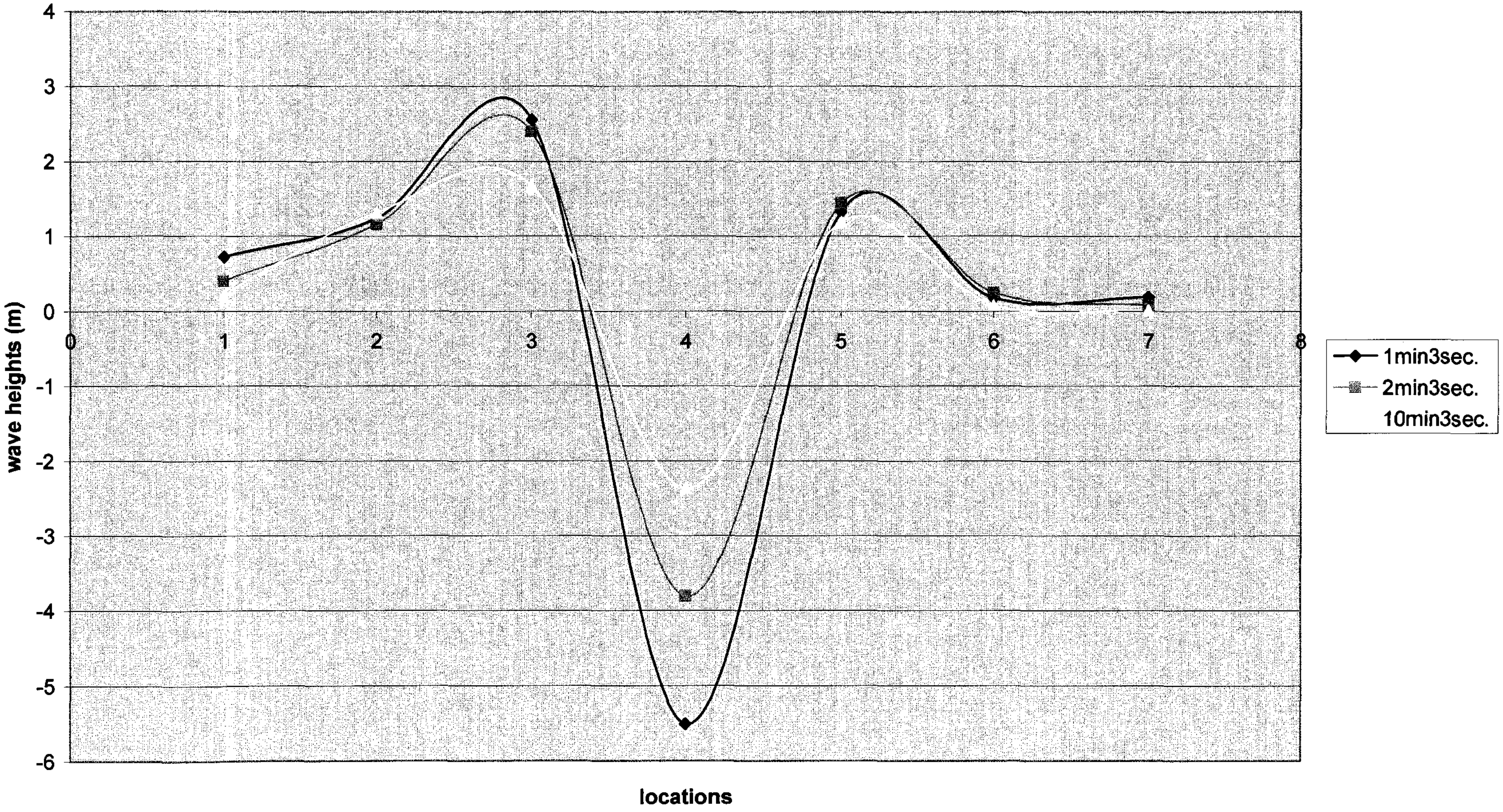

Figure 6-17: The same time step with different spatial grid size at t=7200s

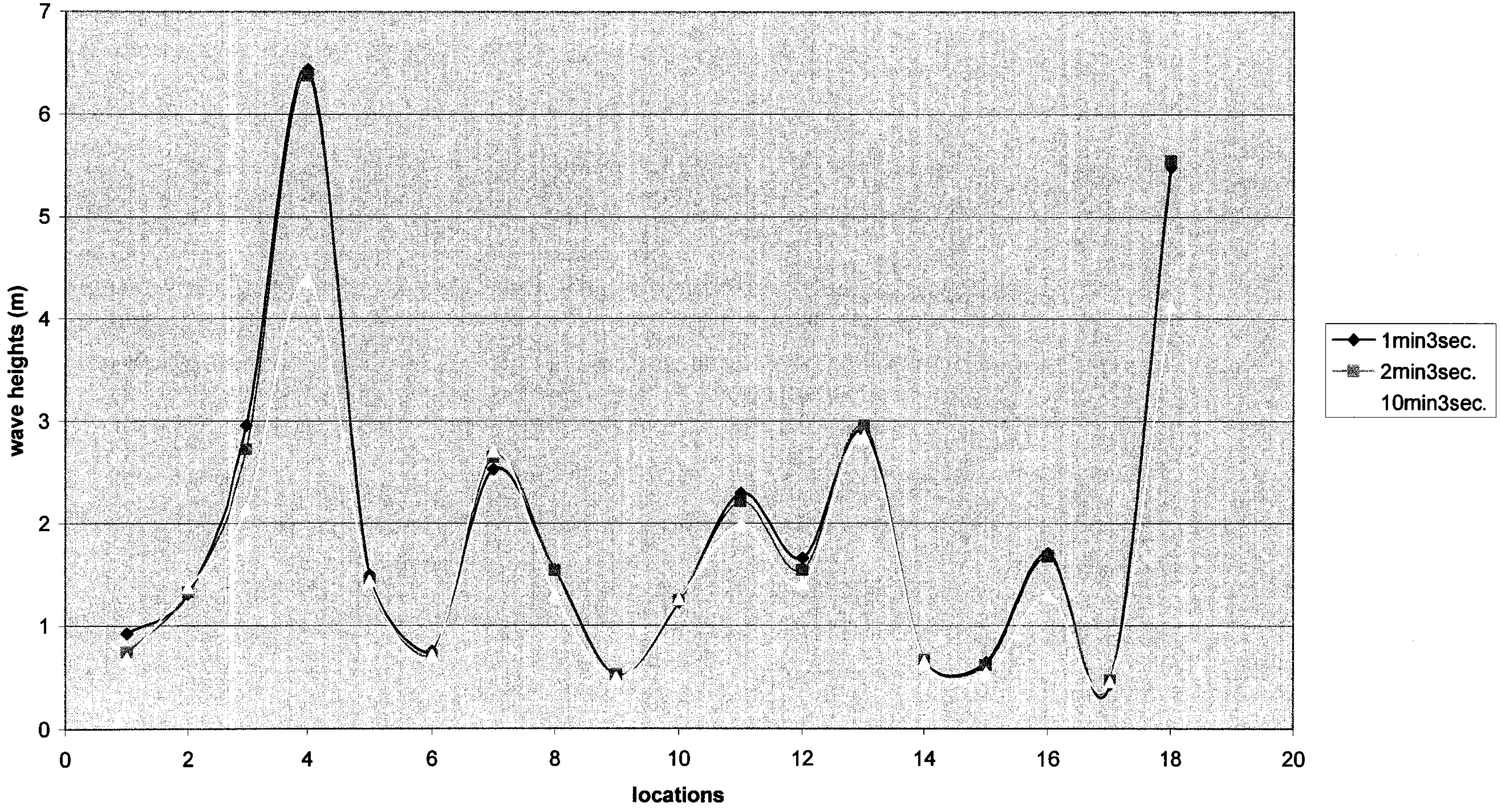

Table 6-13: Comparison of observed wave run-up with calculated wave heights

No.	Location	Survey point	Longitude	Latitude	Observed wave run-up (m)	Calculated Wave height (m)
1	Sibolga	Rhiting	95.234°E	5.429°N	48.86	3.69
2	Simeulue	Laubang	96.26°E	2.432°N	1.50	0.27
3	Sumatra	Sibolga (gauge)	98.785°E	1.729°N	2.60	1.079
4	Thailand	Kuraburi	98.083°E	9.133°N	3.20	1.76
5		Krabi	99.20°E	8.167°N	2.10	0.989
6		Ranong	98.583°E	9.967°N	1.00	0.25
7		Ta Phao Noi	98.033°E	7.667°N	1.45	0.62
8	India (Chennai)	Pattinapakkam	80.279°E	13.021°N	2.70	0.925
9	Sri Lanka	Colombo	79.83°E	6.93°N	2.17	0.689
10		Panadura	79.917°E	6.70°N	5.60	2.08
11		Unawatuna	80.242°E	6.008°N	3.30	0.69

6.10. Discussion of sensitivity analysis

Although several authors claimed that their models reproduced the Indian Ocean tsunami very well. In reality this is not the case. Maximum errors up to 30% and average errors of up to 20% occurred in my numerical model simulations. The reasons for these large errors could be the following:

1. Bathymetric uncertainty contributes to large errors. The author had specified the depth values for the geographical points along the great circle arc. However, the depth data for these locations, when taken from ETOPO2, did represent the depth values for other locations, being outside the great circle arc. It was hard to determine the correct locations for the depth values from ETOPO2. The error was also true for the Andaman Sea.

2. Tide gauge records somewhat underestimate tsunami wave height but are reasonably accurate for the travel times. According to seismological data, the Indian Ocean earthquake actually did not happen in one instant, but lasted quite a few minutes. The interval between the main-shock and the after-shock was 100 seconds, and also they occurred at different places. For the Indian coast, the distance from the main-shock is greater than for the after-shock, but obviously the main-shock happened a little earlier than after-shock. So which leading wave first arrived on the Indian coast depended on the distance, earthquake time interval, wave frequency, etc. this contributed to significant error.

3. The satellite altimetry analysis (Kulikov *et al.,* 2005) showed that the tsunami wave was a combination of short-waves and long-waves, so their speed was different. In the case where the wave generated from the after-shock, they may travel faster; the distance is shorter, and as a result, the tsunami from the after-shock may arrive at the Indian coast earlier than of it was generated by the main-shock . But in our simulation of the tsunami travel time, we assume that the tsunami epicenter is only a point source, and then, the wave spread out in each direction. This introduces considerable error.

4. The wave speed used in the type of codes mentioned above is calculated using $c = \sqrt{gH}$. This is an approximation that starts to break down when the water depth is very shallow, especially near coastal areas. The real wave moves slower than the simulated waves. The

model solutions that depart more from the observations are those where the wave ray path has to travel longer on very low water depths, such as for the Port Louis, Paradip, Tuticorin, Ta Ru Tao tide gauges which are located well near land. So the larger errors in these cases are due to long travel distances over shallow water.

Compared with tsunami travel times, wave heights are affected by even more factors. Once the initial wave is generated from the earthquake, tsunami wave height is modified by the ocean bathymetry. In this thesis, the spatial grid size and time step were used to test the sensitivity of wave heights at different locations.

Table 6-10 displays the sensitivity test results for the time step variation. When the input bathymetry is ETOPO1, the time step for numerical integration must be less than 4.6 seconds to keep the program stable. Using two different time steps of 1 second and 3 seconds , the snapshot of solutions at an elapsed time of 1 hour shows that the wave heights are almost the same; the average difference is 0.023 meters. The program crashes when the time step is increased to 6 seconds. When the input bathymetry is ETOPO2, the maximum allowable time step for numerical integration is 9.26 seconds. Three different time steps, 1 second, 3 seconds, and 6 seconds were used to test the sensitivity of wave heights. The same behavior as shown above occurs. The wave heights are not sensitive to the time step, the average difference being 0.003 meters, and this difference can be ignored. .Normally the smaller the time step, the better the resolution. But a smaller time step will increase the computation time sharply, leading to increased computer resource cost. Therefore, under the restriction of computer resources, we can choose a larger time step within the required limitation of numerical stability in the integration.

On the other hand, the results obtained from the sensitivity tests on the spatial grid size indicate that wave height is very sensitive to the spatial grid size. The maximum difference of wave heights from the spherical 1 minute bathymetry to the spherical 10 minutes bathymetry is up to 2.0 meters; the average difference between wave heights is 0.3 meters. The smaller the spatial grid size, the bigger the wave heights. In reality, even with spherical 1 minute's bathymetry, the spatial grid size is still coarse and the distance between two successive grids is 1.852km. This indicates that, in the process of numerical modeling, in order to obtain wave heights which can simulate coastal inundation realistically, one should establish a finer spatial scheme which would resemble the real bathymetry. In the coastal areas, the real bathymetry is more complicated than in deep ocean and, within a mere 100 meters distance, the elevation difference of the bottom can reach 1000 meters or even more and be dotted with islands and sand bars. Since wave heights determine inundation, a bathymetry with no more than several meters spatial grid size must be used in order to simulate the process of tsunami wave approaching the shoreline.

In summary, bathymetry has a strong impact on tsunami travel times and wave heights. The current model, with its coarse resolution, does not allow for a precise point-by-point comparison with individual field observations. With improvements in computer resources, and better bathymetry, smaller and smaller grid size (up to several meters) should be used to compute the inundation at specific locations; thus, an inverse calibration of the numerical model can be done using field observations. Moreover, the Indian Ocean Tsunami is not a good benchmark to calibrate numerical models because of lack of accurate nearshore bathymetry.

7. NUMERICAL MODELING OF THE NOVEMBER 28, 1945 ARABIAN SEA TSUNAMI

7.1. Historical tsunamis in the Indian Ocean

In the Indian Ocean region, two potential earthquake sources have been identified, namely the Sunda Subduction Zone (Andaman to Sumatra region) and the Makran Subduction zone. The Makran coast of Pakistan is known for generating tsunamigenic earthquakes and the oldest recorded earthquake and tsunami event in this region dates back to 325BC during the time of Alexander the Great. There are a number of unconfirmed reports about tsunamigenic earthquakes in the vicinity of the Makran coast. However, the most recent and well-documented tsunami occurred on November 28, 1945. A list showing the tsunamis that affected the Indian coast in the past two thousands year is given in Table 7-1. Though the historical archives were not properly always documented, the information in the table is authentic but sketchy and cannot be fully confirmed, except for the tsunami of 26th December 2004 event. Though the time gap between first and second event and second and third event is large, there might be some tsunamis which may not have caused destruction and thus escaped historical records. The lists of tsunamis in the Indian Ocean basin indicate that there is a major event roughly every sixty years, with minor events occurring every ten years.

7.2. Makran Subduction Zone (MSZ)

A complicated pattern of tectonic microplates and areas of both subduction and upthrust characterize the region. The MSZ in the Northern Arabian Sea was formed by the northward movement of the Oman oceanic lithosphere and its under thrusting of the Iranian micro-plate at a very shallow angle of about 20 degrees. Convergence rate between the Arabian and Eurasian Plates was estimated to 30-50 mm/year (Platt *et al.* 1988). The east-west trending MSZ is more than 900 km long. High compression and seismic activity characterize the entire tectonic boundary along both the eastern and western sections of the thrust; while large tsunamigenic earthquakes can be expected mainly on the eastern portion of the subduction zone. As in the past, large destructive tsunamigenic earthquakes can occur along major faults in the east Makran region, near Karachi, as well as along the western end of the subduction zone. The trench associated with the present accretionary front does not have much of a morphological relief as other trenches around the world's oceans. Extensive erosion of the Himalayan mountain ranges and the numerous rivers which flow into the North Arabian Sea have buried the trench with sediments with thickness of up to 7 km (Closs *et al.*, 1969, White and Louden, 1983). Complex, kinematical earth movements along the boundaries of such active zones caused numerous destructive earthquakes in India, Pakistan, Afghanistan, Iran and Tibet in recent years.

Table 7-1: List of tsunamis that affected India Ocean Area

Date	Remarks
October – November, 325 BC	The impact of the 325 BC tsunami in the region was probably very similar to what happened with the 1945 Makran tsunami.
6 or 7 September, 1524	Geological evidence shows that large tsunamis occurred in the Arabian Sea. The sand deposit is located on the southern side of the Bharja river delta at Dapoli taluka of Ratnagiri. It triggered a rise in the sea level of 3 to 4 meters above the present level.
12 April, 1762	Earthquake in Bay of Bengal. Tsunami wave of 1.8m at the Bangladesh coast.
19 August, 1868	Earthquake of magnitude 7.5 in Bay of Bengal. Tsunami wave of 1.8m at the Bangladesh coast
31 December, 1881	Earthquake of magnitude 7.9 in Bay of Bengal. Tsunami wave run up level of 0.76m at Car Nicobar, 0.3m at Nagapattinam, 1.22m at Port Blair.
August 27th 1883	Earthquake in the west part of the bay of Bengal. Tsunami at Port Blair, Doublet (mouth of Hoogly River). East coast of India was affected; 2m tsunamis were recorded at Chennai.
26 June 1941	Earthquake of magnitude 8.1 in the Andaman Sea at 12.9^0N, 92.5^0E. Tsunami on the east coast of India with amplitudes from 0.75 to 1.25m. Some damage from East Coast was reported.
27 November, 1945	Makran Earthquake (magnitude 8.1). 12 to 15m wave height in Ormara in Pasni Considerable damage in Makran coast. In Gulf of Cambay of Gujart, wave heights of 11-11.5 m were estimated. Damage reports from Gujarat coast were not available. The estimated height of waves at Mumbai was about 2 m, boats were taken away from their moorings; and the waves killed more than 4000 people.
26 December, 2004	Earthquake of magnitude 9.3 off north Sumatra coast generated devastating Tsunami waves affecting several countries in South East Asia. In India, Andaman & Nicobar Island, Tamil Nadu, Pondichery, Andhra, Kerala affected about 365,000 people and caused about 15,000 deaths.

There is no obvious topographic trench associated with the present accretionary front. Quittmeyer (1978) claims that the recent seismicity in the west region of the area suggests that the western region of the 1945 earthquake may be the site of the next large earthquake. Therefore this region should be closely monitored in the future. Figure 7-1 shows the geographical features and tectonic structures of Makran coast of Pakistan.

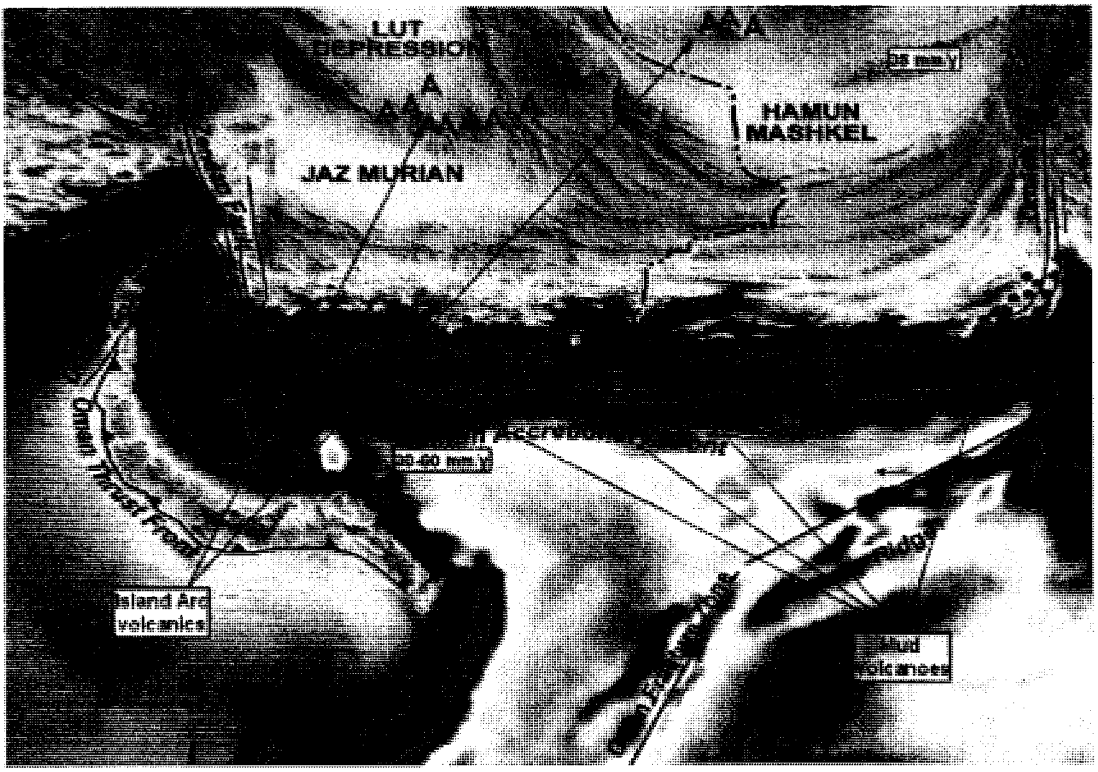

Figure 7-1: the geographical features and tectonic structures of the Makran coast of Pakistan (Mokhtari, 2005)

Most of the earthquakes in this region of South Asia occur mainly on land, along the boundaries of the Indian tectonic plate and the Iranian and Afghan micro-plates. At least 28 earthquakes with magnitudes close to 7 or over 7 are known to have occurred in this region from 1668 to present (Ambrasseys and Bilham, 2003). Figure 4-2 shows locations of major earthquakes and tsunamis in the Oman Sea, Pakistan, India and surrounding regions. One of requirements for tsunami occurence is that the tsunamigenic earthquakes should occur underneath the sea floor and that their magnitude must be higher than 7 on the Richter scale.

The active subduction zone along the Makran coast of Pakistan produced many tsunamigenic earthquakes in the past and is a region with significant potential for future destructive tsunamis. Although the occurrence of a large earthquake along the Makran Subduction Zone is infrequent, the potential for the generation of destructive tsunamis in the Northern Arabian Sea cannot be overlooked. Recent advances in geological and paleotsunami studies have identified the MSZ as a substantial seismic and tsunami hazard for the Arabian Sea Area. The earthquake on November

28, 1945 generated a destructive tsunami in the Northern Arabian Sea and in the Indian Ocean. More than 4,000 people were killed in Pakistan by the combined effects of both the earthquake and the associated tsunami. However, it was the tsunami that was responsible for most of the loss of life and destruction, which occurred along the coasts of Iran, Oman and north-western India (PC, 2006b).

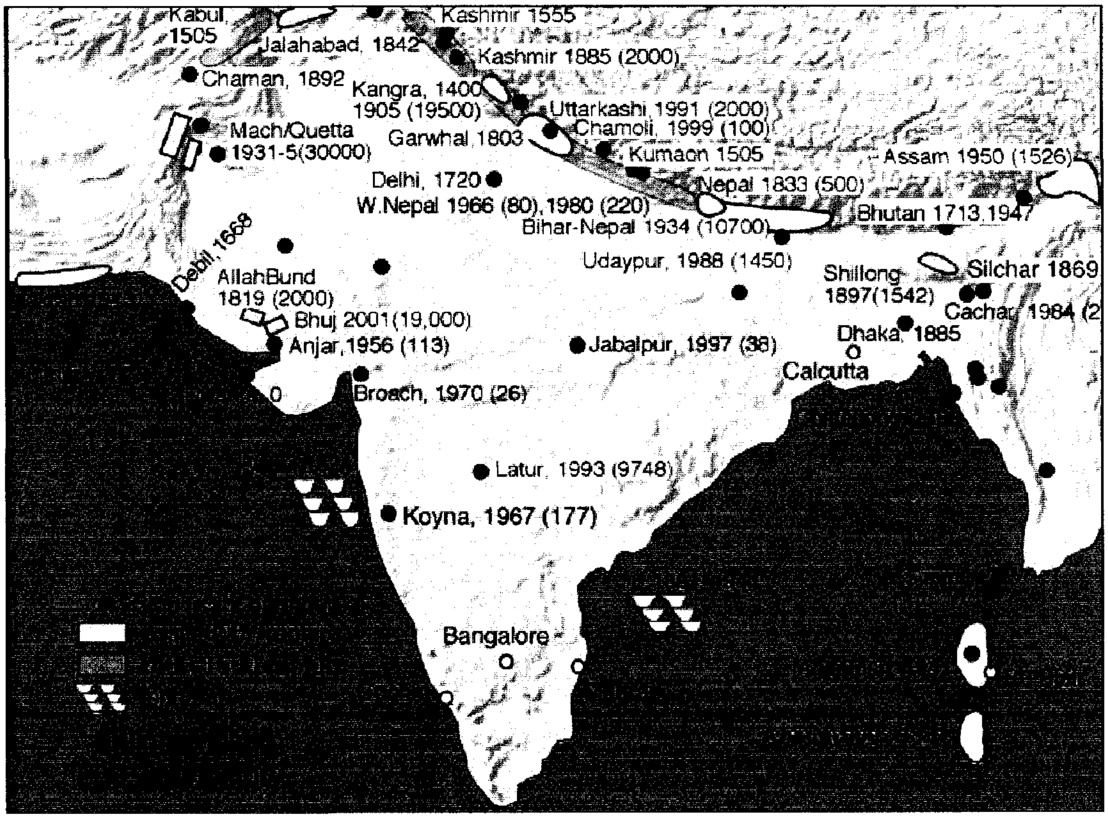

Figure 7-2: Major earthquakes and Tsunamis in Arabian Sea and surrounding regions (NASA, 2004)

7.3. November 28, 1945 tsunami modeling

The details of the tsunami generation are extremely important when the shoreline is in close proximity to the tsunami source. The latest scientific evidence about the MSZ fault structure and its seismicity is employed to predict a tsunami source scenario for this study. The great Makran earthquake occurred at 21:56 UTC (03:26 IST), on November 28, 1945. Its epicentre was located at latitude 24.5N, longitude 63.0E; at a distance of 150-400 km from the Makran coast; off the eastern segment of MSZ in the northern Arabian Sea, and about 100 km south of Karachi and about 87 km SSW of Churi (Baluchistan), Pakistan. The quake's focal depth was 25 km and its magnitude was evaluated to be 8.1 on the Richter scale (Pacheco and L. Sykes, 1992). The length of its rupture is estimated to be about 300-350 km. The thrust faults were oriented nearly perpendicular to the direction of convergence. The subduction plate had a northward dip of greater than 20^0 till 270N, then bended down to an angle of approximately 300^0. The observed maximum wave had a height of 1.98 meters in Karachi. The first wave was recorded at 5:30 a.m., then subsequent waves occurred at 7:00 a.m., 7:15 a.m. and, finally, at 8:15 a.m. The last wave (at 8:15 a.m.) was also the biggest. The tsunami had a height of 11.0 - 11.5 m in Kutchh, Gujarat. At 8:15 a.m., it was observed in Salsette Island, in Mumbai and was also recorded in the Harbour. The tsunami was also observed at Versova (Andheri), Haji Ali (Mahalaxmi), Juhu (Ville Parle) and Danda (Khar). The average velocity of tsunami waves in deep sea in the area analyzed is about 650-700 km/hour. Keeping in mind these figures, the tsunami arrival time on Pakistan coast was of the order of 20 to 40 minutes. Effectively, there are only 15 to 35 minutes available for evacuation, even in the best of circumstances. In other words, this tsunami scenario, near the coastal areas, is much more dangerous than that of the 2004 Indian Ocean tsunami, where the tsunami took more than two hours to arrive to the Indian coast. However, the same situation occurred for the Banda Aceh region where the tsunami hit the coast in less than 30 to 40 minutes. Figure 7-3 shows tsunami travel times for several locations in the North Arabian Sea. Within 2 hours, the tsunami travels to Karachi; within 4 hours the tsunami spreads to Mumbai, and within 5 hours the tsunami reaches Sri Lanka. These calculated tsunami travel times agree well with the existing records. The red and yellow areas in the shadow of Sri Lanka suggest that the tsunami takes longer to arrive there due to wave diffraction and refraction.

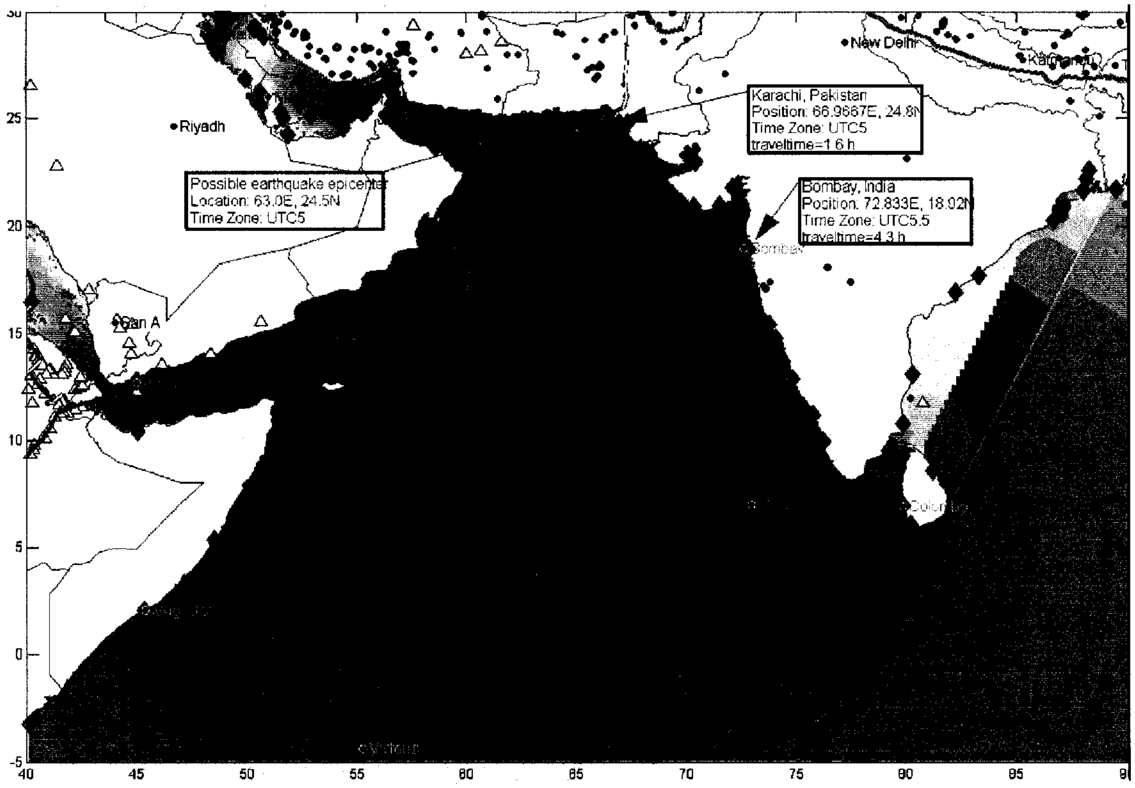

Figure 7-3: Computed tsunami travel time for the November 28, 1945 MSZ tsunami

Figure 7-4 shows the maximum wave heights and directionality of the November 28, 1945 MSZ tsunami. In the region of earthquake source, the northern part of the Arabian Sea, the computed maximum wave heights are close to 6 meters for the coarser grid size of 2 min of arc, while wave heights in the region of Karachi are close to 2 meters. This agrees well with the observed values. When the waves approach the ridges of the Arabian Sea, they interact with the shallow submarine ridges and the wave energy was trapped inside. Hence, wave amplitude is amplified. As the Arabian Sea is relatively shallow compared with the Indian Ocean, wave heights become thus even higher. Also, tsunami waves send a strong signal into the south Indian Ocean. Due to the extremely shallow opening of the Persian Gulf, most of the wave energy was trapped inside the Arabian Sea and thus, significant increases in the wave heights in the nearshore areas of Pakistan and India are observed; while wave heights in the Persian Gulf are relatively lower. The Oman coast was fairly impacted by tsunami waves as it was exposed to open ocean and thus takes the brunt of the tsunami force.

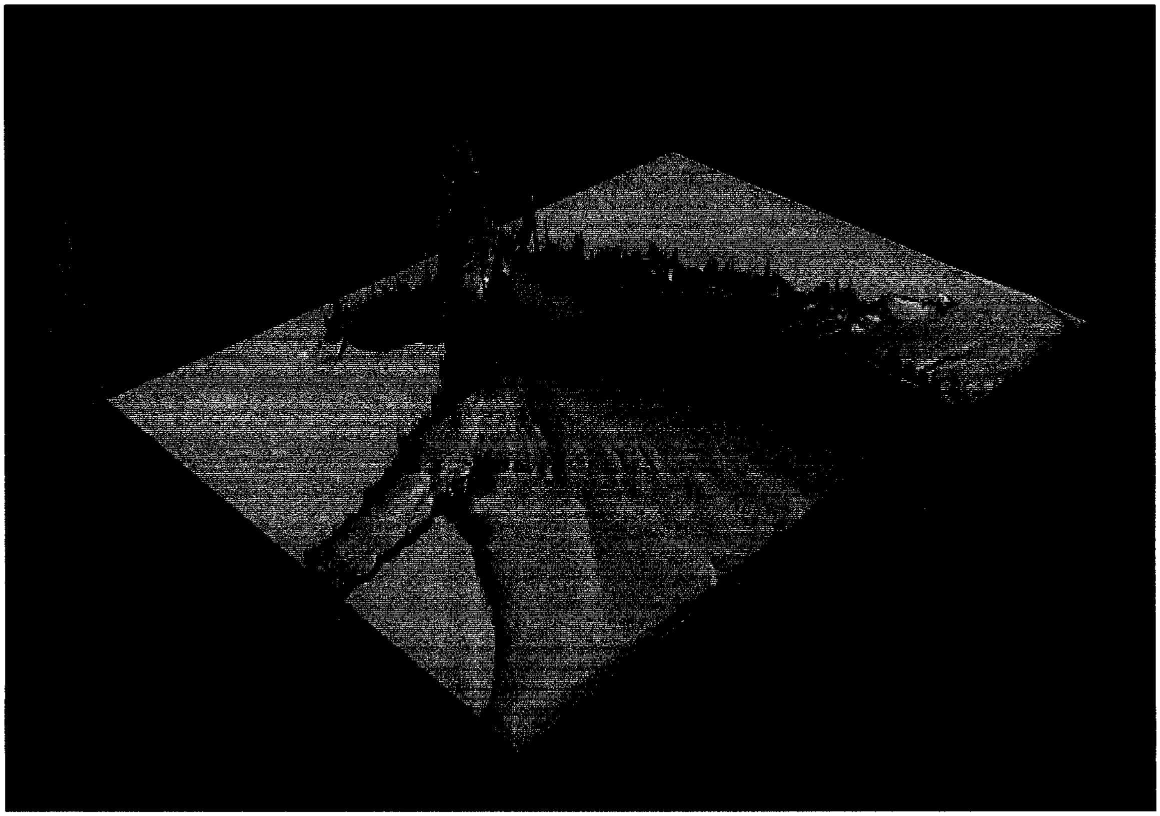

Figure 7-4: Maximum wave height and directionality of the November 28, 1945 tsunami

Several other figures demonstrating the processes of tsunami propagation are shown in the appendix. Figure A-7 shows snapshots of the water surface elevation and maximum wave heights of November 28, 1945 MSZ tsunami at different time steps into the computation: t=500s, 1000s, 2000s, 3000s, 4000s, 5000s, 6000s, 7000s and 8000s after earthquake occurrence.

8. TSUNAMI RISK FOR WESTERN CANADA AND NUMERICAL MODELING OF THE CASCADIA FAULT TSUNAMI

This part of the thesis deals with the analysis of the tsunami risk for western Canada and the numerical modeling of a potential tsunami which could affect the region and cause significant damage to the western Canadian coastline. Following a review of the seismic risk and of historical tsunamis which occurred along the western Canadian coastline, the author concluded that this region is highly vulnerable to a major tsunami in the near or distant future. Consequently, the author conducted a study on the numerical modeling of a possible tsunami generated by the Cascadia fault, which is located offshore of British Columbia. The results of the model outline the significance and extent of the coastal flooding risk associated with such a rare, but destructive phenomenon. The potential for inundation of the low-lying areas around the coastlines of Vancouver Island and in and around the City of Vancouver was found to be high. A number of recommendations and conclusions focusing on the results of the numerical simulation are included.

In general, the Pacific Ocean region has received more attention from tsunami scientists and engineers than any other region on the globe. These efforts materialized into the implementation of a tsunami early warning system which benefits all countries around the Pacific Rim. Having a relatively long coast on the Pacific Ocean, Canada is an active participant in the Pacific Tsunami Early Warning System. Although population density along the western Canadian coastline is relatively low when compared to the case of other countries surrounding the Pacific Ocean such as Japan, US or Korea, several major Canadian communities are located along the coastline. Vancouver and Victoria are two of the largest Canadian coastal municipalities with a population of 2.186 million and 335,000 inhabitants, respectively. These cities are located in relatively low-lying areas, with significant potential for coastal flooding due to a possible tsunami. Several major offshore geologic faults are located relatively close to the shoreline. The current West Coast Tsunami Early Warning System is effective in the case of far-field tsunamis, but it may not be as effective for a locally-generated one. Moreover, considering also the high level of seismic activity in the area, there is increased awareness and interest in analyzing the possibility of occurrence of such an event, its foreseeable effects and the possible prevention and/or mitigation measures that must be taken into account by the provincial and federal government bodies.

8.1. Seismic risk for Canada

In Canada, the evaluation of regional seismic hazard is the responsibility of the Geological Survey of Canada. Seismic hazard maps prepared by the Geological Survey are derived from statistical analysis of past earthquakes and from developing knowledge of Canada's tectonic and geological structure. On these maps, seismic hazard is expressed as the most powerful ground motion that is expected to occur in a certain area for a given probability level. Contour lines delineate regions which would likely experience similarly strong ground motions. A simplified seismic hazard map shown in Fig. 8-1 indicates the distribution and magnitude of the earthquakes which occurred across Canada between 1660 and 2004 (for which written or oral accounts exist), as well as the location of the ten most powerful earthquakes in Canada. For convenience Canada has been divided into earthquake source regions based on past earthquake activity and tectonic structure. The relation between earthquake magnitude and the average rate of occurrence for each region is weighed, along with variations in the attenuation of ground motion with distance. In calculating seismic hazard, scientists consider all earthquake source regions within a relevant distance of the considered site. Spectral acceleration is a measure of ground motion that takes into account the sustained shaking energy at a particular period.

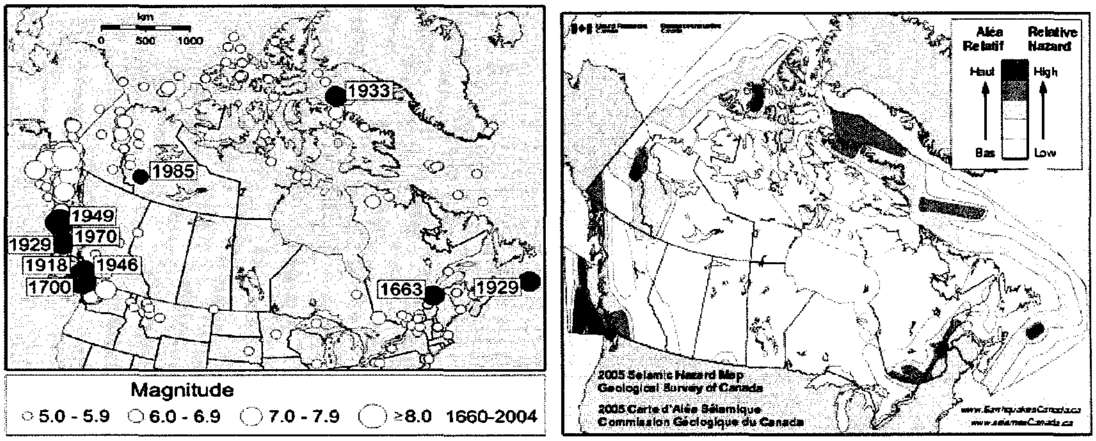

Figure 8-1: Earthquake distribution and seismic risk in Canada (GSC, 2006)

Subduction earthquakes are particularly effective in generating tsunamis. As seen in Fig. 8-1, the major risk for an earthquake capable of generating a tsunami which could affect the Canadian coastline lies along the western seaboard. For the case of the Arctic Ocean, though the risk of a tsunami occurring is real, the extremely low population density, the presence of numerous islands, as well as the extensive permanent ice cap are reasons why implementation of a warning system is less of an immediate objective. For the case of the Atlantic Ocean coastline, the situation is somewhat different. Fig. 2-5 shows the Atlantic Ocean and the mid-Atlantic ridge, which is a divergent plate boundary, and hence does not give rise to tsunamigenic earthquakes. Normally, there are no ocean-wide tsunamis in the Atlantic, and most tsunamis are local, for example, occurring in the Caribbean Sea. The Lisbon earthquake tsunami of 1755 was supposed to have had several meters of amplitude in the Caribbean, but was not significant along the western Atlantic coastline. Consequently, the current paper focuses on the possibility of a tsunami being generated in the western coast of Canada (along the shorelines of British Columbia).

According to the past three decades of seismologic research and observations, it appears that the western seaboard of Canada has the highest risk of being hit by an earthquake-generated tsunami. This is mainly due to the existence of a system of faults that has the potential to – just as in the past – generate tsunamis. The Cascadia Subduction Zone (CSZ) is a long sloping fault that stretches from mid-Vancouver Island to Northern California with a very large fault area; it is the outer boundary which separates the Juan de Fuca and North American plates. Since earthquake magnitude is proportional to the fault area, the CSZ could produce a very powerful earthquake with a magnitude of 9.0 on the Richter scale or greater, if rupture occurred over its entire area. Scientists have collected compelling evidence on earthquakes and tsunami events originating from the CSZ fault. Estimates of the return period for a large event on this fault are not well established (probably, in the millennia range). Nevertheless, the proximity to a large metropolitan area makes the risk from such an event formidable and warrants a thorough scientific investigation. It is almost certain that a tsunami will accompany a large rupture on the CSZ Fault. As more material wells up along the ocean ridge, the ocean floor is pushed toward and beneath the continent. Fig. 8-2 shows subduction of the oceanic Juan de Fuca plate beneath the continental crust of North America.

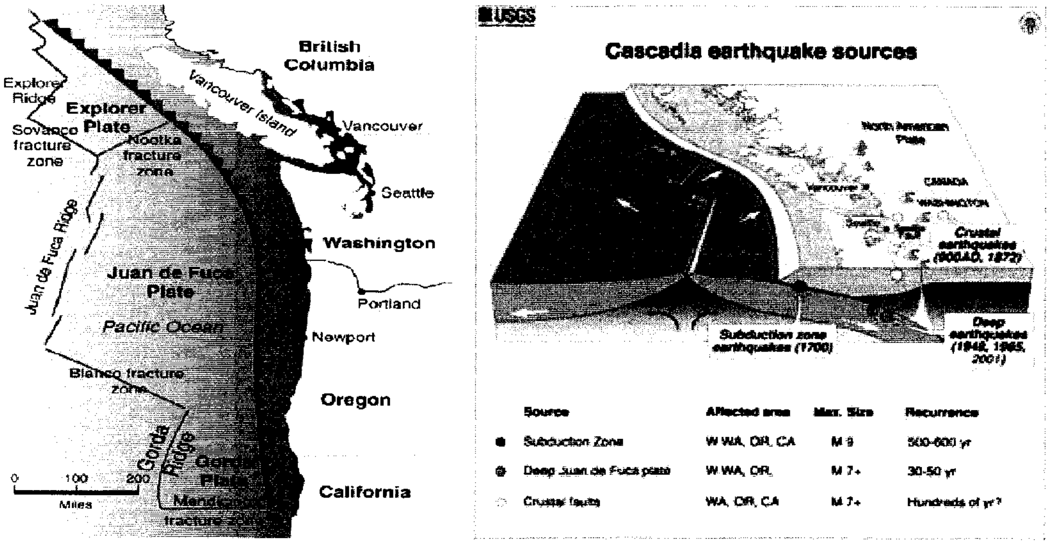

	Source	Affected area	Max. Size	Recurrence
●	Subduction Zone	W WA, OR, CA	M 9	500-600 yr
◉	Deep Juan de Fuca plate	W WA, OR	M 7+	30-50 yr
○	Crustal faults	WA, OR, CA	M 7+	Hundreds of yr?

Figure 8-2: Location of the Cascadia fault and subduction zone (Thatcher 2001, USGS 2005)

Thatcher (2001) mentioned that "the CSZ last experienced a great earthquake in 1700 and so may be only about halfway through its approximate 600-year earthquake cycle". However, other regional faults may be closer to failure and such episodic events could lead to large earthquakes. Continuous monitoring of these faults, in Cascadia and elsewhere, is therefore important. The width of the CSZ fault varies along its length, depending on the temperature of the subducted oceanic slab, which heats up as it is pushed deeper beneath the continent. As it becomes hotter and more molten, it eventually loses the ability to store mechanical stress and generate earthquakes. The "locked" zone is storing up energy for an earthquake, and the "transition" zone, although somewhat plastic, could rupture.

8.2. Historical tsunamis affecting western Canada

There is large geological evidence in the tidal marshes along the Pacific coast from Vancouver Island to northern California for repeated, historically unprecedented, massive earthquakes in the recent past. Geological evidence indicates that major earthquakes may have occurred at least seven times in the last 3,500 years, suggesting a return period of 400 to 600 years. The latest known major earthquake in the northwest occurred in January 1700, just over 300 years ago. The ensuing tsunami moved across the Pacific Ocean and produced destructive waves up to several meters high along a 1000-km length of the coast of Honshu in Japan. Much larger waves struck the west coast of North American less than 30 minutes after the shaking stopped. Deposits from this tsunami are preserved in tidal marshes and low-elevation coastal lakes on the Pacific coast. Their distribution provides information on the wave run-up that could be expected from future Cascadia fault-generated tsunamis.

Tsunamis along coastal British Columbia were generated by remote or local earthquakes. For example, in 1964, a large earthquake in Alaska triggered a tsunami that caused damage all the way to California, including several million dollars damage in Port Alberni, British Columbia. In the case of the local tsunami source, the Cascadia subduction zone earthquake seems to be the main factor. While there were several tsunamis which affected the western Canadian coast, the most important ones are briefly described below.

1700 Cascadia Tsunami

The January 26, 1700 Cascadia earthquake had a moment magnitude 9 on the Richter scale. Reports of damage and flooding show that the 1700 Cascadia tsunami run-up reached heights of 1 to 5 m at seven shoreline locations along Japan's eastern coastline. An estimate based on seismological analysis shows that tsunami wave height reached 16 m near Vancouver Island. The exact location of the rapture extent and destruction in Canada is not known.

1946 Aleutian Tsunami

On April 1, 1946, at 12:29 GMT, an earthquake occurred in the Aleutian Islands of Alaska. A Pacific-wide tsunami was triggered by the earthquake, which had a magnitude of 7.8 on the Richter scale, with an epicenter located at 52.8° N, 163.5° W, with a focal depth of 25 km. Before tsunami waves dissipated, they took the lives of more than 165 people and caused over $26 million (1946 US dollars) damage.

1964 Prince William Sound Tsunami, Alaska

On March 28, 1964, at 03:28 GMT, the second largest earthquake of the twentieth century (magnitude 9.2 on the Richter scale) occurred in Prince William Sound, Alaska, triggering a Pacific-wide tsunami. The main tsunami wave swept southward across the Pacific Ocean, with a velocity of about 830 km/h, reaching Antarctica in only 16 hours. The earthquake had a surface-wave magnitude of 8.4, and an epicentre located at 61.1° N, 147.5° W, with a focal depth of 23 km. The earthquake, the local tsunamis generated by landslides, and the regional tsunami were responsible for taking the lives of more than 130 people and causing over $106 million in damages. Two hundred and sixty homes in Port Alberni were damaged.

Canada and other members of the international community participate in the Pacific Tsunami Early Warning System, which provides alerts for tsunamis on the west coast to the federal and British Columbia governments. The Government of Canada and its international partners are working together to extend the existing coverage for tsunami warnings so as to provide global protection. The government operates a national seismographic network through Natural Resources Canada. This network provides a warning and alert system for earthquake activity on or near the Canadian territory. On January 18, 2005, the government of Canada announced $850,000 to assist the Province of British Columbia in establishing a jointly-funded program to allow coastal communities to set up training, telecommunications and tsunami warning capabilities. The Government of B.C. currently works toward ensuring that vulnerable coastal communities in B.C. conduct tsunami risk assessments, prepare plans that include recommendations for communications and notification enhancement, and review best practices to deal with tsunami hazards.

8.3. Earthquake characteristics and tsunami generation

Many details of the CSZ Fault are still poorly understood. The amplitude and geographical extent of the next CSZ megathrust earthquake are, of course, unknown. The tsunami generation, however, depends only on the surface manifestation (the amount of vertical offset) of the internal fault rupture. Therefore, the internal fault geometry, though important, may not be as vital a constraint for the tsunami model as the vertical deformation evidence. The author therefore investigated the tsunami waves that may originate from a simple, single-fault mechanism which was assumed for the earthquake source. First, the scenario assumes a major (magnitude 9.0 on the Richter scale) earthquake. The earthquake will generate the biggest tsunami wave on the British Columbia coast — Vancouver Island, and emphasis is placed on the northern part between latitude 45°N and 50°N. Combining six scenarios (Satake *et al.*, 2003) based on the 1700 CSZ megathrust tsunami with the directionality towards Vancouver Island, one scenario was provided with tsunami amplitudes being the largest on the path to Vancouver Island and perpendicular to the fault strike orientation (Ben-Menahem and Rosenman, 1972). Especially for the long rupture model, most tsunami energy from the CSZ is directed towards the northwestern Pacific Ocean and Vancouver Island (Fig. 8-3).

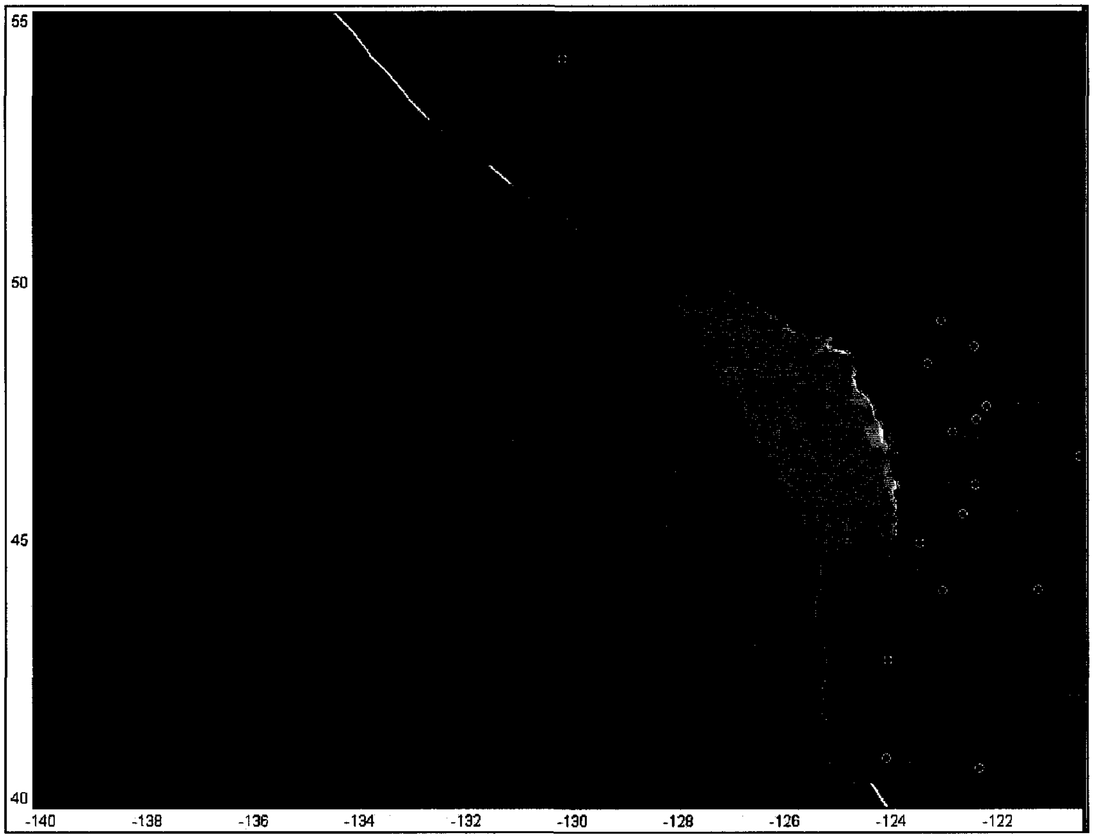

Figure 8-3: Direction of maximum tsunami amplitudes

Permanent, vertical sea floor displacement is computed using the static dislocation formula of Okada (1985). The Harvard solution, derived by inverting seismic data, provided estimates of the moment magnitude ($1 - 9 \times 10^{22}$ Nm), strike (340°), dip (12°), and rake (90°). The aftershock distribution was used to estimate the fault length (670 km) and width (80 km) [Geology, March 1998; v. 26; no. 3; p. 199-202]. Finally, the relationship ($M = \mu UA$) between moment magnitude, M, the shear modulus, μ ($= 4.5 \times 10^{20}$ N/m^2), the average slip, U, and the fault area, A, (670×80 km^2) was used to estimate the magnitude of the slip (20 m). Those fault-plane parameters were used in the elastic earthquake model to compute the static vertical sea-floor displacement. An identical displacement of the sea surface was then used as the initial condition for subsequent tsunami propagation computations (Figure 8-4).

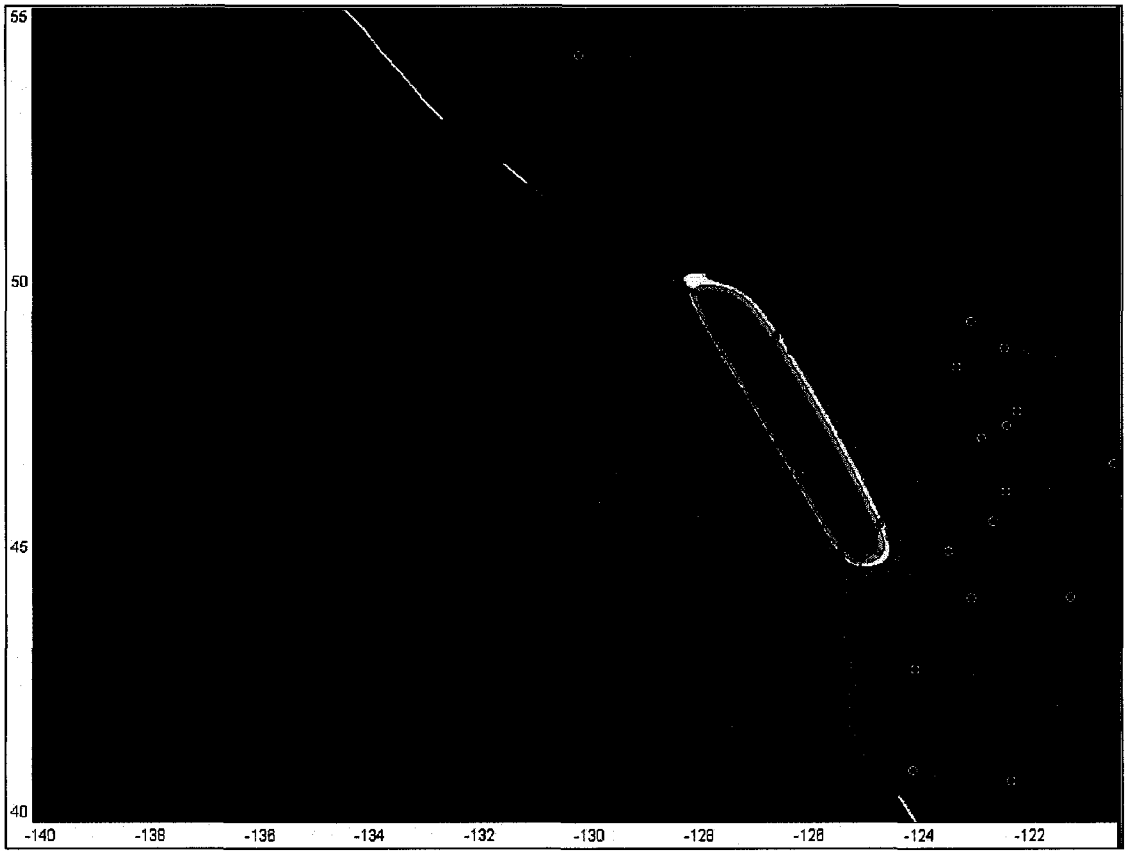

Figure 8-4: The calculated displacement of the submarine bottom by using Harvard solution (max. value ~ 9 m)

8.4. Tsunami travel time

The same models were used here as in the Indian Ocean tsunami simulation. One minute bathymetry (about 1.852 km along a meridian, generally known as ETOPO1) available from the NOAA-NGDC website (http://www.bodc.ac.uk/data/online_delivery/gebco/) in the area of 40^0N~55^0N from south to north with a total number of 1162 grids, 140^0W~120^0W from west to east with a total number of 901 grids was used to reflect the ocean bottom features. For a typical 4-km water depth, the wave speed is approximately 200 m/s or 720 km/hr. For the case of the present simulation, it takes around 1 hour and 20 minutes for the first tsunami wave to arrive at the mouth of the Juan de Fuca Strait, as shown in Fig. 8-5.

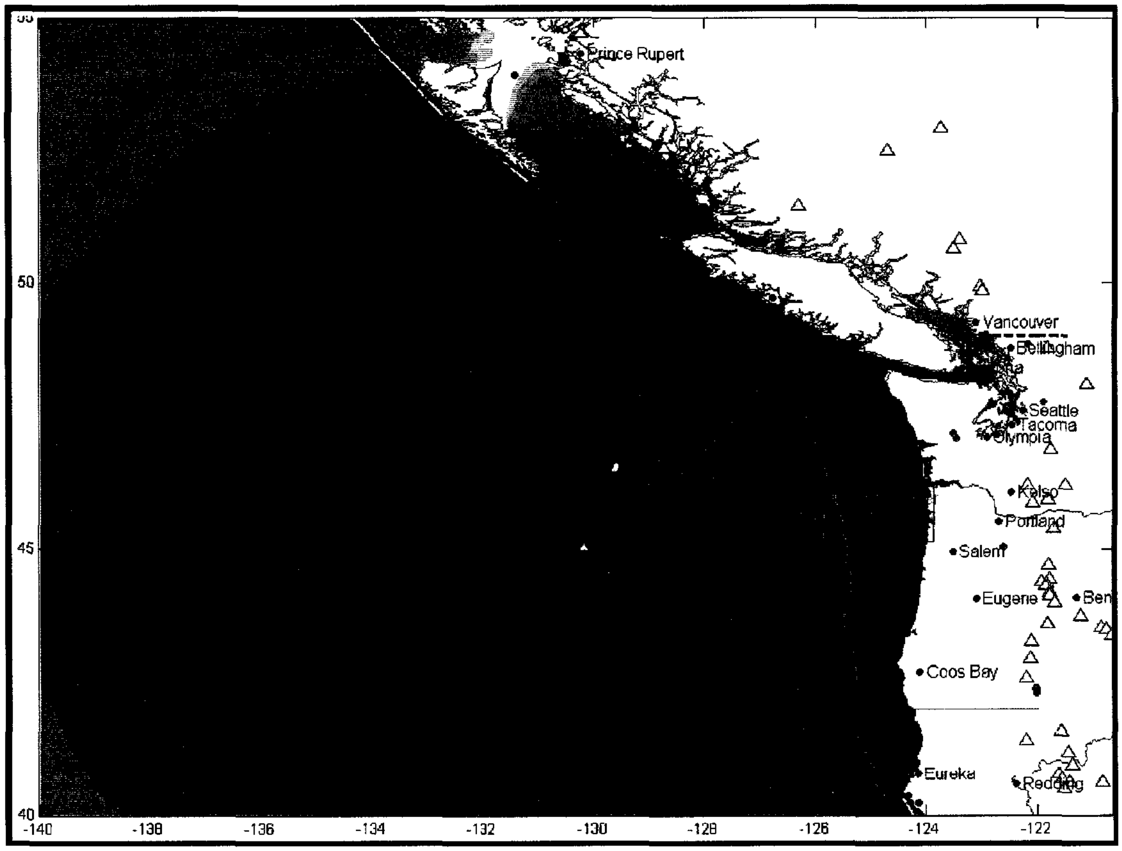

Figure 8-5: Computed tsunami travel time for the Cascadia tsunami

8.5. Tsunami propagation

The output of a submarine seismic source model was used as an initial condition for ocean surface displacement, which then propagates away from the source. The calculation domain is the same as above; the time step for computation is 1 second, small enough to satisfy the stability criterion of the finite difference computation. The simulation time is 2 hours and 30 minutes on a desktop computer (2.0GB RAM and Athlon XP 2600+ CPU). The computed tsunami amplitudes vary with the azimuth on its path across the Pacific Ocean. Computed tsunami amplitudes are large in an arc stretching westward, between Hawaii and Kamchatka and are the largest along a line pointing toward Midway Islands (Figure 8-3). The eastward wave moves towards North America and its continental shelf. The estimates of maximum wave height near Vancouver Island coast and Esquimalt Harbour, inside the Juan de Fuca Strait are as high as 25 m (Figure 8-6).

Maximum Amplitude

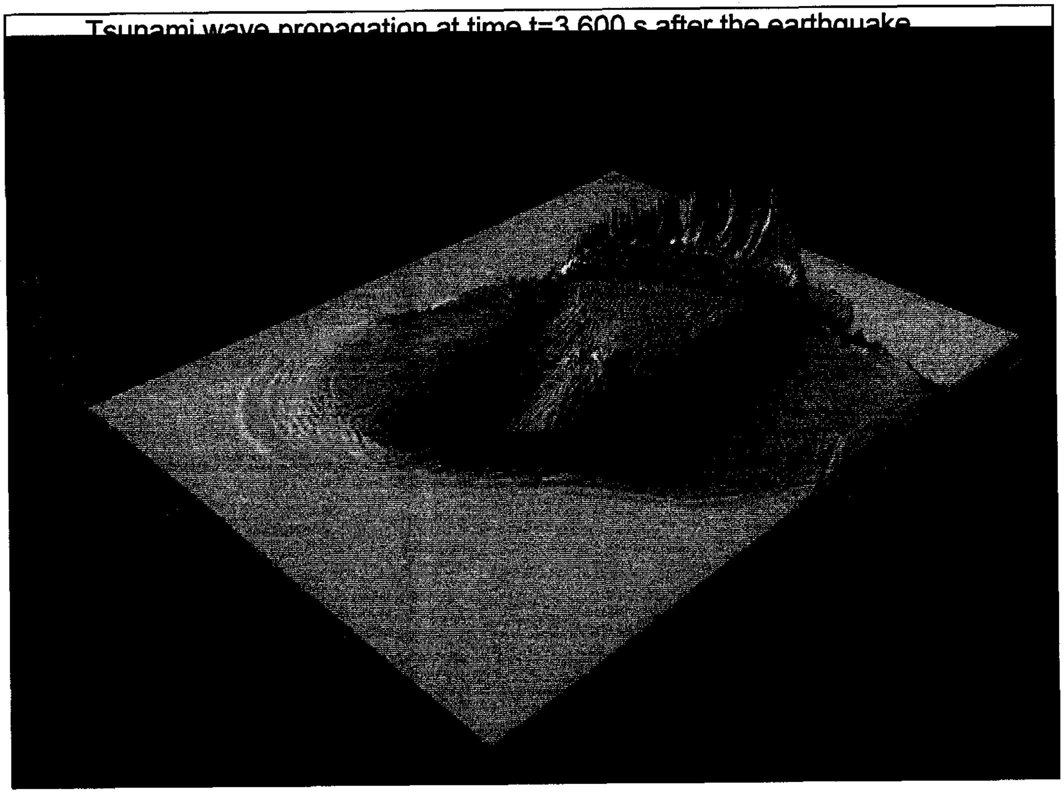

Surface Elevation

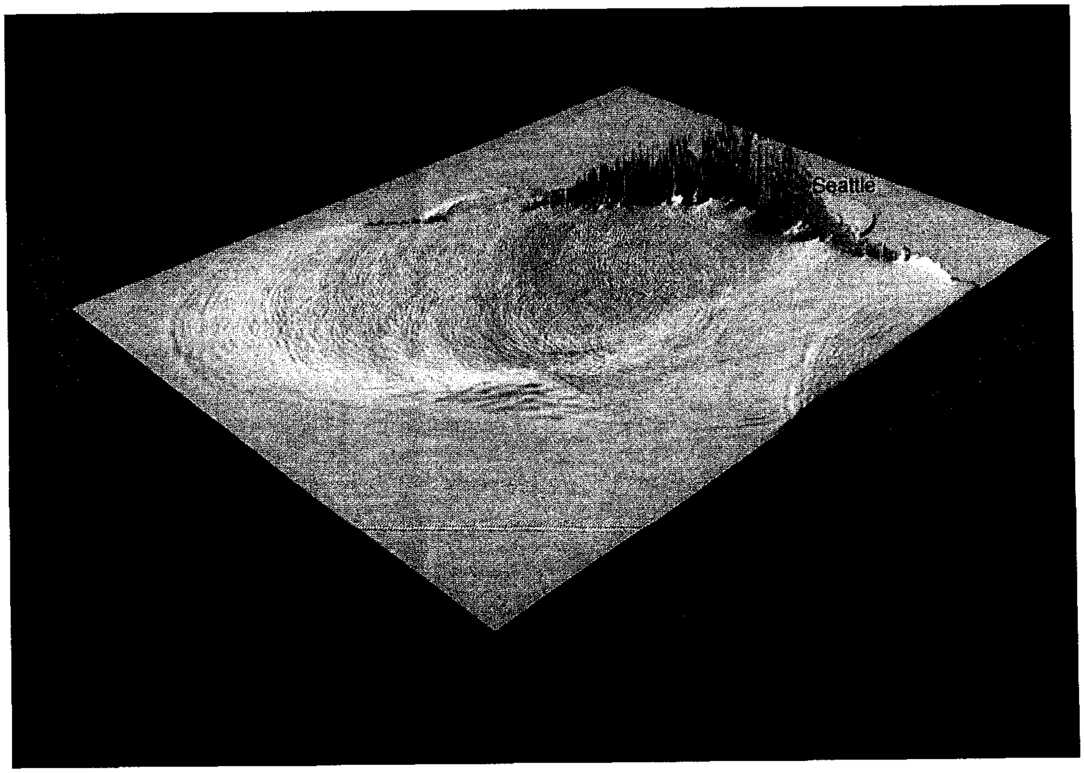

Figure 8-6: Maximum tsunami amplitudes and surface displacement (m)

Figure A-8 lists the ocean surface elevation and maximum wave amplitude of the Cascadia Fault tsunami at different time steps (t=500s, 1000s, 1500s, 2000s and 2500s) after earthquake occurrence.

8.6. Summaries of the Cascadia fault tsunami

This scenario focuses on the investigation of the tsunami risk for western Canada. Several conclusions presented below are drawn based on the results of the current investigation.

a. The analysis of the possible risk for an earthquake-generated tsunami in the near future along the Canadian coastline indicates that the threat of a potential tsunami is real and that this threat is particularly high for case of the western Canadian seaboard.

b. Because of its low population density, at present, there is no immediate priority for a tsunami early warning system for Arctic Canada. The Pacific tsunami warning system is in existence since 1948 and functions reasonably well from a scientific point of view. As for the warning aspects for the Pacific coast of Canada, the logistics are relatively simple, because only the federal government and the province of British Columbia are involved.

c. The analysis of the numerical modeling of a tsunami which could possibly occur in the near future as a result of an earthquake originating in the Cascadia fault, reveals the fact that extensive regions along the Canadian western seaboard would be affected and that the extent of the coastal flooding would be significant for the low-lying areas.

d. The travel time of a tsunami wave generated in the region of the Cascadia fault to the mouth of the Juan de Fuca Strait is around 1 hour and 20 minutes. This is a critical element not only for the early activation of the warning system (already in place in Pacific), but also for the implementation of mitigation measures needed for this region. In the case of a short warning time, the present system may be not effective for a local, Cascadia fault-induced tsunami.

e. The calculated maximum coastal run-up values indicate that, particularly for the low-lying regions of Vancouver, the extent of the coastal inundation and hazards associated with it may be significantly high.

f. More work needs to be done towards identifying the flood-prone areas and towards establishing the extent of the possible flooding zones for the purpose of preparing and implementing emergency measures and plans.

g. The numerical model needs to be improved in order to account for other phenomena not currently accounted for such as diffraction and, in the region very close to the shoreline, the increased bottom friction which accounts for wave damping and energy dissipation.

CHAPTER 3

DISCUSSION AND ANALYSES

9.1. Discussion

Tsunami modeling has traditionally been undertaken using the shallow water wave equations, which are non-frequency, dispersive long wave equations. Nowadays, with requirements for more advanced and accurate simulations, with a finer grid size better results would be possible. Also, diffraction and refraction, as well as wave dispersion, must be taken into account.

During propagation of deep water waves, propagation of an undular bores in shallow water, and propagation of edge waves along the coastline (Liu et al., 1998), dispersive effects are important. The recorded and observed tsunami waves originated by the earthquake of 26 December, 2004, showed complicated temporal and spatial structure. Analysis of recorded data demonstrated that the tsunami waves propagating south-westward across the Indian Ocean two hours after the main shock were noticeably dispersive (Kulikov *et al.*, 2005). Figure 9-1 shows the tsunami signal two hours after the main shock. According to this figure, most of the energy was associated with a wave period of about 50-60 min. The spatial extent of the wave field is remarkable. The bottom panel presents results from frequency band-pass analysis of the tsunami signal and clearly indicates the spatial shift (time delay) of the short wave components compared to the leading wavefront. Because shorter wave are dispersive and cannot propagate long distance, trans-ocean tsunami waves are mainly long period waves. Dispersion effects can be significant for amplitude estimation in transoceanic tsunami propagation. This brings into question the accuracy of the models used for numerical simulation of tsunamis. Usually, tsunami models are based on the shallow water approximation which ignores the effect of linear wave dispersion. As the initial wave propagates, separation of the wave into spectral components with different frequencies and amplitudes occurs. Thus, the leading wave is followed by a train of waves formed in its tail. In coastal regions this train of waves interacts with the leading wave's run-up, drawdown and reflection from shelf or land, introducing strong modification to leading wave effects. Often coasts are located in low-lying and flat regions that together with natural and man-made obstacles make the retreat of the flood caused by the first tsunami wave very slow. In this situation, subsequent waves entering shallow water, often ride over a region already flooded by the first wave, allowing these waves to impinge on structures, often with higher sea level and speed.

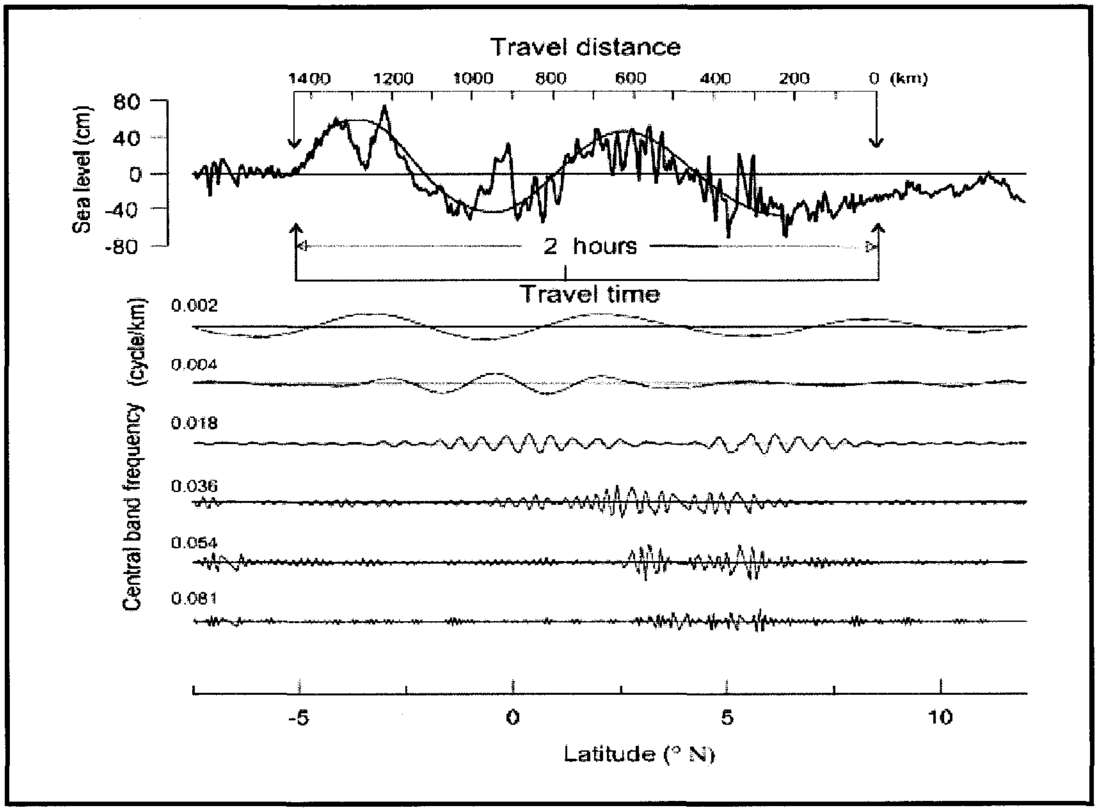

Figure 9-1: Tsunami wave frequency distribution (Kulikov *et al.*, 2006)

The presence of frequency dispersion in tsunami numerical modeling is important for the case of short wave propagation into relatively deep water, and allows for the mechanism of wave crests splitting during wave propagation over shallow bathymetry. Being a forced wave that depends on the characteristics of the disturbing force, a tsunami wave does not behave exactly as a long wave or a short wave, but behaves as an inter-mediate wave which is modified and transformed by the oceanic and seabed properties, as it travels away from the generation area. Explaining these phenomena is not simple, since a train of waves approaching a particular coastal region, in addition to transformation, may have experienced dispersion effects, and could be composed of a combination of waves coming from different parts of the source, or it may be that these waves have been diverted by the ocean bathymetry or transformed by a submerged bar. So the difficulty in correctly simulating tsunamis lies in the fact that they are forced quasi-infra-gravity waves, whose characteristic length and period occur in between short gravity wind-waves and long-gravity waves, such as tides or storm surges. Therefore, they can not be fully described by conventional long wave models.

9.2. Critical analysis

A traditional method to calculate the inundation area is by simulating wave run-up near the shoreline. Then, one would translate the wave run-up into inundation area; while totally ignoring the effect of inundation velocity on the flooding zone. The shallow water, long wave theory, is inadequate to accurately describe the observed coastal flooding and resolve local effects of topography or friction at different locations, regardless of the grid size. The flooding levels are strongly dependent upon friction, which is the largest unknown factor in evaluating tsunami coastal flooding. Currently, only an upper limit on flooding can be obtained without a realistic friction model. The effects of bottom friction, trees, and buildings introduce a 5 to 25% uncertainty factor, a fact which demonstrates that the shallow water model is somewhat inadequate for computing coastal inundation. The interaction of the reflected first wave with the later waves often results in the second or third wave run-up being very different than the firstwave run-up. The highest crest in a series of tsunami waves is often not the first wave to arrive at the shore. Consequently, the behavior of a series of waves inside the inlets must be predicted, which demands, in turn, a realistic treatment of the boundary conditions, especially the reflection condition at the landward end. More accurate modeling of extreme water levels near inlet heads - that exhibit significant absorption of wave energy or flooding on dry ground - will require finer resolution bathymetry. The magnitude and direction of the wave depends upon both the bottom slope and the wave period. For higher period waves, the second wave is as much as a third larger than the first wave. Moreover, shallow water models are inadequate to describe the effect of underwater barriers on tsunami waves because the vertical component of velocity is a crucial feature of the flow in such cases. Since we assume that horizontal velocity is vertically uniform, and the flow is hydrostatic, when underwater barriers exist or the ratio of bottom slopes is less than 1 in 10, the assumption of a uniform velocity over depth is no longer valid. During propagation and inundation, non-uniform velocity profiles over depth are most often encountered when water waves propagate from deep to shallow water, so that they become significantly nonlinear.

The 2004 Indian Ocean tsunami modeling results obtained in this study have therefore significant error bars, similar to all the other similar studies in the literature including those documented in the monograph *Numerical Modeling of Water Waves (NMWW), CRC Press 2004.* The University of Hawaii team had to increase the source magnitude of the 1946 tsunami event from the observed 7.5 to 8.4 to obtain inundation similar to the observed ones. This means that they had to increase the magnitude by a factor of 9 to compensate for the numerous errors characteristic to all shallow water model calculations.

Another aspect is that, presently, all numerical models try to calculate the initial wave height and do not consider the initial wave current. In reality, the initial wave current is a very important factor for the tsunami impact, especially when the earthquake source is located in shallow waters or near a low-altitude coastal zone. From the tsunami generation mechanism, we already understand that only a slow earthquake can trigger a huge tsunami. While in our numerical modeling process, we assume that the earthquake is instantaneous, this simplification leads to a certain bias. The generation module should be improved to compensate for the above shortcomings. Also, due to lack of instrumentation for measuring currents during inundation, when a tsunami approaches the shoreline, numerical models simply calculate the relative tsunami run-up for specific locations and then convert it to the inundation distance, according to the ratio of the bottom slope. The amplification of the tsunami amplitude is mainly associated with strong amplification of tsunami currents. Nonlinear interaction between tides and tsunamis lead to smaller amplitudes than in the case of a linear superposition. The nonlinear interaction of tides with tsunami is important, as it generates stronger run-up and even stronger changes in tsunami currents. Thus, the resulting run-up ought to be calculated for the tsunami and tide propagating together. The contribution of the tide to tsunami run-up can be significant, especially during the high tidal phase.

NOAA has actively been developing a system of deep ocean pressure monitoring systems (Tsunameter system or DART buoys). These instruments have the potential to allow the rapid monitoring and evaluation of tsunamis, facilitating warnings and evacuation (Bernard *et al.*, 2005). This advance in instrumentation could lead to more timely and more accurate warnings and thus, save lives. The current state-of-the-art shallow-water wave models cannot predict tsunami inundation correctly, including extreme run-up, current velocities and overland flow.

Coastal inundation is correlated more with inundation velocities than with inundation heights, thereby providing one explanation why threshold-type modeling has substantially underpredicted coastal inundation in this and other recent events (Titov *et al.*, 2006). The only scientifically valid method available at present for the determination of tsunami inundation zones is to examine historical records such as those collected during the recent Indian Ocean.

CHAPTER *4*

CONCLUSIONS AND RECOMMENDATIONS

10.1. Summary and conclusions

Any numerical model is based upon certain assumptions, hypotheses and has certain limitations. The simplest case of tsunami wave simulations is the linear gravity wave theory (LGW), in which case the convective terms are neglected completely. The LGW model is valid when H/L, H/D, and L/D (H — wave height; L — wave length; D — water depth) are small, i.e. for waves of small amplitude and small wave length in deep water. Under the first assumption, they are modeled using the 'small amplitude wave theory', which is the infinitesimal wave approximation. For studying the effect of various wave length-to-depth ratios and the tsunami propagation for longer distance and times, the LGW model is generally used. Because nonlinear terms are important when the waves travel to the nearshore area, the analytical linear gravity wave model is inadequate to analyze wave run-ups and the associated coastal flooding.

The incompressible, nonlinear, shallow water, long wave code including the effects of friction and flooding has been used to model the development of a tsunami wave from an initial sea surface displacement, the propagation of a tsunami wave, and the resulting shoaling and flooding. If the tsunami period is large (15-60 min), the model can approximately describe initial tsunami wave propagation across deep ocean basins, but the numerical techniques cannot model tsunami inundation within an error factor of 2. A calculation from the source to run-up and flooding often has a factor of more than 10 to 15% error. Since we assume that water waves are nonlinear, incompressible and the flow is viscous, the long wave theory results in waves that become steeper as they move onshore, and which are too steep as they shoal and hence, break too early. This is called the "long wave paradox" and becomes more serious as the distance and time of computation increases. Thus, the MOST model has to have a single high friction factor to remain numerically stable so that the tsunami waves do not break too early.

All numerical models can simulate trans-ocean tsunami waves due to their longer wavelength and period. In terms of description of the tsunami wave properties, the shallow water code which use sinusoidal wave as initial source, results in a constant amplitude and velocity along with a small trailing wave with amplitude of less than 0.01 meter. The waves from the shallow water model do not disperse in the deep ocean, they shoal higher and steeper, and also they do not disperse as they run along the shallow area. ZUNI model, which used Stokes waves as initial source wave, considers dispersion and results in a 20% lower height than the reflected wave in the SWAN model. Also, the maximum run-up does not result from the shoaling of the first wave, but from the shoaling of the second or third wave which ride on the first wave. Such behavior has been observed in real tsunamis. When the ratio of wavelength to water depth is less than 10, neither LGW model, nor UAF, nor MOST model should be used for accurate modeling of tsunami inundation.

Further, the evaluation of tsunami water levels should also consider the nonlinear interaction with tides. Tidal forcing applied along the model boundary can be coupled with tsunami levels. Simulations can be phased to combine tidal high water with the tsunami crest elevations, providing thus an estimate of the maximum probable combined water level in a dynamically coupled calculation. The effects of varying tidal heights and currents were not considered here, but they are important and should be included in future numerical models and experiments. The tidal range in most of the Indian Ocean coastal communities is about 4 to 12m, making tides a significant contributor to wave amplitudes and currents.

In conclusion, the inherent complexity of the tsunami generation, propagation and inundation in a complex ocean environment can always hamper the highly sensitive tsunami numerical models. But as new knowledge and understanding resulting from the analysis of accurately collected data and interpretation becomes available, these should be used so that better inundation hazard maps will be developed. Accurate model predictions, especially with regards to wave amplitudes and phases, can lead to improved early warning systems.

10.2. Recommendations

As explained in the above paragraph, tsunami numerical modeling must attain the ability to resolve important wave propagation and transformation mechanisms such as refraction, diffraction, shoaling, partial reflection and transmission, back-scattering, frequency dispersion, non-hydrostatic pressure, non-uniform horizontal velocity, wave breaking and resonant wave-wave interaction.

Liu et al. (1995), and Titov and Synolakis (1998), among others, developed numerical models such as MOST for tsunami run-up on the basis of nonlinear shallow water equations. Those models were tested against physical experiments carried out by Briggs *et al.* (1994) on solitary wave run-up on a conical island. Although generally good agreement was obtained for the case of non-breaking waves, discrepancies exist in the case of breaking run-up, as shown by Liu et al. (1995) and Titov and Synolakis (1998). This calls for models to take non-hydrostatic pressure and wave breaking into account. Under the restriction of technology and computer resources, the UAF model incorporated wave dispersion and Coriolis force; succeeded in solving several numerical aspects so that the results more agree with observations. But it is still a shallow water based model; and assumes that the vertical velocity is uniform everywhere and the pressure is hydrostatic.

The basic theory of Boussinesq equations is to solve non-hydrostatic and damping questions including wave breaking and a non-uniform vertical velocity. Shallow water models are not applicable to combined wave-current interactions which are often encountered in nearshore regions. To enable the Boussinesq model to simulate the near shore area hydrodynamics, energy dissipation due to wave breaking is modeled by introducing an eddy viscosity term into the equations with the viscosity strongly localized on the front face of the breaking waves. The inclusion of the full nonlinearity of the Boussinesq model leads to a correct form of the Doppler shift in the equations when an ambient current is present. In other words, the new Boussinesq equations are suitable for modeling wave-current interactions, as shown by Kirby (1997). Boussinesq-type models which incorporate the momentum mixing due to wave breaking, are not only able to simulate nearshore wave transformation, but also capable of modeling wave-induced surf-zone currents, including rip currents and longshore currents. However, it is worth mentioning that not all of the Boussinesq type models reported in the literature are able to model wave-induced currents. To transform a Boussinesq wave model into a wave current model, two important issues must be resolved, besides the parameterization of energy dissipation owing to wave breaking and bottom friction. Firstly, the correct Doppler shift for wave-current interaction needs to be enforced (Yoon and Liu 1989; Chen *et al.,* 1998). Secondly, Boussinesq-type equations derived from the assumption of a potential flow have to consistently recover the vertical component of the vorticity in the momentum equations in order to ensure the transport of vertical vorticity associated with surf-zone currents. Wave run-up on the beach is simulated using permeable seabed techniques. Both breaking and run-up schemes are detailed by Chen *et al.* (1999b).

FUNWAVE, is a public domain higher–order Boussinesq wave model developed over the last ten years at the University of Delaware (Kennedy *et al.*, 2000). It is a fully Nonlinear Boussinesq model. The Boussinesq equation (including nonlinear advection term) is simplified as follows:

$$\frac{\partial u}{\partial t}+u\frac{\partial u}{\partial x}+v\frac{\partial u}{\partial y}+g\frac{\partial \zeta}{\partial x}+\frac{1}{\rho D}ru\sqrt{u^2+v^2}=\frac{\partial \psi}{\partial x} \tag{34}$$

$$\frac{\partial v}{\partial t}+u\frac{\partial v}{\partial x}+v\frac{\partial v}{\partial y}+g\frac{\partial \zeta}{\partial y}+\frac{1}{\rho D}rv\sqrt{u^2+v^2}=\frac{\partial \psi}{\partial y} \tag{35}$$

Where the potential function ψ is defined as

$$\psi=\frac{H^2}{3}\left(\frac{\partial^2 u}{\partial x\partial t}+\frac{\partial^2 v}{\partial y\partial t}\right) \tag{36}$$

Here ρ is the water density, u and v are vertically averaged velocity components along x and y directions respectively, H is the mean water depth, ζ is the sea level, $D=\zeta+H$ is the total depth, r is the friction coefficient, and g is the gravitational acceleration.

More detailed and expanded versions of the equations can be found in the link (source code can be downloaded): http://chinacat.coastal.udel.edu/~kirby/programs/funwave/funwave.html. The benefits of a Boussinesq wave propagation model over traditional nonlinear shallow water wave models is that the horizontal velocity over depth is no longer constrained to have a constant value, and vertical accelerations (i.e., non-hydrostatic pressures) are no longer neglected. Also it incorporates underlying unsteady flow generated by wave breaking. The wave breaking scheme gives better predictions than do non-dispersive models based on nonlinear shallow water equations reported in the literature. As a research trend, we should put more emphasis on improving the Boussinesq models so that the real hydrodynamic process can be reproduced in the near future.

10.3. Preparedness

Although the occurrence of an earthquake and ensuing tsunami cannot be prevented, the magnitude of catastrophic impacts in terms of loss of life and livelihood, the, destruction of property and the associated environmental damage can be kept within reasonable limits through an integrated approach to disaster management. Planning of disaster management encompasses four different, but related, aspects: mitigation or prevention, preparedness, response and recovery.

One effective method to get ready for a future tsunami attack is to protect the coast that has a high risk of tsunami destruction. This protection may come in many ways, from a combination of mangrove forests, buffer zones, sand dunes and, in very special circumstances, seashore protection such as a breakwaters or seawalls. These types of protections were built in some places along Japan's coastline. However, such physical constructions are very expensive. In addition, they also generate environmental problems. For instance, they create a gap between the ecosystem of the sea and of the land; and they may also be unappealing for the people who live along the coast. Therefore, vegetation belts for coastal protection are often preferable as a "soft" technique. Mangroves that have strong roots have been considered as the right choice to hold back a large wave, such as tsunamis. Research using analytic, numerical and also laboratory experiment has shown that mangroves have an optimal capacity to reduce the wave energy caused by a tsunami. The use of mangroves as a protection measure is effective in the long-term. It is relatively cheaper than building a seawall, so it is affordable for most of the developing countries. Furthermore, it also has many other functions, for example, as a great biota-breeding place, as a filter of seawater penetration, or as wild bird habitat. However mangroves forest vegetation requires protection from strong winds and wind generated waves. As a consequence, mangroves communities tend to located within sheltered coastal areas such as estuaries, embayment and offshore islands protected by reefs and shoals.

It is necessary that suitable long-term measures during the pre-tsunami period are initiated. This does not mean that constructing a protection wall is the only solution. The best way is to use a botanical shield planting of mangroves near the shore to help reduce the amplitude of tsunami waves. The mangrove is a combination of a grass and a type of bush. The mangrove plantation should be planted off shore. Another similar approach is to plant Casuarinas trees, Phoenix Paludosa (khajoor tree) or similar palm-type trees. These are known as sand binders, are very strong and don't break or burn easily. Planting of such trees in a few rows, parallel to the seashore, will help tremendously to reduce the tsunami effect on the shore. Once the botanical shield is planted, it will not need maintenance.

REFERENCES

Annunziato A., C. Best (2005), the tsunami event analyses and models; JRC Tsunami Model: http://tsunami.jrc.it/model; Joint research center, European commission, January 2005, 42 p.

Barman. R., Kumar B. P., Pandey P. C., and Dube S. K. (2006) tsunami travel time prediction using neural networks, *Geophysical Research.*

Bhaskaran P. K., Dube S. K., Murty T. S., Gangopadhyay A., Chaudhuri A. and Rao A. D. (2006) tsunami travel time atlas for the Indian Ocean, chapter 24, pp 273-292, in "the Indian Ocean tsuanmi" edited by Murty Tad, Aswathamarayama U. and Nirupama N., Taylor and Francis, London, P491.

Chittibabu P. and Murty T. S. (2006) numerical models for the Indian Ocean tsunami of 26th December, 2004: a brief review, chapter 15, pp 159-174, in "the Indian Ocean tsunami" edited by Tad Murty, U. Aswathanarayana and N. Nirupama, Taylor, and Francis, London, P491.

CASCADIA SEISMIC EXPERIMENT by University of PGC, SFU, JAMSTEC, UBC, and Dalhousie (2003), http://geophys.seos.uvic.ca/cassis/update.html;

Chang, S.E. (2003). Evaluating Disaster Mitigations: Methodology for Urban Infrastructure Systems. Natural Hazards Review, November 2003, 186-196.

Cherniawsky Josef Y., Titov, Vasily V., Wang, Kelin and Li, Jing-yang(2006), Numerical simulations of tsunami waves and currents for southern Vancouver Island from a Cascadian megathrust earthquake; http://www.pac.dfo-mpo.gc.ca/sci/osap/projects/tsunami/default_e.htm

Dunbar, D., P. Leblond and T. S. Murty. 1991. Evaluation of tsunami amplitudes for the Pacific Coast of Canada. Prog Oceanog. 26: 115-177.

EarthGuide (2002). Tectonic Plates. University of California. URL: http://earthguide.ucsd.edu/earthguide/maps/tectonicsio.html;

Fine Isaac V., Alexander B. Rabinovich, and Richard E. Thomson (2005), the dual source region for the 2004 Sumatra tsunami; *Geophysical Research Letters*, Vol. 32.

Geist E. L. Titov V. V., Areas D. Pollitz F. F and Bilek SL. (2007) Implications of the 26 December 2004 Sumatra- Andaman earthquake on tsunami forecast and assessment models for great subduction-zone earthquakes, *Bulletin of the Seismological Society of America*, Vol. 97, No. 1a, S249-S270.

Ghobarah, A., Saatcioglu, M. and Nistor, I., (2006). The impact of 26 December 2004 earthquake and tsunami on structures and infrastructure, *Journal of Engineering Structures*, Elsevier,Vol. 28, 312-326.

Grilli Stephan T., Mansour Ioualalen, Kirby James T. and Philip Watts (2007). Source constraints and Model simulation of the December 26, 2004 Indian Ocean Tsunami. *Journal of Waterways, Port, Ocean and Coastal Engineering.*

George David L. and Randall J. LeVeque (2006), Finite volume methods and adaptive refinement for global tsunami propagation and local inundation; *Science of Tsunami Hazards*, Vol. 24, No. 5, 319-327.

Goto, C. and N. Shuto. 1983. Numerical simulation of tsunami propagations and run-up. In Tsunami-Their Science and Engineering, edited by K. Iida and T. Iwasaki, pp 439-451. Tokyo: Terra Scientific Publ. Comp.

Horrillo J., Kowalik Z. and Shigihara Y. (2006a) wave dispersion study in the Indian Ocean tsunami of December 26, 2004, *Science of Tsunami Hazards*, Vol. 25, No. 1, P42-63.

Horrillo J., Kowalik Z. and Shigihara Y. (2006b) wave dispersion study in the Indian Ocean tsunami of December 26, 2004, *Marine Geodesy*, Vol. 29, P149-166.

Harlow, F. H. and J. E. Welch. 1965. Numerical Calculation of time-dependent viscous incompressible flow of fluid with a free surface. *The Physics of Fluids* 8:2182–2189.

Heinrich, P., F. Schindele and S. Guiborg. 1998. Modeling of the February 1996 Peruvian tsunami. *Geophysics Research Letter*. 25(14), 2687-2690.

Hirata, K. , K. Satake, Y. Tanioka, T. Kuragano, Y. Hasegawa, Y. Hayashi, and N. Hamada. 2005. The Indian Ocean Tsunami: Tsunami Source Model From Satellite Altimetry. Proceedings of the International Tsunami Symposium, edited by G.A. Papadopoulos and K. Satake, Chania Greece, pp 72-76.

Hyndman M.D., K. Wang and H. Dragert, Cascadia Megathrust Earthquake Potential: Constraints from Current Deformation and the Thermal Regime;
http://erp-web.er.usgs.gov/reports/abstract/1994/pn/g2487.htm;

Hebert H., Sladen A. and Schindele F. (2007) numerical modeling of the great 2004 Indian Ocean tsunami; *Bulletin of the Seismlogical Society of America,* Vol. 97, No. 1a, S208-S222.

Imamura, F., N. Shuto, and G. Goto. 1988. Numerical simulation of the transoceanic propagation of tsunamis. 18th Congress Asian and Pacific Regional Division, International Association for Hydraulic Research, Kyoto Japan 6: 265-272.

Imamura, F. and N. Shuto. 1989. Tsunami propagation simulation by use of numerical dispersion. International Symposium on Computational Fluid Dynamics P390-395.

Imamura, F., N. Shuto and C. Goto. 1990. Study on numerical simulation of the transoceanic propagation of tsunamis. Part 2, Characteristics of tsunami propagation over the Pcific Ocean. Zisin (J, Seismol. Soc. Japan), 43,389-402.

Imamura, F., Gica, E., Takahashi, T. and Shuto, N. (1995). "Numerical simulation of the 1992 Flores tsunami: interpretation of tsunami phenomena in Northeastern Flores island and damage at Babi island", Pure and Applied geophysics, Vol. 144, No. 3-4, P555-568.

Kowalik Zygmunt, William Knight, Tom Logan, Paul Whitmore (2005), the tsunami of 26 December 2004: Numerical modeling and energy considerations, *Science of Tsunami Hazards,* vol. 23, No. 2, P32-45.

Kowalik Zygmunt, William Knight, Tom Logan, Paul Whitmore (2005), Numerical modeling of the global tsunami: indonesian tsunami of 26 December 2004, *Science of Tsunami Hazards*, vol.

23, No. 1, P40-56.

Kowalik, Z. and Murty Tad (1993a), Numerical Modeling of Ocean Dynamics, Singapore: *World Scientific.*

Kowalik, Z. and Murty Tad (1993b), Numerical simulation of two-dimensional tsunami run-up, *Marine Geodesy*, Vol.16, P87-100.

Kumar B. P., Kumar R. R. Dube S. K., Murty T., Gangopdhyay A. Chaudhuri A. and Rao A. D. (2006) tsunami travel time computation and skill assessment for the 26th December, 2004 event in the Indian Ocean, *Coastal engineering Journal*, Vol. 48, No. 2, P147-166.

Kulikov, E. 2005. Dispersion of the Sumatra Tsunami Waves in the Indian Ocean detected by satellite altimetry.
http://www-sci.pac.dfompo.gc.ca/osap/projects/tsunami/documents/195610_0_merged_1107633516.pdf

Kawata, T. et XIV alia (2005). "Comprehensive analysis of the damage and its impact on coastal zones by the 2004 Indian Ocean tsunami disaster". Disaster prevention research institute, http://www.tsunami.civil.toholu.ac.jp/sumatra2004/report.html.

Lay, T., H. Kanamori, C. J. Ammon, M. Nettles, S. N. Ward, R. C. Aster, S. L. Beck, S. L. Bilek, M. R. Brudzinski, R. Butler, H. R. DeShon, G. Ekstrom, K. Satake, S. Sipkin. 2005. The Great Sumatra-Andaman Earthquake of 26 December 2004. *Science*, 308: 1127-1139.

Liu P.L.-F., Y. B. Cho, S. B. Yoon and S. N. Seo. 1995. Numerical simulation of the 1960 Chilean tsunami propagation and inundation at Hilo, Hawaii. In Tsunami Progress in Prediction, Disaster Prevention and Warning, edited by Y. Tsuchiya and N. Shuto. Netherlands: Kluwer Academic Publisher.

Murty, T., Rao, A.D, Nirupama, N., and Nistor, I. (2006b), Tsunami warning systems for the hyperbolic (Pacific), parabolic (Atlantic) and elliptic (Indian) oceans, *Journal of Industry Geophysical Union*, Vol. 10, No. 2, P69-78.

Murty, T., Rao, A.D., Nirupama, N., and Nistor, I. (2006a). Numerical modelling concepts for tsunami warning systems, *Current Science*, Vol. 90, No. 8, 1073-1081.

Murty, T., Nirupama, N., Nistor, I. and Rao, A.D. (2005). Conceptual differences between the Pacific, Atlantic and Arctic tsunamis warning systems for Canada, *Science of Tsunami Hazards*, Vol. 23, No. 3, P39-51.

Murty, T., Nirupama, N., Nistor I. and Hamdi, S. (2006) Why the Atlantic cannot generally generate trans-oceanic tsunamis. *ISET Journal of earthquake technology.* Vol. 42, No. 4, 130-155.

Mader, Charles L.(2004), *Numerical Modeling of Water Waves*; second edition; CRC Press.

Madsen, P. A., and H. A. Schaffer. 1999. A review of Boussinesq-type equations for surface gravity waves. In Advances in Coastal and Ocean Engineering, edited by P. L.-F. Liu, vol. 5, pp 1-94. Singapore: *World Scientific.*

Nichols, B. D., C. W. Hirt and R. S. Hotchkiss. 1980. SOLA-VOF: A Solution Algorithm for Transient Fluid Flow with multiple Free Boundaries. LA-8355, Los Alamos National Laboratory.

Nirupama, N., Murty, T., Nistor, I. and Rao, A.D. (2006). Persistent high water levels around Andaman and Nicobar Islands following the 26 December 2004 tsunami, *Science of Tsunami Hazards*, Vol. 24, No. 3, 183-193.

Nirupama, N., Murty, T., Nistor, I. and Rao, A.D. (2006). The Energetics of the Tsunami of 26 December 2004 in the Indian Ocean: A Brief Review, *Marine Geodesy Journal*, Taylor and Francis Group, London, Vol. 29, No. 1, 13-42.

Nistor I., Murty T.S., N. Nirupama, and S. Hamdi (2006). Far-Field Dispersion Characteristics of the Tsunami of 26th December 2004, *ISET Journal of earthquake technology.*

Numerical Modeling of the 1964 Alaska Tsunami; Web project by Elena Suleimani, PHYS-645; http://ffden-2.phys.uaf.edu/645fall2003_web.dir/elena_suleimani/propagation.html;

Okada, Y. 1985. Surface deformation due to shear and tensile faults in a half-space. *Bulletin of the Seismological Society of America* 75: 1135-1154.

Ortiz, M., E. Gómez-Reyes, H.S. Vélez-Muñoz. 2001. A fast preliminary estimation model for transoceanic tsunami propagation. ITS 2000 Proceedings 723-739.

Pararas-Carayannis, G. (2006a), Alexander the Great – Impact of the 325 B.C, Tsunami in the North Arabian Sea upon his Fleet. http://drgeorgepc.com/Tsunami325BCIndiaAlexander.html;

Pararas-Carayannis, G. (2006b), The earthquake and tsunami of 28 November 1945 in Southern Pakistan. http://drgeorgepc.com/Tsunami1945Pakistan.html;

Puspito N. T. and Gunawan I. (2005) tsunami sources in the Sumatra region, Indonesia and simulation of the 26th December, 2004 Aceh tsunami, *ISET Journal of earthquake technology*, pp. 459, Vol. 42, No. 4, 111-125.

Parsons Tom, Anne M., James H., Kate Miller, Fiona Kilride, Ray E. Wells, Michael A. Fisher, Ernst Flueh, Uri S. and Nikolas I. (1998): A new view into the Cascadia subduction zone and volcanic arc: Implications for earthquake hazards along the Washington margin.

Rivera Paul C. (2006), Modeling the Asian tsunami evolution and propagation with a new generation and a non-linear dispersive wave model; *Science of Tsunami Hazards*, Vol. 25, No. 1, P18-33.

Santek, D. A. and Winguth A. (2007). A satellite view of internal waves induced by the Indian Ocean tsunami. *The International Journal of Remote Sensing.*

Sato, S. 1996. Numerical simulation of 1993 southwest Hokkaido earthquake tsunami around Okushiri Island. *Journal of Waterway, Port, Coastal and Ocean Engineering* 122 (5): 209-215.

Satake, K., Wang K, and Atwater, B. F., (2003), Fault slip and seismic moment of the 1700 Cascadia earthquake inferred from Japanese tsunami descriptions, Journal of Geophysics Research, 108 (B11);

Titov Vasily (2007). The global reach of the 26 December 2004 Sumatra tsunami. *Science*, Vol. 309, 2045.

Watts, P., Ioualalen, M., Grilli, S., Shi, F., and Kirby, J. T. 2005. Numerical simulation of the December 26, 2004 Indian Ocean tsunami using high-order Boussinesq model, Fifth International Symposium. WAVES 2005, July, 2005, Madrid Spain, 10pp.

Walker, D.A. (2005), Critical Evaluations for the State of Hawaii Subsequent to the December 26, 2004 Asian Tsunami. *Science of Tsunami Hazards*, Vol. 23, No. 1, 17-24.

Xie Jinsong, Nistor Ioan, Murty Tad and Shukla T. (2007), Numerical modeling of the 2004 Indian Ocean tsunami — a review, *International Journal of Ecology & Development,* the special issue of the Mathematical Modeling of Earth System Sciences. (Accepted)

Xie Jinsong, Nistor Ioan, Murty Tad (2007), Numerical modeling of the 2004 Indian Ocean tsunami, *Science of Tsunami Hazards*.(Accepted)

Xie Jinsong, Nistor I., Murty Tad (2007), Tsunami risk for western Canada and numerical modeling of the Cascadia fault tsunami, *18th Canadian Hydrotechnical Conference & Symposium,* Winnipeg, Manitoba, August 22-24th, 2007.

Yalciner A.C., Ghazali N.H., Wahab A.K.A. (2005a). "December 26, 2004 indian ocean tsunami field survey (july, 09-10, 2005) at north west peninsular Malaysia coast, penang and langkawa islands." http://yalciner.ce.metu.edu.tr/malaysia-survey.

Yalciner A.C., Perincek D., Ersoy S., Presateya G., Hidayat R., McAdoo B., (2005b). "Report on December 26, 2004, Indian Ocean tsunami, field survey on Jan 21-31 at North of Sumatra", by ITST of UNESCO IOC. http://yalciner.ce.metu.edu.tr/sumatra/survey.

Yamada F., Fernandez, H., Goff J., Higman B. and B. Jaffe (2005). "An overview of the ITST expedition to Sri Lanka". In proc. 5th intl. on Ocean Wave Meas. And Analysis (waves 2005, Madrid, Spain, July 2005), ASCE Publish, paper 217.

APPENDIX:

Figure A—1: Soil erosion and structural damage (Saatcioglu *et al.* & Nistor *et al.*, 2005).

Figure A–2: Views of the coastal areas in the Takua Pa district after the 2004 tsunami (Thanawood *et al.*, 2006).

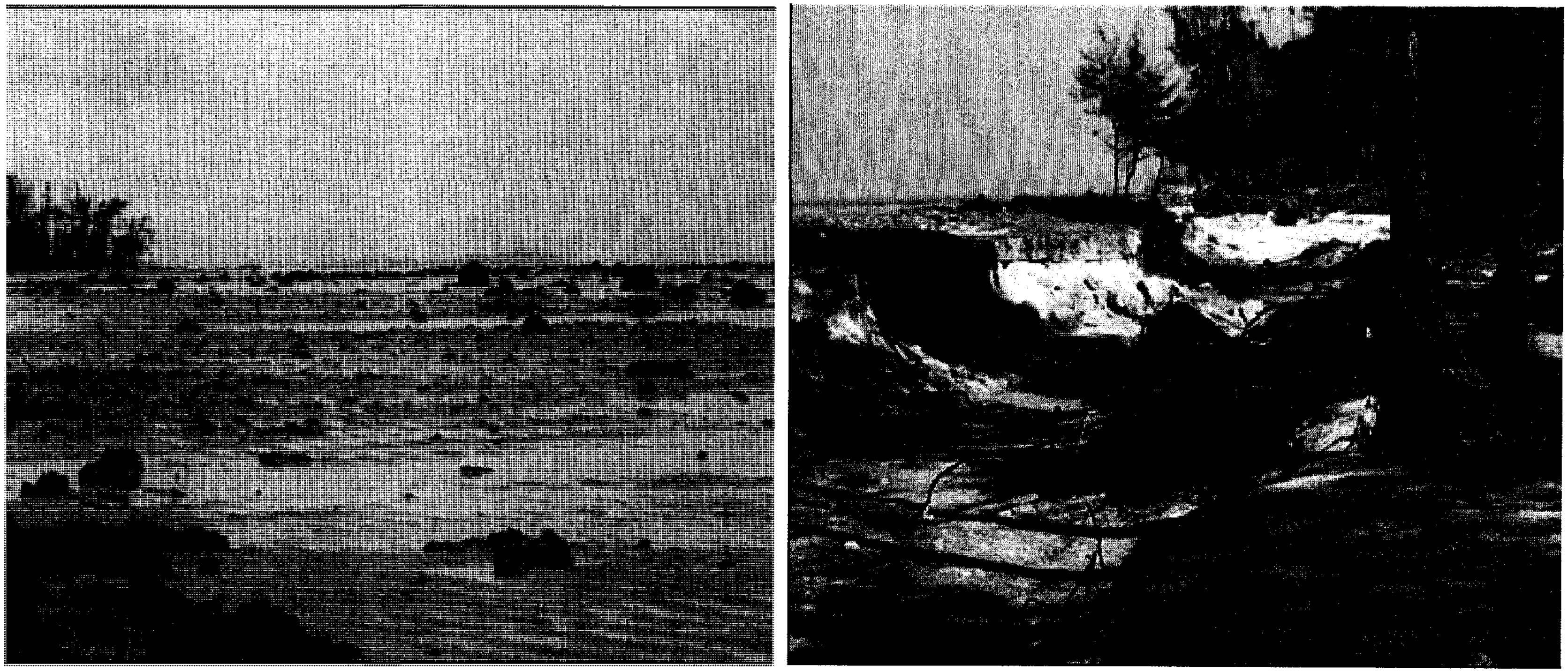

Figure A—3: 3-D Indian Ocean bathymetry and topography (shallow ocean bottom ridge).

Figure A—4: The computational domain for the 2004 Indian Ocean tsunami; the dots show the tide gauge location around the Indian Ocean.

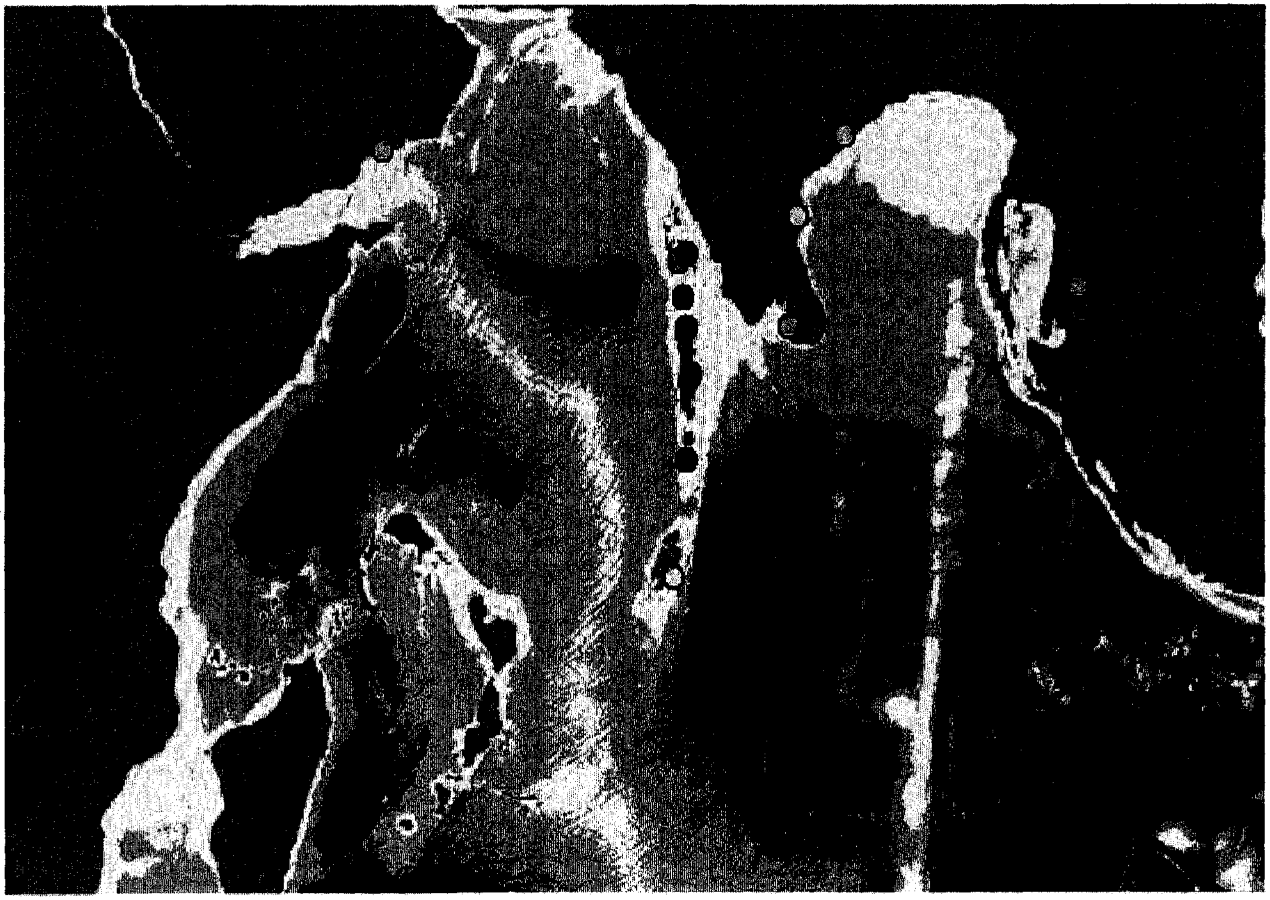

Figure A-5: Nested-grid schemes

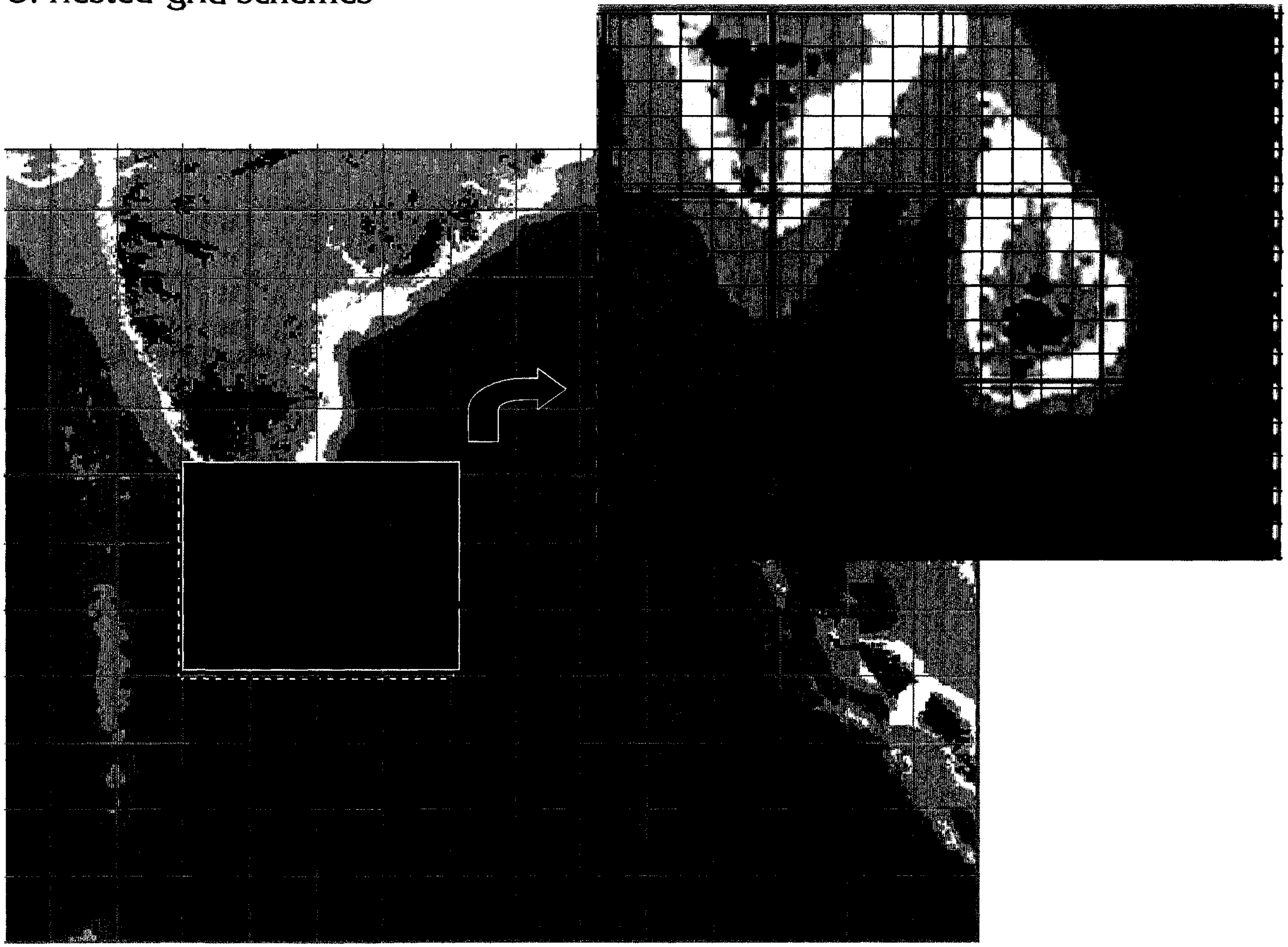

Figure A—6: The ocean surface elevation and maximum wave amplitude of the 2004 Indian Ocean tsunami at different times (t=0s, 1500s, 3000s, 6000s, 9000s, 12000s, and 15000s) after earthquake occurrence.

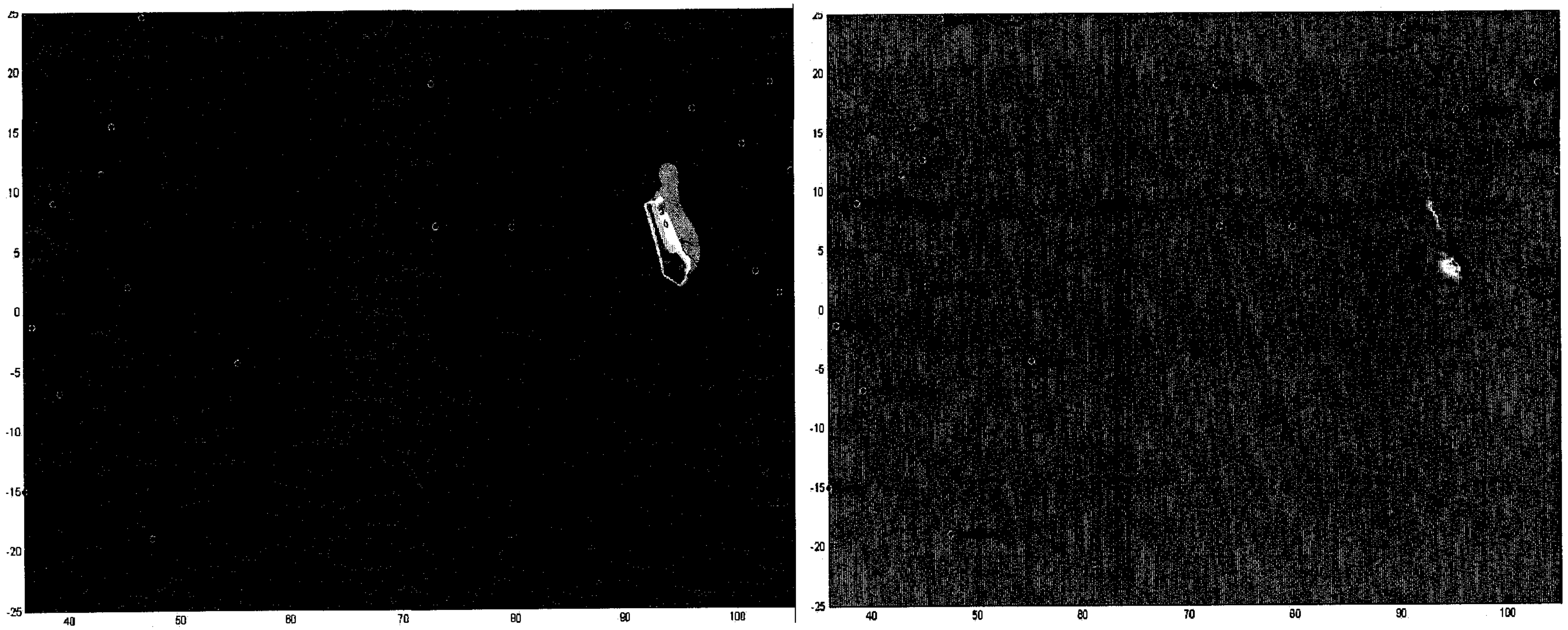

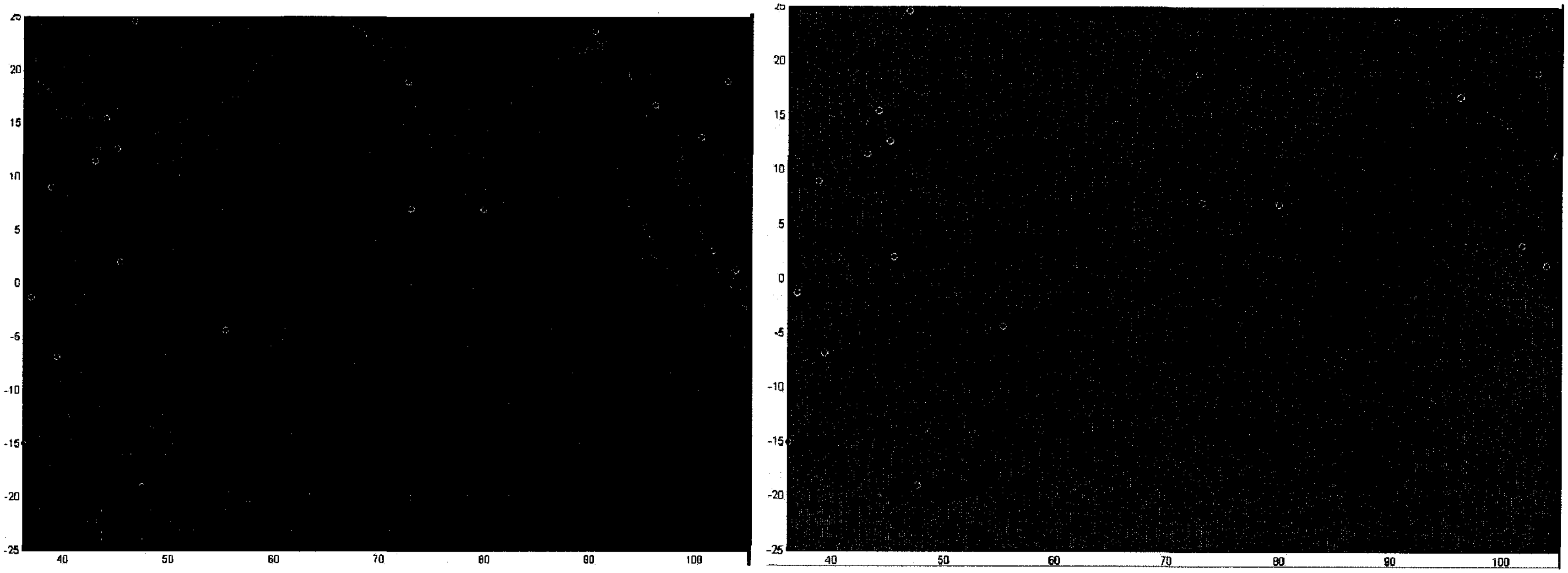
25
20
15
10
5
0
-5
-10
-15
-20
-25
40
50
60
70
80
90
100
25
20
15
10
5
0
-5
-10
-15
-20
-25
40
50
60
70
80
90
100

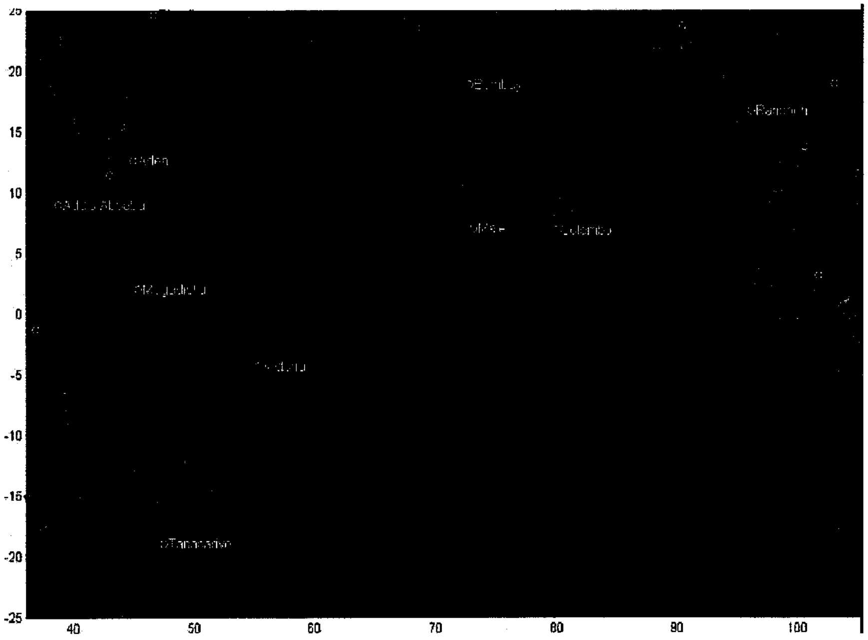

25
20
15
10
5
0
-5
-10
-15
-20
-25
40
50
60
70
80
90
100
Aden
Tananarive

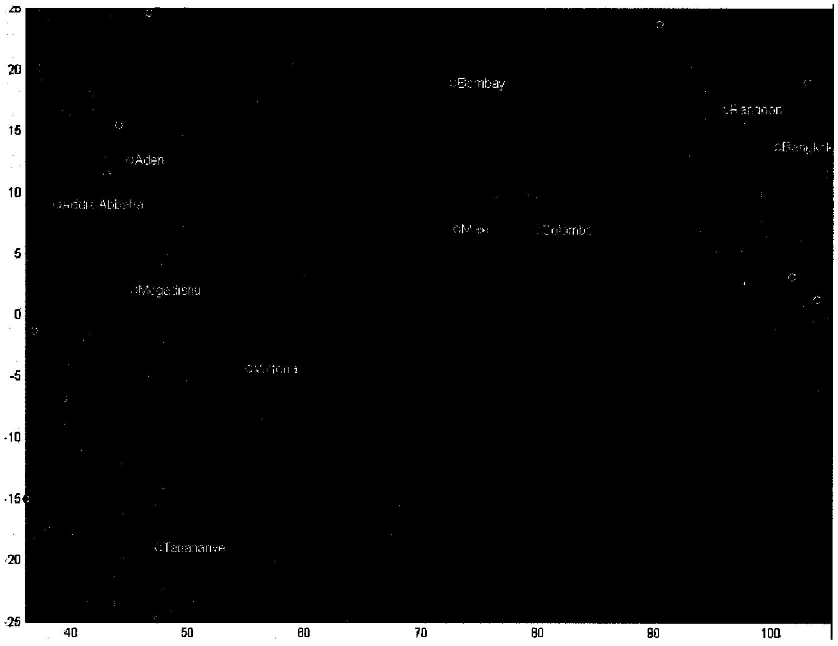

25
20
15
10
5
0
-5
-10
-15
-20
-25
40
50
60
70
80
90
100
Bombay
Rangoon
Bangkok
Aden
Addis Abeba
Male
Colombo
Mogadishu
Victoria
Tananarive

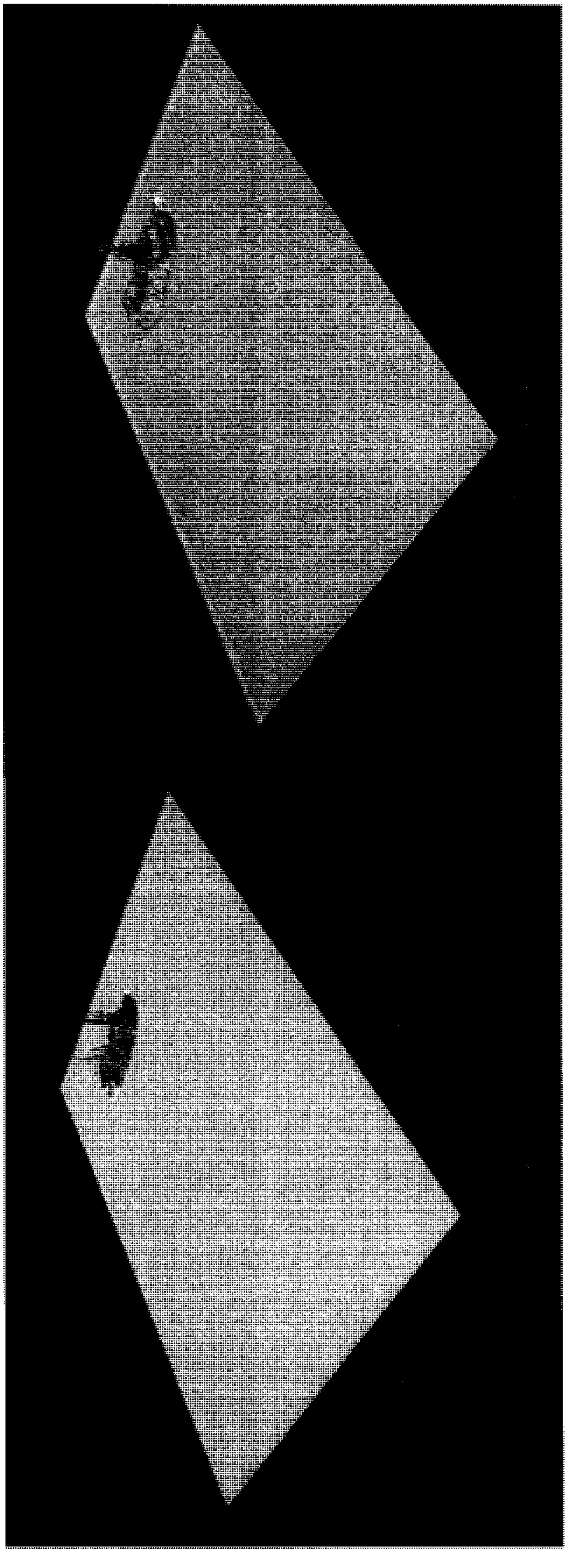

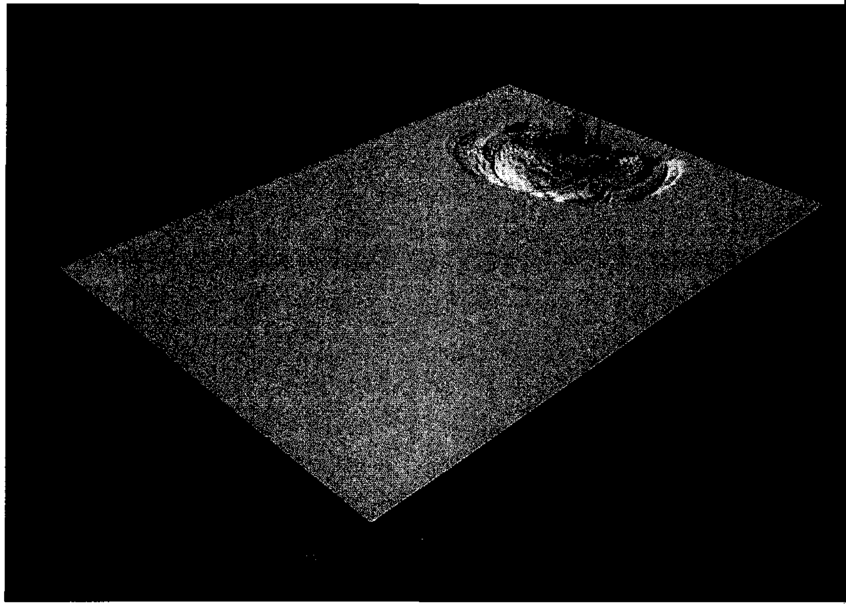

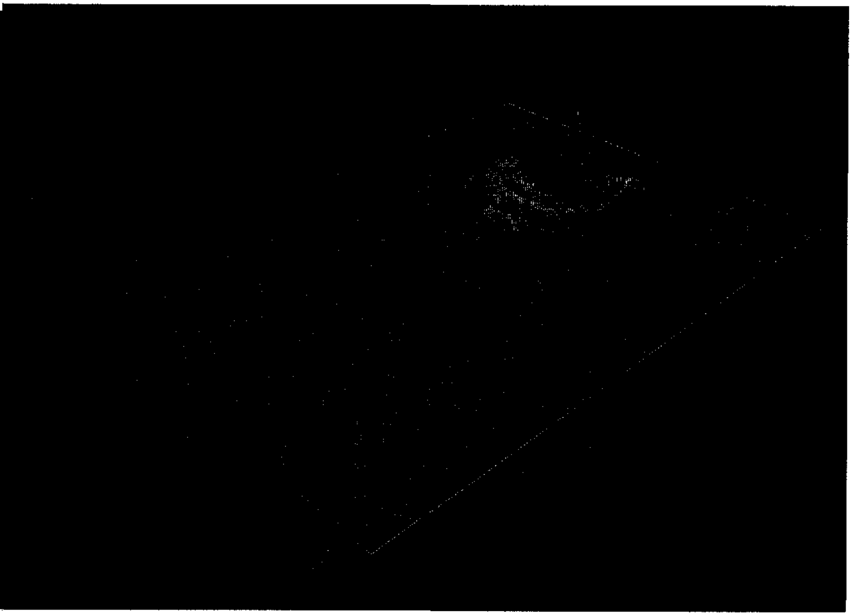

Figure A—7: The snapshots of surface elevations and maximum wave heights of November 28, 1945 MSZ tsunami at different times (t=500s, 1000s, 2000s, 3000s, 4000s, 5000s, 6000s, 7000s and 8000s) after earthquake occurrence.

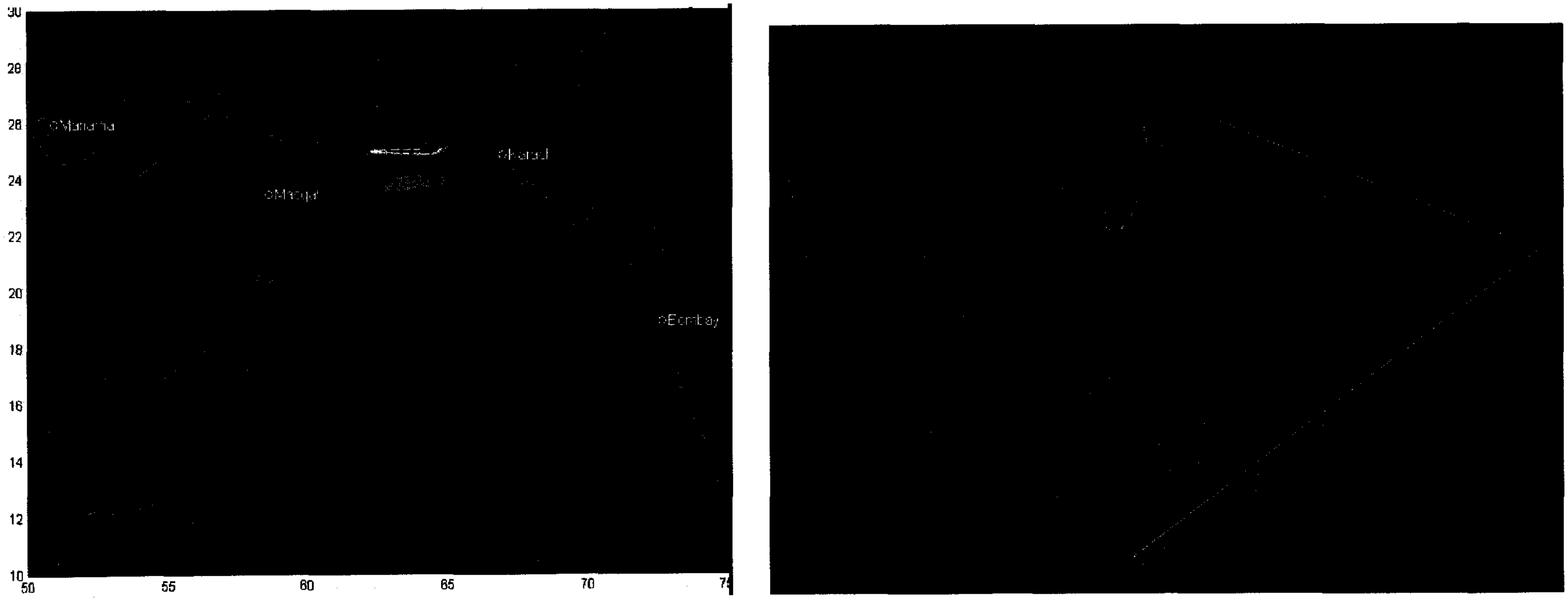

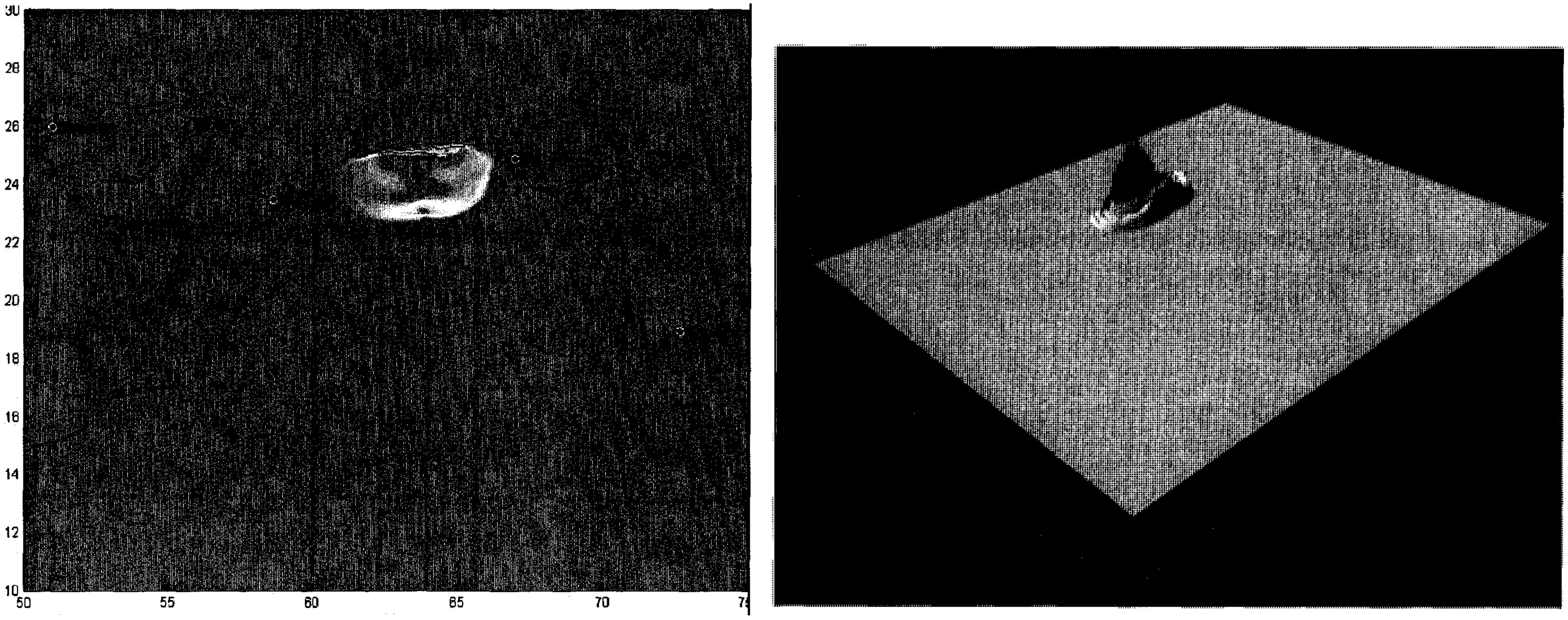
30
28
26
24
22
20
18
16
14
12
10
50
55
60
65
70
7

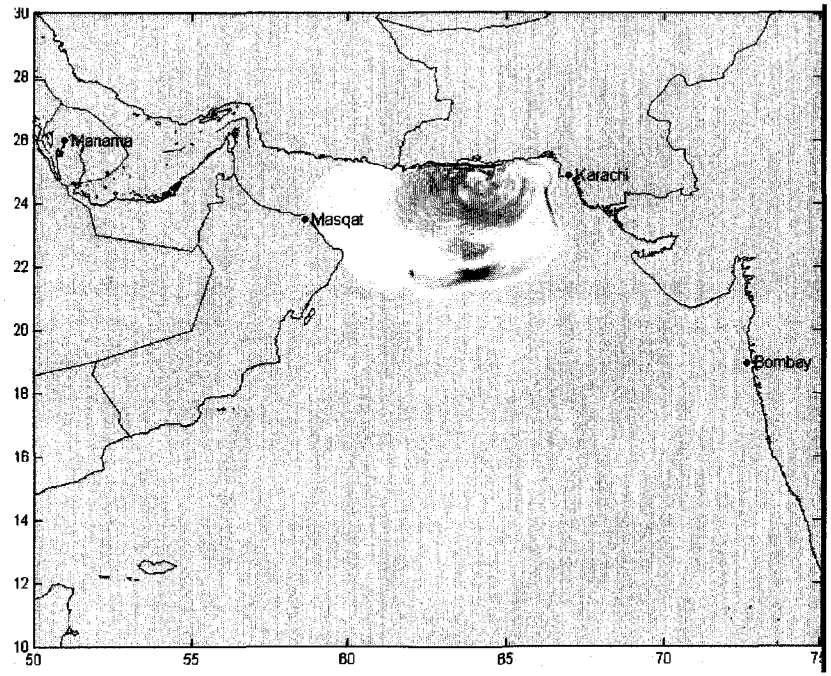
30
28
26
24
22
20
18
16
14
12
10
50
55
60
65
70
Manama
Masqat
Karachi
Bombay

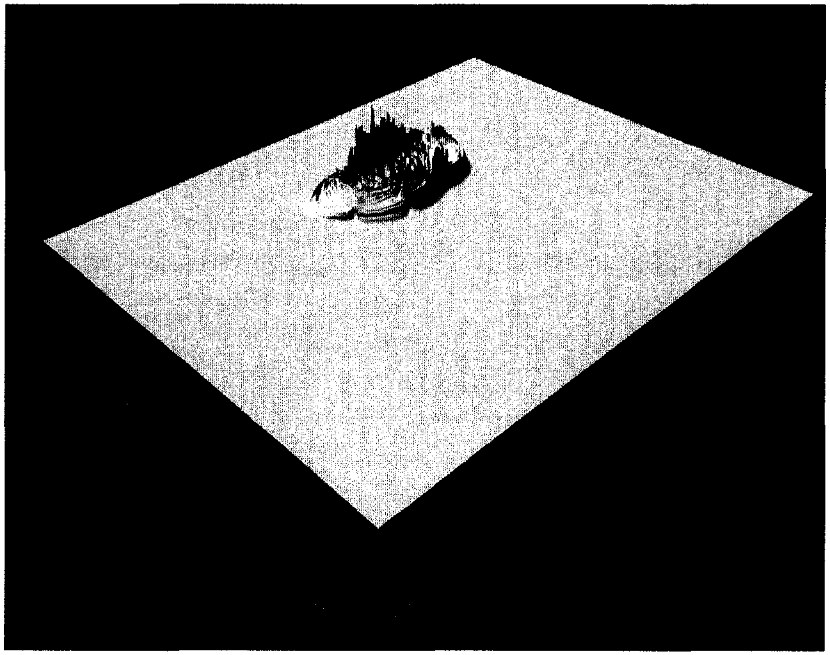

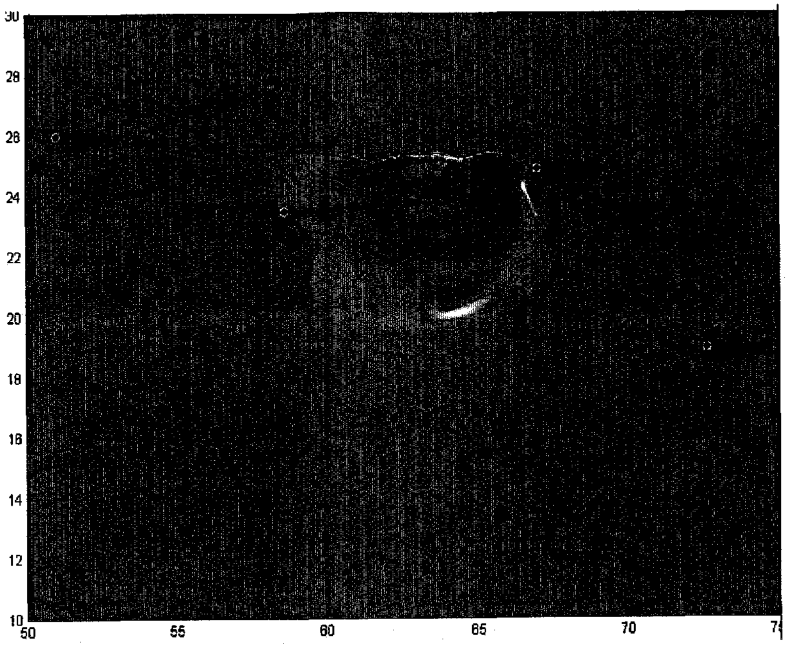
30
28
26
24
22
20
18
16
14
12
10
50
55
60
65
70
7

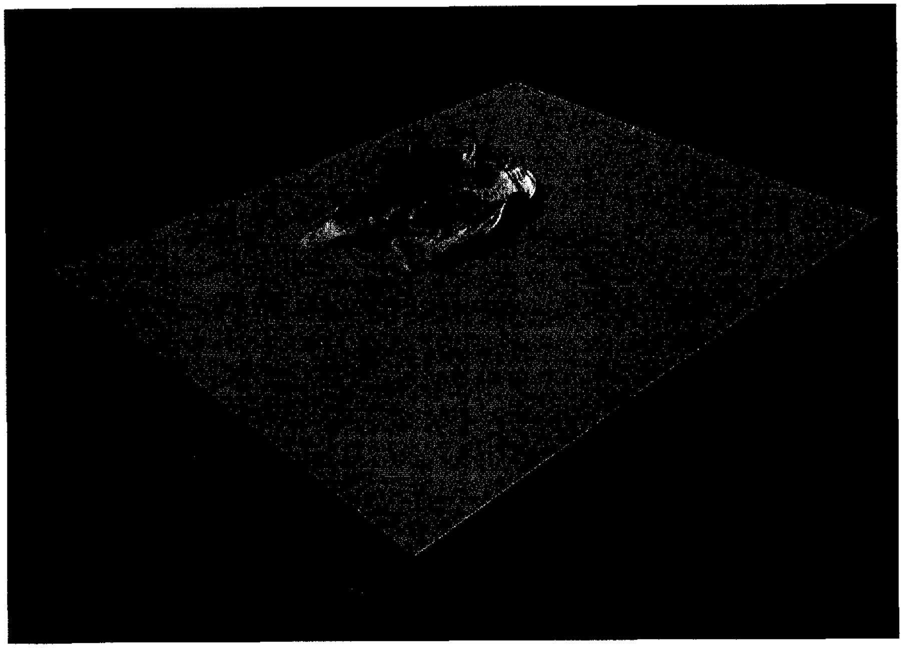

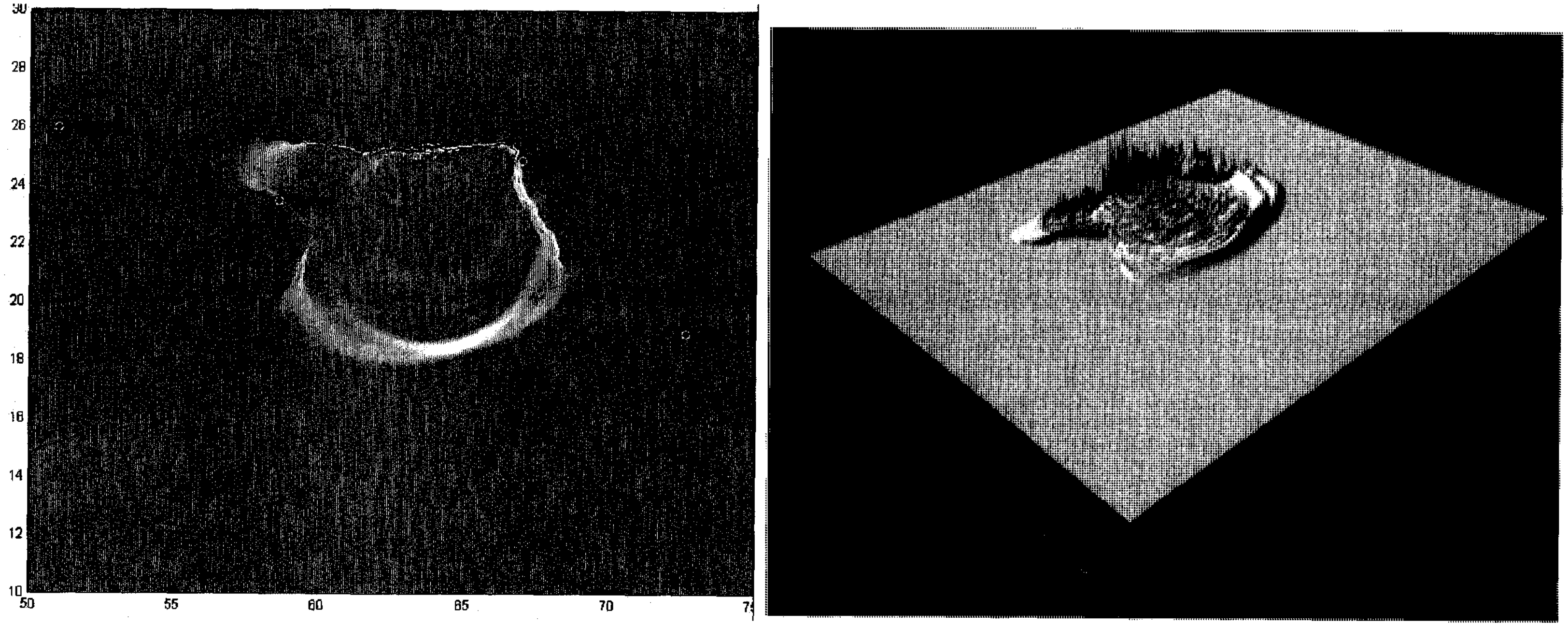
30
28
26
24
22
20
18
16
14
12
10
50
55
60
65
70

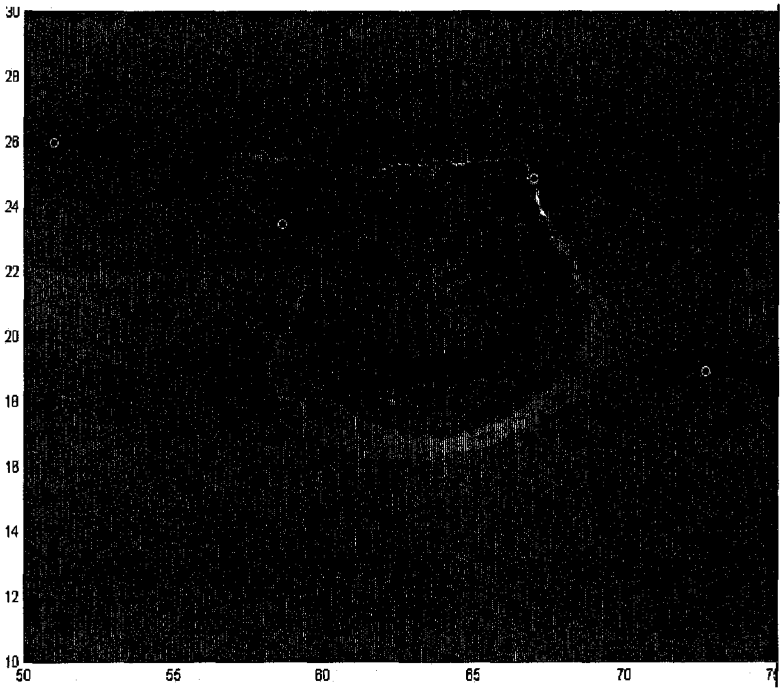
30
28
26
24
22
20
18
16
14
12
10
50
55
60
65
70
7

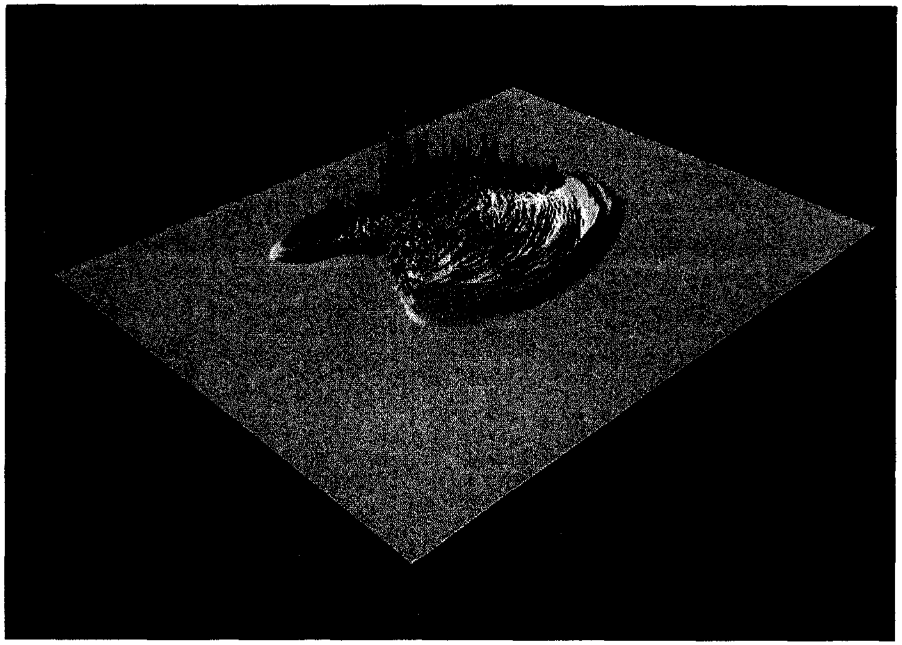

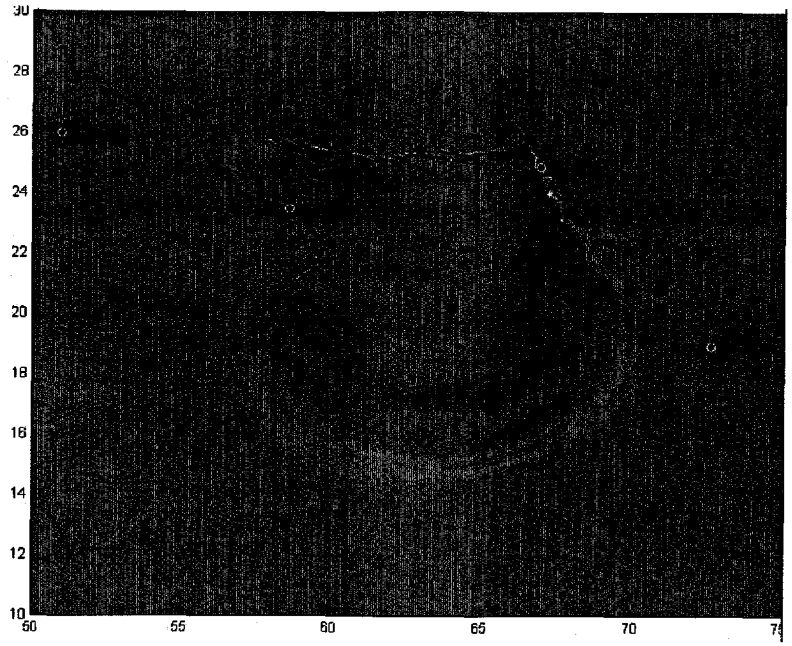
30
28
26
24
22
20
18
16
14
12
10
50
55
60
65
70
7

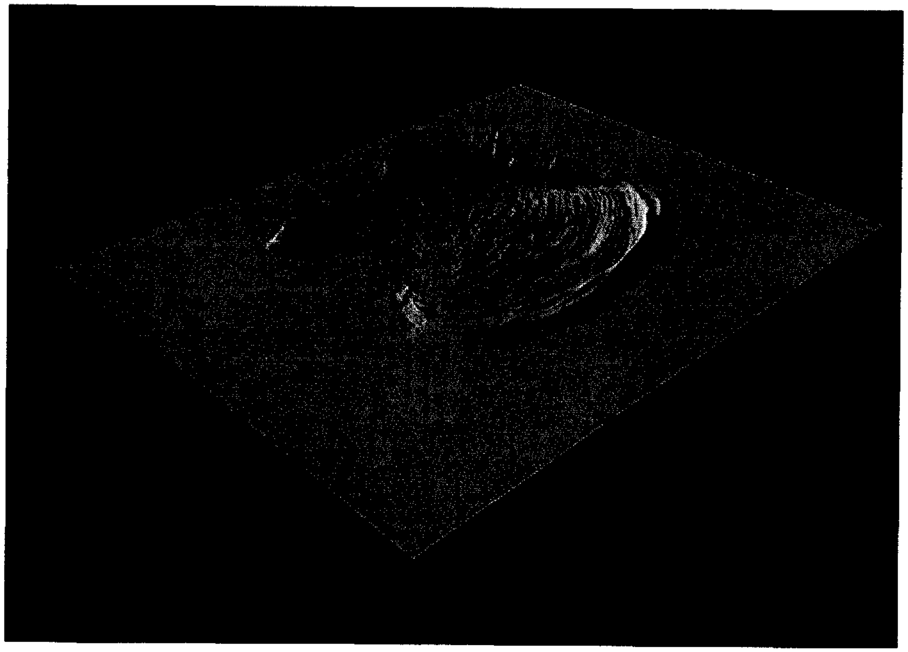

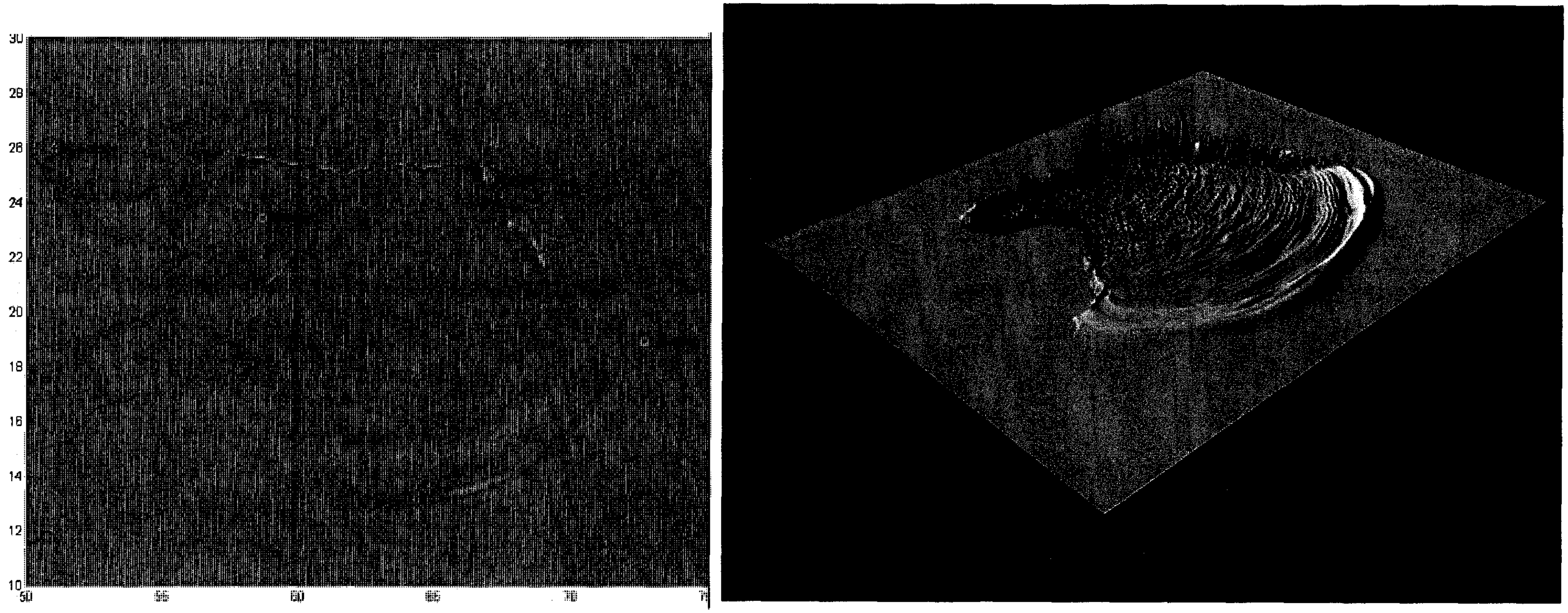
30
28
26
24
22
20
18
16
14
12
10
50
55
60
65
70

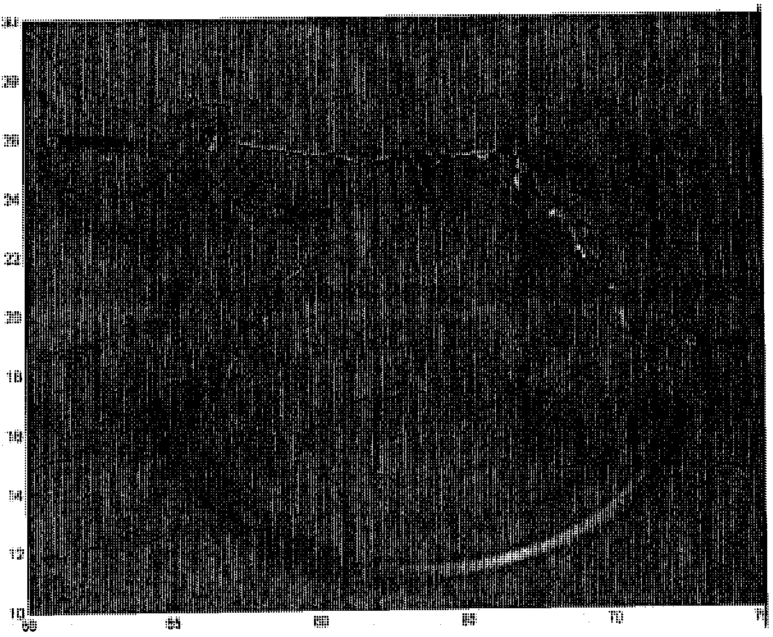
30
28
26
24
22
20
18
16
14
12
10
50
55
60
65
70
75

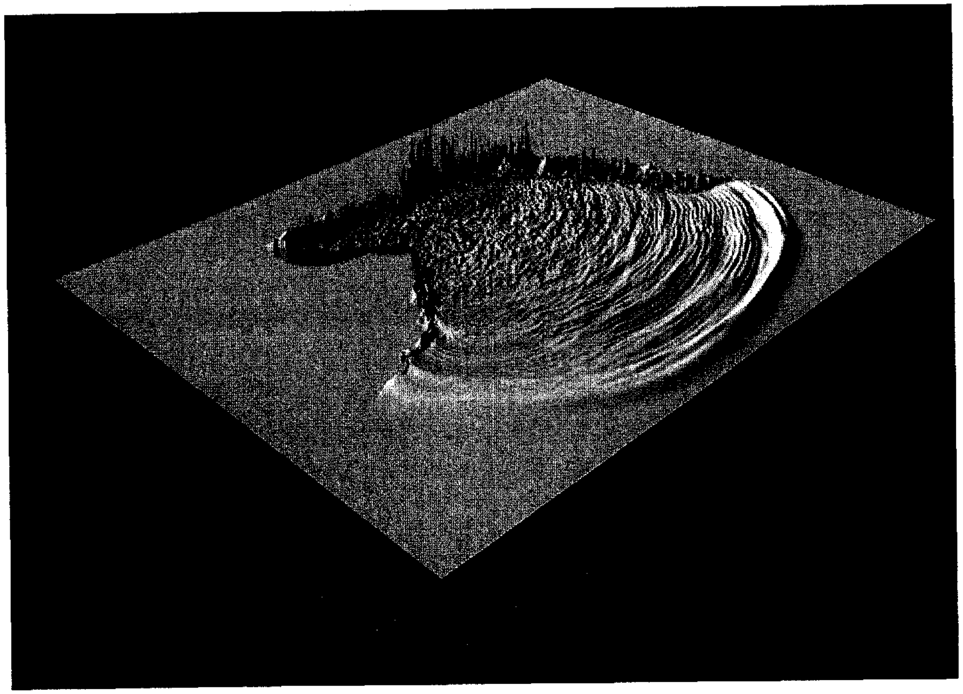

Figure A—8: The ocean surface elevation and maximum wave amplitude of Cascadia fault tsunami at different times (t=500s, 1000s, 1500s, 2000s and 2500s) after earthquake occurrence.

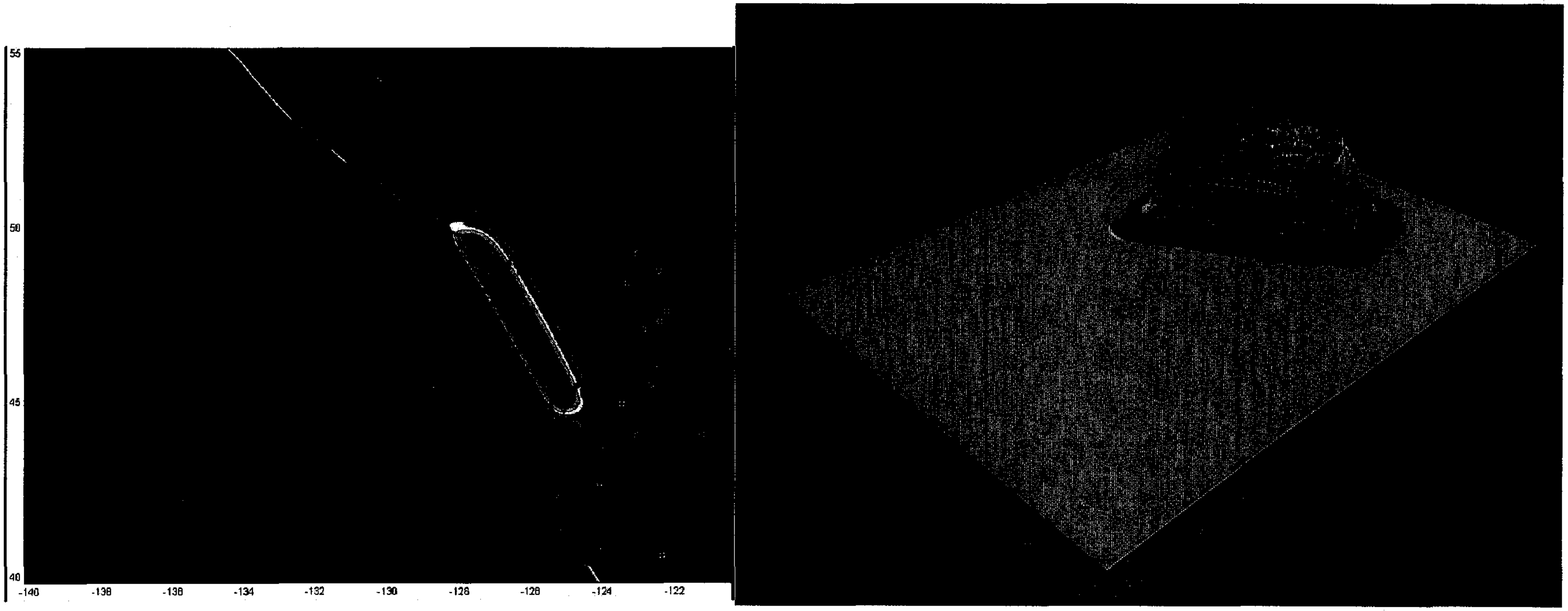

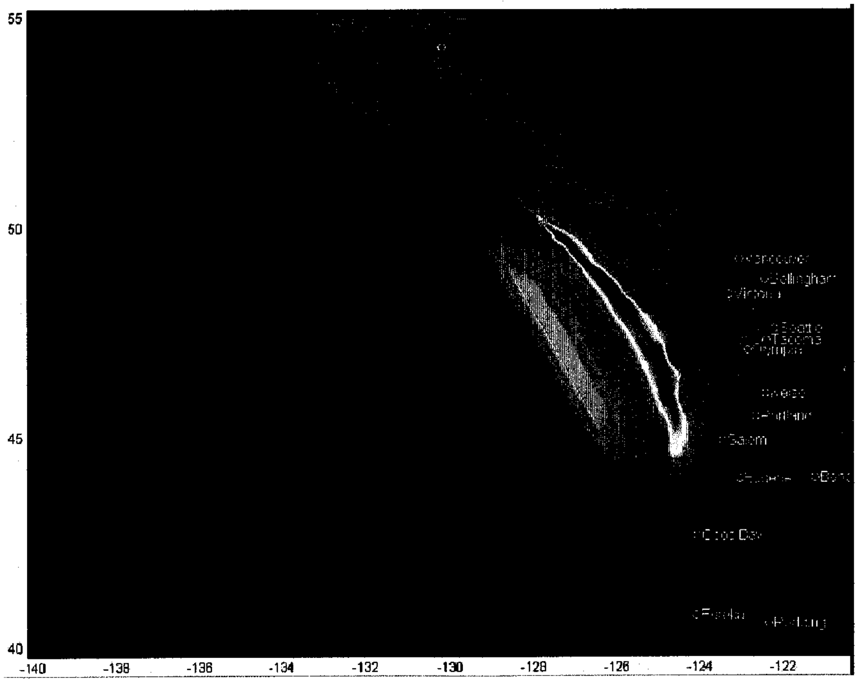
55
50
45
40
-140
-138
-136
-134
-132
-130
-128
-126
-124
-122
Vancouver
Bellingham
Victoria
Seattle
Tacoma
Olympia
Portland
Salem
Eugene
Coos Bay
Redding

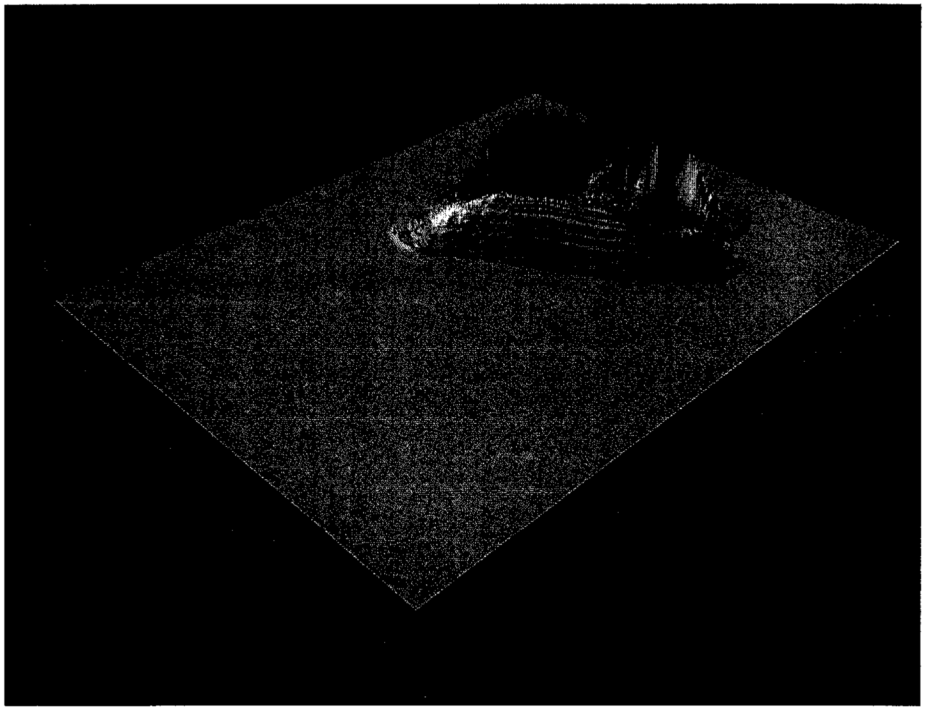

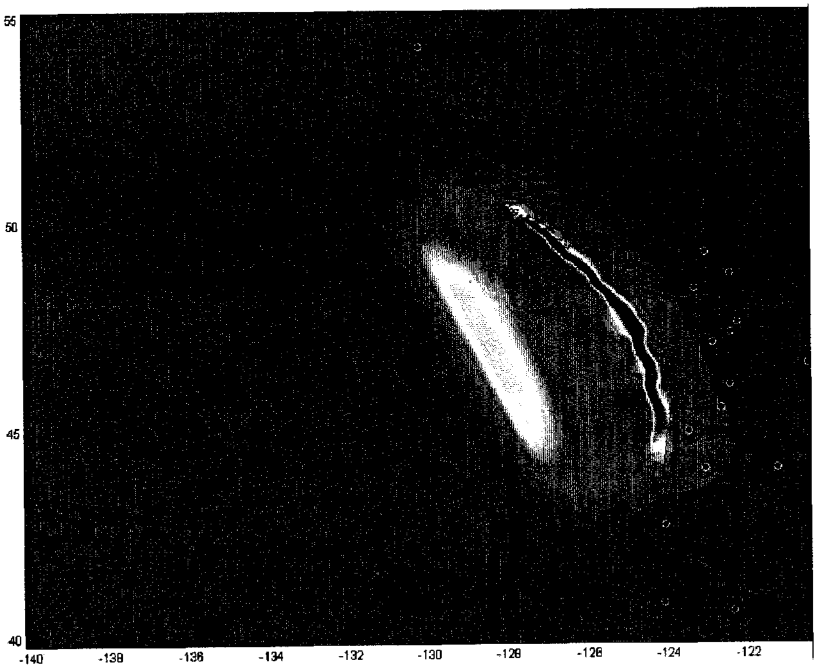
55
50
45
40
-140
-138
-136
-134
-132
-130
-128
-126
-124
-122

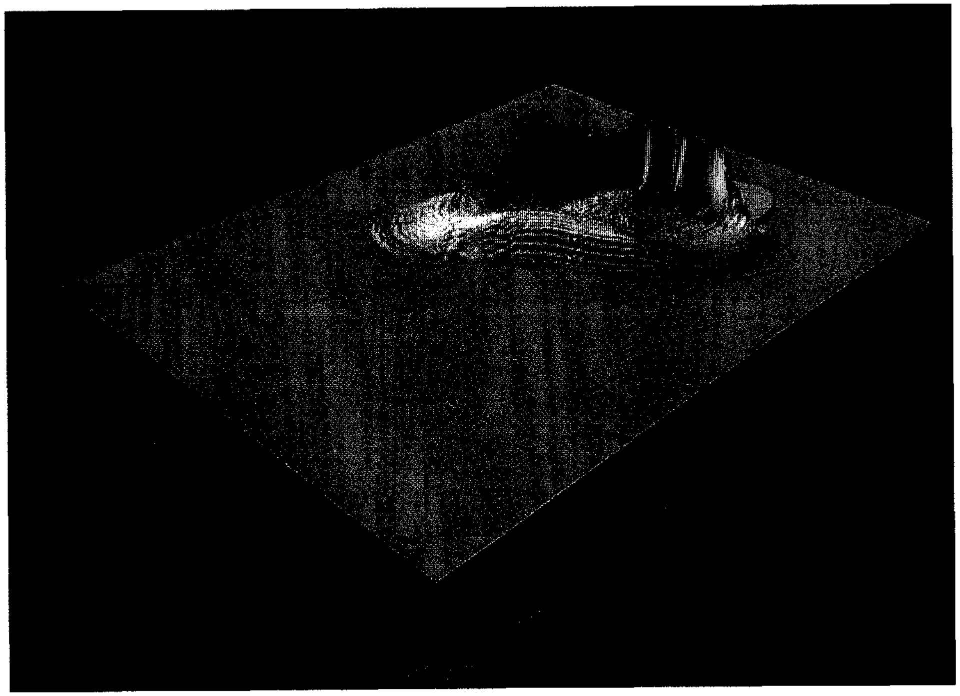

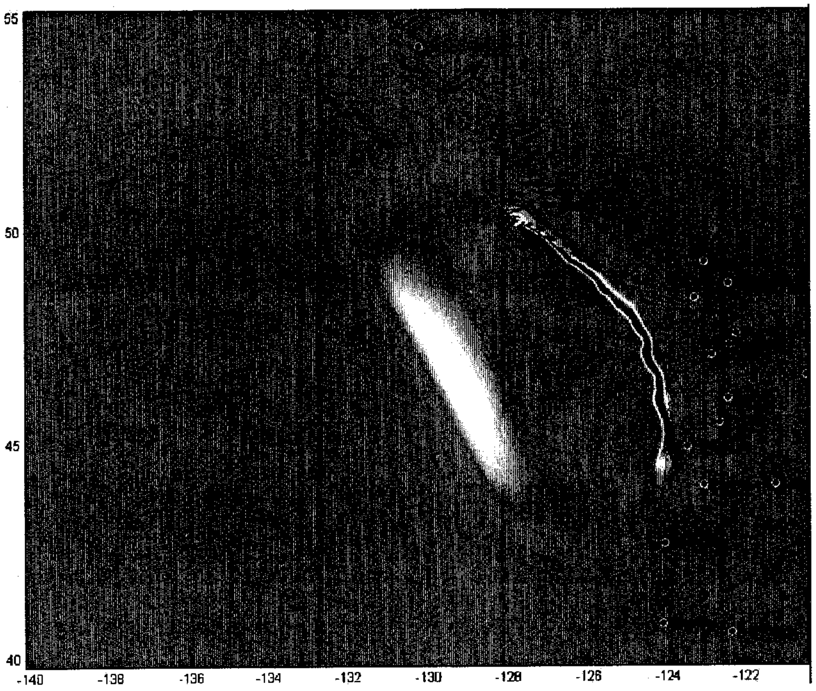
55
50
45
40
-140
-138
-136
-134
-132
-130
-128
-126
-124
-122

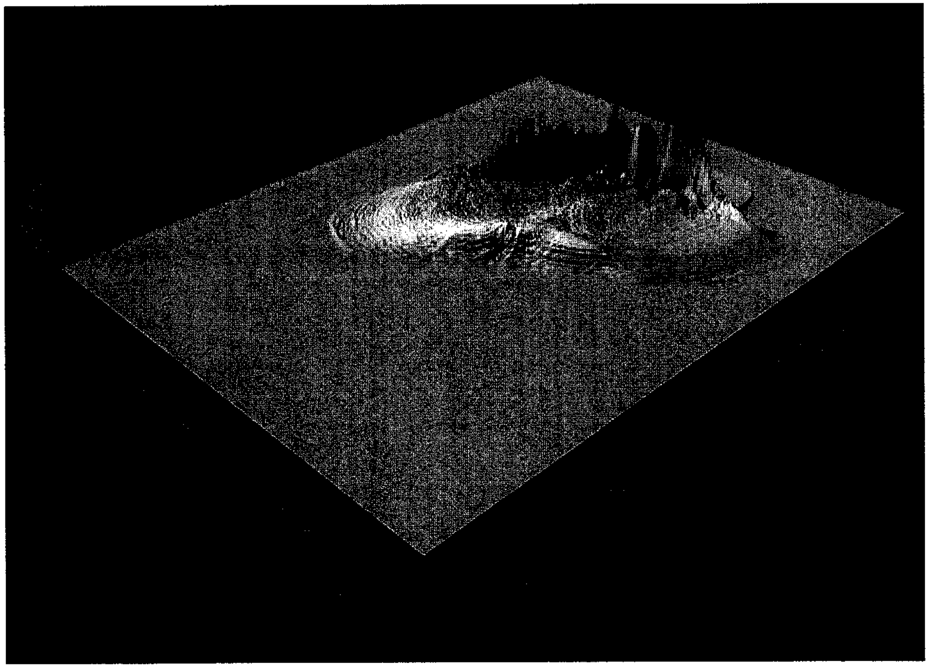

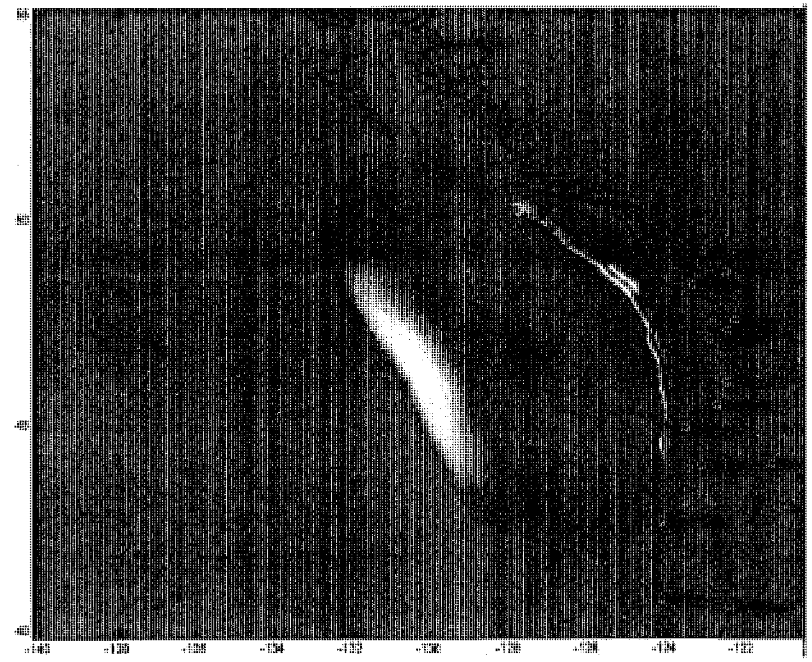
55
50
45
40
-140
-138
-136
-134
-132
-130
-128
-126
-124
-122